EES Catalysis

REVIEW ARTICLE

View Article Online
View Journal | View Issue



Cite this: *EES Catal.*, 2023, 1, 459

# Catalytic hydrogen storage in liquid hydrogen carriers

Yuwen Ni, Zhe Han,* Yuchao Chai, Guangjun Wu and Landong Li*

Received 5th April 2023,
Accepted 21st May 2023

DOI: 10.1039/d3ey00076a

rsc.li/eescatalysis

Hydrogen energy, often dubbed the "ultimate energy source", boasts zero carbon emissions and no harmful by-products. Nevertheless, the storage and transportation of hydrogen remain significant hurdles for its commercialization and large-scale implementation. Liquid hydrogen carriers (LHC), such as cyclohexane, methylcyclohexane, N-heterocycles, methanol, and ammonia, have emerged as promising solutions in hydrogen energy conversion systems. The storage and release of hydrogen rely on molecular hydrogenation and dehydrogenation processes, which are heavily influenced by the presence of catalysts. As such, a thorough understanding of catalyst design and mechanism is essential to facilitate (de)hydrogenation reactions under milder conditions. In this review, we explore three prevalent LHC systems and the catalysts employed during (de)hydrogenation processes. While noble metal catalysts exhibit superior performance in catalytic hydrogen storage, non-noble metal catalysts have also made considerable advancements. Furthermore, some liquid organic molecules are close to commercialization, potentially providing new options for energy storage and transportation. This article aims to trigger interest in LHC research and inspire the development of innovative catalytic systems for the catalytic hydrogen storage process.'

## Broader context

Hydrogen is currently considered as the most promising renewable energy source, however the physical properties of dihydrogen molecule present significant challenges for its large-scale storage and transportation. In order to overcome these challenges, various liquid compounds, namely aromatic hydrocarbons, N-heterocycles, methanol, and ammonia-related compounds, have been explored as potential hydrogen carriers. Ideally, these liquid hydrogen carriers can absorb and release dihydrogen through reversible hydrogenation and dehydrogenation reactions under practical conditions, making them suitable for large-scale storage and transportation applications. Catalysts are indispensable in the processes of hydrogen storage and release processes. In the past decades, significant progress has been made in developing catalysts for the dehydrogenation and hydrogenation of liquid hydrogen carriers, while some key issues are still to be addressed. Herein, a comprehensive overview of current state of catalytic studies related to liquid hydrogen carriers is provided. A thorough understanding of catalyst design and mechanism can facilitate the progress of liquid hydrogen carriers, ultimately contributing to the broader applications of hydrogen as a renewable energy source.

*Key Laboratory of Advanced Energy Materials Chemistry of Ministry of Education, College of Chemistry, Nankai University, Tianjin 300071, P. R. China.*
*E-mail: zhehan@nankai.edu.cn, lild@nankai.edu.cn*

**Yuwen Ni**

*Yuwen Ni received her Bachelor's degree from Nankai University in 2021. She then joined Prof. Landong Li's group as a MS student at the School of Materials Science and Engineering, Nankai University. Her current research focuses on the design and synthesis of catalysts for (de)hydrogenation.*

**Zhe Han**

*Zhe Han obtained his BSc in Chemistry in 2014 at Nankai University. Afterward, he pursued a PhD study with Prof. Can Li in $CO_2$ hydrogenation with heterogeneous catalysts. He is currently a postdoctoral researcher with Prof. Landong Li at Nankai University. His research interests focus on the conversion of C1 molecules by heterogeneous catalysis.*

## 1. Introduction

Fossil fuels have been acting as the indispensable driving force in human development. However, since the Industrial Revolution, the widespread use of fossil fuels has led to a steady increase in atmospheric carbon dioxide concentrations. By 2022, the global average atmospheric carbon dioxide concentration has reached a record 416 parts per million (ppm) and has continued to rise. The increasing carbon dioxide concentration significantly affects the global environment and biodiversity.[1] Sustainable and carbon-free energy systems need to be developed and deployed as soon as possible to achieve the goal of carbon neutrality.[2] Moreover, the energy shortages exposed by regional conflicts have emphasized the need to replace fossil fuels with renewable energy sources. Overall, it is pressing to find alternatives to fossil energy.

Hydrogen, one of the most promising renewable energy carriers, has the advantages of zero carbon emissions and no harmful by-products. Often referred to as the "ultimate energy source," hydrogen has the potential to address global environmental issues and solve the energy crisis of the 21st century. To harness the full potential of hydrogen, challenges in production, storage, transportation, and utilization must be addressed. Hydrogen storage and transportation, in particular, are crucial due to the highly flammable and explosive nature of hydrogen at ambient conditions. Hydrogen storage technology faces difficulties related to storage density (including mass and volume storage density), energy consumption, and safety.[3–5]

There are two primary categories of hydrogen storage methods: physical and chemical. Physical methods, such as high-pressure gas storage, low-temperature liquid storage, and adsorptive storage, each have benefits and drawbacks. For instance, high-pressure gaseous hydrogen storage is low-cost, fast, and operates at room temperature, but it has low safety levels, requires significant compression work, and demands pressure-resistant vessels.[5] Similarly, cryogenic liquid hydrogen storage has high energy density, but the high costs and energy consumption during liquefaction are significant drawbacks.[4] In order to encourage the development of materials for on-board hydrogen storage in light-duty automobiles, the US Department of Energy (DOE) sets system-level technical hydrogen storage targets of 5.5 wt% and 40 g $L^{-1}$ for 2025 and an ultimate target of 6.5 wt% and 50 g $L^{-1}$. In this field, emerging research trends include metal hydride hydrogen storage and porous material adsorptive hydrogen storage, both offering potential solutions to current limitations. Metal hydride hydrogen storage refers to hydrogen storage in the form of metal hydrides. The hydrogen release process is realized by the decomposition of metal hydride upon heating. The hydrogen storage reversibility of metal hydride still needs to be improved.[6] Porous material adsorptive hydrogen storage shows promise due to its safety, reliability, and efficiency. However, the volumetric storage capacity of porous materials is generally low.[7]

In contrast, hydrogen storage using specific molecules through reversible hydrogenation–dehydrogenation reactions can achieve high storage capacity. These molecules, typically liquid at room temperature, can be transported using existing infrastructure, ensuring safety and convenience.[4] Liquid hydrogen carriers (LHC) offer high hydrogen storage capacity, high energy density, and safe, convenient liquid storage and transportation. This technology is considered an alternative to liquefaction or high-pressure hydrogen storage and is expected to play a significant role in future hydrogen energy storage and transportation. For example, 1,3-diaminopropane has a theoretical hydrogen content of up to 10.8 wt%, far exceeding the US

**Yuchao Chai**

*Yuchao Chai received his BS degree in chemistry from Hunan University in 2014 and PhD degree in materials physics and chemistry from Nankai University in 2019. Now he is a professor in the College of Chemistry of Nankai University. His research interest focuses on the construction and application of single-site catalysts.*

**Guangjun Wu**

*Guangjun Wu received his PhD degree in materials physics and chemistry from Nankai University in 2009. Now he is an associate professor in the College of Chemistry, Nankai University. His research interest focuses on the synthesis and catalytic applications of zeolites.*

**Landong Li**

*Landong Li received his PhD degree in physical chemistry from Nankai University in 2006. Now he is a distinguished professor in the College of Chemistry, Nankai University. Prof. Li directs comprehensive research on energy-related heterogeneous catalysis.*

DOE (2020) target of about 5.5 wt%.[8] Research on utilizing these chemicals for hydrogen storage shows great potential for practical applications.[9,10]

The concept of LHC can be dated back to the 1980s.[11] Several systems have been proposed and studied to assess their viability for practical application.[12] Hydrogen carriers might be classified into two types: (1) hydrogen–lean organic liquids that achieve fully reversible hydrogenation and dehydrogenation storage cycles, such as aromatic hydrocarbons, and (2) hydrogen–lean inorganic small molecules such as $CO_2$ or $N_2$, which can form molecules containing elemental hydrogen after catalytic hydrogenation processes, like methanol and ammonia (Table 1). These systems show differences in their development timeline, hydrogen storage capacity, and energy density.[13]

Cycloalkanes such as cyclohexane and methylcyclohexane are widely used in industry and can be obtained at a relatively low cost. However, the cyclohexane/benzene and methylcyclohexane/toluene systems have their drawbacks. These reactants and products have low boiling points, making them gaseous during the dehydrogenation processes. As a result, condensation and purification steps are needed to separate pure hydrogen from mixed gases. Additionally, the toxicity of benzene must be considered. In comparison, the perhydrodibenzyltoluene system has a lower vapor pressure and volatility, allowing it to release hydrogen in the liquid phase. The stability of the DBT system is also relatively high, making it advantageous. However, the viscosity of this system is quite high, posing challenges for reactor design. N-Heterocyclic molecules have a lower dehydrogenation enthalpy than alkanes, allowing dehydrogenation to occur at lower temperatures. Nevertheless, side reactions like disproportion and alkyl transfer can negatively impact long-term cycling performance and should be avoided. Methanol, which has high hydrogen content and is widely used in industry, has its limitations as well. Methanol decomposition produces carbon monoxide (CO), which is harmful to hydrogen fuel cell applications. Thus, removing CO from the effluent is necessary. Ammonia, on the other hand, produces only nitrogen and hydrogen when decomposed, without any carbon-containing gases. However, ammonia production is energy-intensive, and its storage presents challenges due to its low boiling point and toxic nature. Ammonia borane and hydrous hydrazine can be stored and transported more easily, but they come at a high cost.

The hydrogen storage process using liquid hydrogen carriers includes hydrogenation and dehydrogenation. The hydrogenation process of organic molecules is generally thermodynamically favourable, enabling high selectivity and conversion. In contrast, the dehydrogenation process is a strongly endothermic reaction that is thermodynamically unfavourable. Besides, dehydrogenation catalysts are prone to deactivation due to sintering and coking at high temperatures.

Thus, the main challenge in achieving hydrogen storage using liquid organic hydrogen carriers is to develop dehydrogenation catalysts that are low-cost, highly stable, and offer high activities. This review highlights the development of three types of substrates in hydrogen storage applications and introduces catalysts used in the reaction process, aiming to inspire further research in this hot field.

## 2. Cycloalkanes

When the concept of liquid hydrogen carriers (LHC) was initially proposed, the primary focus of research was on the hydrogen storage cycles of benzene-based hydrocarbons, such as benzene/cyclohexane and toluene/methylcyclohexane (MCH). In addition to these two classical systems, researchers have developed the hydrogen storage cycles of benzyltoluene (H0-BT)/perhydrobenzyltoluene (H12-BT), dibenzyltoluene (H0-DBT)/perhydro-dibenzyltoluene (H18-DBT), and naphthalene/hydrides of naphthalene, including tetralin and decalin over the past twenty years.[3] In 2003, Air Products and Chemicals pioneered the use of carbazole-based molecules for hydrogen storage. A new class of heteroaromatic compounds, *N*-ethylcarbazole (NEC)/dodecahydro-*N*-ethylcarbazole (DNEC), was proposed, which can be used for reversible hydrogen storage under moderate conditions without generating unwanted impurities. The dehydrogenation enthalpy of this system is 51 kJ per mol $H_2$, allowing the dehydrogenation process to occur at a much lower temperature compared to naphthenic hydrocarbons.[14] Similar systems include *N*-propylcarbazole (NPCZ)/

Table 1 Properties of presentative compounds for LHC

| Hydrogen carrier | Dehydrogenated carrier | $H_2$ density | | Dehydrogenation enthalpy (kJ per mol $H_2$) |
|---|---|---|---|---|
| | | wt% | g $L^{-1}$ | |
| Cyclohexane ($C_6H_{12}$) | Benzene ($C_6H_6$) | 7.1 | 56.3 | 68.6 |
| Methylcyclohexane ($C_7H_{14}$) | Toluene ($C_7H_8$) | 6.1 | 47.1 | 68.3 |
| Decalin ($C_{10}H_{18}$) | Naphthalene ($C_{10}H_8$) | 7.3 | 64.9 | 63.9 |
| Cyclohexylbenzene ($C_{12}H_{16}$) | Biphenyl ($C_{12}H_{10}$) | 3.8 | 35.6 | 65.9 |
| Tercyclohexane ($C_{18}H_{32}$) | Terphenyl ($C_{18}H_{14}$) | 7.2 | 67.5 | — |
| Perhydro-dibenzyltoluene ($C_{21}H_{38}$) | Dibenzyltoluene ($C_{21}H_{20}$) | 6.2 | 56.4 | 62, 65, 71 |
| Dodecahydro-*N*-ethylcarbazole ($C_{14}H_{25}N$) | *N*-Ethylcarbazole ($C_{14}H_{13}N$) | 5.8 | — | 50.6 |
| Octahydro-1*H*-indole ($C_8H_{15}N$) | Indole ($C_8H_7N$) | 6.4 | 58.5 | 51.9 |
| Methanol ($CH_3OH$) | Carbon dioxide ($CO_2$) | 12.6 | 99.8 | 16.5 |
| Ammonia ($NH_3$) | Nitrogen ($N_2$) | 17.7 | 108 | 30.6 |
| Ammonia borane ($NH_3BH_3$) | Hydrolysis: $NH_4BO_2$ | 19.6 | 145 | −52 |
| Hydrous hydrazine ($N_2H_4{\cdot}H_2O$) | Nitrogen ($N_2$) | 8.0 | 82.6 | −25.3 |

perhydro-*N*-propylcarbazole (12H-NPCZ),[15] indole/indoline, 2-methylindole (2-MID)/8H-2-methylindole (8H-2-MID),[16] *N*-ethylindole (NEID)/octahydro-*N*-ethylindole (8H-NEID),[17] and tetrahydroquinoline/quinoline.[18]

The hydrogenation process of aromatic hydrocarbons (the term aromatic hydrocarbons in this context refers to a broader definition and includes non-benzene aromatics) results in a reduction of Gibbs free energy, often with a large absolute value, which is thermodynamically advantageous. Consequently, the conversion and selectivity of the hydrogenation process of aromatic hydrocarbons are very high, with conversion even approaching 100%. The aromatic hydrogenation process is well-established and has been industrialized. However, the dehydrogenation reaction is strongly endothermic that requires low-pressure and high-temperature conditions while also being limited by reaction equilibrium constraints.[8] Early studies on chemical hydrides as hydrogen storage media indicated that chemical hydrides could not be recycled for these reasons. Moreover, dehydrogenation catalysts are susceptible to pore structure destruction, coking, and deactivation under high-temperature conditions. The dehydrogenation process might also involve side reactions, such as hydrogenolysis. Consequently, research on these systems primarily concentrates on the dehydrogenation process.

The activation and breaking of multiple C–H bonds are required during dehydrogenation, both for the traditional benzene-cycloalkane and the newly developed carbazole-based system. Therefore, the selectivity of catalysts is crucial, and the challenge lies in reducing the cost of dehydrogenation catalysts while ensuring high conversion, high selectivity, high stability, and good resistance to coking deactivation. Many studies indicate that noble metals, such as Pt and Pd, show excellent performance as the active component of catalysts. The activity of the catalyst largely depends on the presence of a suitable structure for the active sites, allowing the adsorption and activation of reactant molecules. Pt-Based and Pd-based catalysts continue to be the focus of current research. Although noble metal catalysts have shown exceptional catalytic activity, the scarcity of Pt, Pd, and other noble metals in nature, combined with high industrial costs, limit the practical application of these catalysts. From an industrial application standpoint, non-noble metal-based aromatic hydrocarbon dehydrogenation catalysts, such as those utilizing Ni, Cu, and other active metals, are more practical. Among these, Ni-based catalysts show great promise.

To further enhance the dehydrogenation activity of catalysts, it is common practice to add a second metal component to the catalyst. Bimetallic catalysts perform well in dehydrogenation reactions because the second active metal component can inhibit the migration and agglomeration of the original active metal on the catalyst surface, thus improving the stability and specific activity of the catalyst.[19] In addition, the performance of the catalyst can be improved by modifying factors such as the catalyst support, the morphology of the catalyst, and the interaction between the active components and the support.

### 2.1 Benzene/cyclohexane

Benzene/cyclohexane is one of the most well-known and classical LHC systems and has been studied extensively. Dehydrogenation is the most challenging part of this cycle because the C–H bonds in cyclohexane are thermodynamically stable and kinetically inert. In most cases, catalysts are required to accelerate the dehydrogenation of cyclohexane to hydrogen and benzene.[20] Transition metals are commonly used as catalysts for the activation of C–H bonds because they can hybridize their s- or d-orbitals with C–H s* anti-bonding orbitals so they can weaken the C–H bonds of hydrocarbons.[21] Transition metal-based catalysts for this process mainly include Pt, Pd, and Co as the active component.

**2.1.1 Pt-Based catalysts.** In 1969, Boudart proposed that cyclohexane dehydrogenation on Pt is a structure-insensitive reaction.[22] However, later in the 1990s, a study using the model catalyst prepared by depositing inactive metal atoms on the surface of a Pt(111) single crystal suggested that at least 8 Pt atoms were required for cyclohexane dehydrogenation to benzene.[23] The high cost and low natural abundance of Pt limit its application in the industry. Reducing Pt particle size is an effective way to reduce industrial costs and maximize atomic efficiency. Chen *et al.* prepared a single-site $Pt_1/CeO_2$ catalyst using the modified ascorbic acid-assisted reduction method. This catalyst has active sites consisting of single Pt atoms and neighbouring oxygen vacancies and exhibits unique catalytic properties for the reversible dehydrogenation and hydrogenation of large molecules such as cyclohexane and methylcyclohexane (Fig. 1).[24] Recently, the concept of a fully exposed cluster catalyst was proposed by Ma *et al.*[25] A series of platinum catalysts that have Pt clusters of different sizes anchored on the curved graphene layer of nanodiamond (ND@G) were prepared by using the incipient wetness impregnation or precipitation method.[26] The catalytic performance and DFT calculations prove the advantage of fully exposed few-atom Pt ensembles in cyclohexane dehydrogenation. Researches on Pt-based catalysts also focus on using different supports and promoters. Some representative results are summarized in Table 2. Goodman *et al.* compared the performance of $\gamma$-$Al_2O_3$, $SiO_2$, and activated carbon supported Pt catalysts.[27] The activity decreases in the trend of Pt/$\gamma$-$Al_2O_3$ > Pt/$SiO_2$ > Pt/C. Zhu *et al.* tested Pt supported on a series of carbon materials, including hollow and mesoporous carbon nanoparticles, multiwall carbon nanotubes, and activated carbon.[28] Among these catalysts, the Pt/hollow carbon nanoparticle shows the best activity, achieving cyclohexane conversion of ~80% at 310 °C. The good activity is ascribed to the short pore channels of carbon nanoparticles which favor the diffusion of benzene and reduces the coke formation. Luo *et al.* used Sn-doped $MgAlO_x$ as support for Pt catalyst in cyclohexane dehydrogenation.[29] The Sn-doped $MgAlO_x$ was prepared from the decomposition of hydrotalcite-like precursors by microwave heating. Pt was introduced by impregnation. The interaction between Sn and $MgAlO_x$ was enhanced by microwave calcination, making the Sn species more difficult to be reduced. The interfacial character between Pt and $MgAlO_x$ was modified by the addition of Sn, which accelerates the

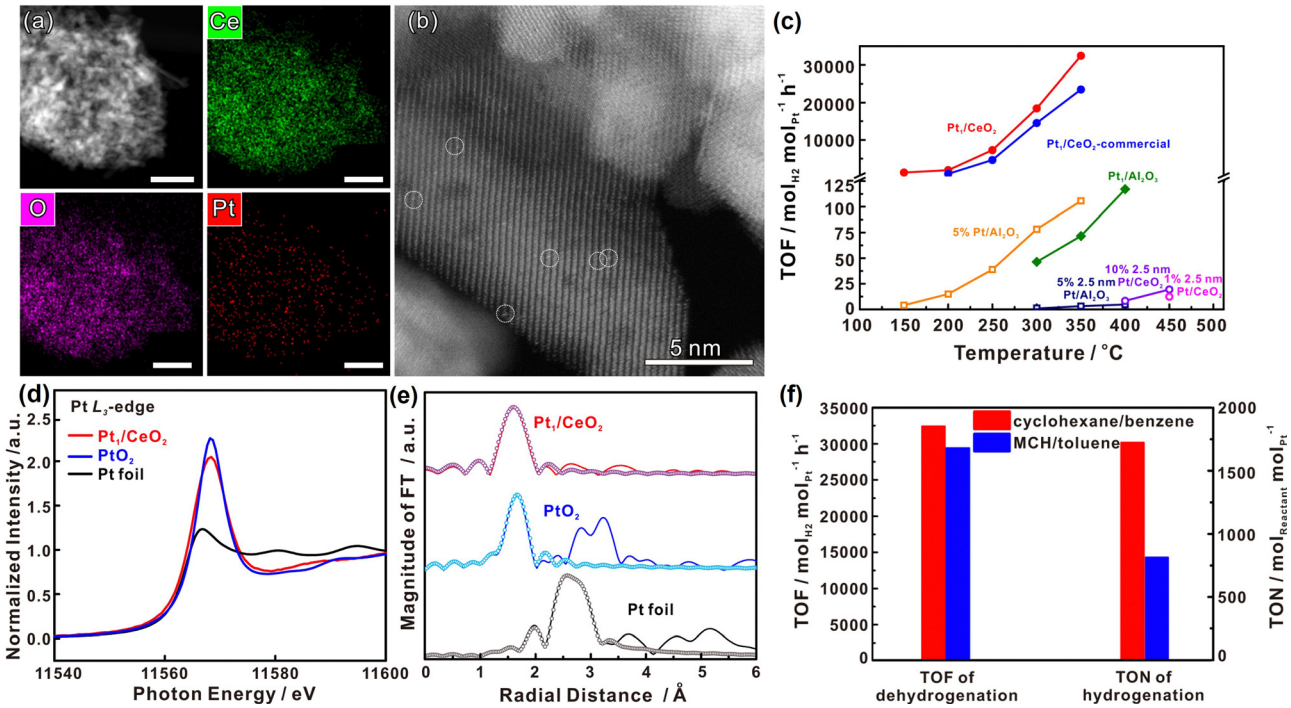


Fig. 1 (a) HAADF-STEM images with corresponding elemental distribution images and (b) Cs-corrected HAADF-STEM images of $Pt_1/CeO_2$. (c) Comparison of the performance of $Pt_1/CeO_2$ with other catalysts in cyclohexane dehydrogenation. (d) Normalized Pt $L_3$-edge XANES spectra and (e) $k^3$-weighted Fourier transform EXAFS spectra ($L_3$-edge) of Pt in $Pt_1/CeO_2$, $PtO_2$, and bulk Pt foil. (f) Comparisons of the performance in dehydrogenation and hydrogenation of different molecules.[24] Modified with permission from ref. 24. Copyright (2022) Springer Nature.

Table 2 Pt-based catalysts for cyclohexane dehydrogenation

| Catalyst | Temp. (°C) | Space velocity | Conv. (%) | Sel. (%) | Ref. |
|---|---|---|---|---|---|
| 3 wt% Pt/C | 280 | 1 $h^{-1}$ (WHSV) | ~58 | | 35 |
| Pt/CN (N-doped carbon) | 210 | | 96.03 | 100 | 36 |
| $Pt_1/CeO_2$ | 350 | 24 $h^{-1}$ (WHSV) | ~30 | ~100 | 24 |
| $Pt/MgAl(Sn)O_x$ | 550 | 360 $h^{-1}$ (GHSV) | ~11 | ~48 | 29 |
| $Pt/Al_2O_3$ | 200 | | 72.1 | | 30 |
| $Pt–Ca/Al_2O_3$ | 350 | 10 $h^{-1}$ (WHSV) | 97.0 | | 31 |
| $Pt_3Sn/SiO_2$ | 600 | | ~35 | ~85 | 33 |

migration of reaction intermediates. Besides, the electronic state of Pt was modified by the formation of PtSn alloy, which suppresses olefin adsorption on the surface and reduces the deep dehydrogenation and hydrogenolysis activity. All these effects contribute to the good activity of $Pt/MgAl(Sn)O_x$. Kusakabe *et al.* studied cyclohexane dehydrogenation in a membrane reactor catalyzed by $Pt/Al_2O_3$.[30] The FAU-zeolite membrane was fabricated on a porous $\alpha$-$Al_2O_3$ support tube by hydrothermal synthesis and used to separate benzene and hydrogen from the reactant. The FAU membrane shows a high separation factor for benzene over cyclohexane of 70 at 100 °C, which decreases at higher temperatures. The decrease is caused by the reduced benzene adsorption at high temperatures, which reduces the blocking effect of benzene for cyclohexane diffusion. Separating products during the reaction can increase the conversion beyond thermodynamic equilibrium. The cyclohexane conversion achieves 72.1% at 200 °C with a sweep gas flow of 100 mL $min^{-1}$, which is much higher than the equilibrium conversion of 32.2%. Xu *et al.* reported that the performance of $Pt/Al_2O_3$ could be improved by the addition of Ca.[31,32] The introduction of CaO inhibits the coke formation by neutralizing the residual Cl ions on the $Al_2O_3$ surface which is a key site for coke formation. The deep dehydrogenation of H-rich carbonaceous species is suppressed by CaO addition. At the same time, the coke desorption is enhanced by the increased hydrogen content of the hydrogen-deficient coke.

The dispersion of Pt and hydrogen spillover capability of the catalyst is also improved by CaO addition with a decreased product adsorption on Pt sites by electron transfer from Ca to Pt. The catalyst with Ca/Pt of 5 shows the best activity and stability. At low Ca loading, the hydrogen spillover from the Pt–Al interface is not enhanced efficiently. While at high Ca loading, The CaO covers the support surface. The strong interaction between CaO and Pt suppresses the reduction of Pt and reduces the initial activity. Komatsu *et al.* tested $SiO_2$ supported Pt-based intermetallic compounds, including Co, Ge, Sn, Tl, and Zn, in this reaction.[33] $Pt_3Zn/SiO_2$, $Pt_3Tl_2/SiO_2$, $Pt_3Co/SiO_2$ were prepared by impregnation while $Pt_3Sn/SiO_2$, $PtSn/SiO_2$, and $PtGe/SiO_2$ were prepared by chemical vapor deposition. $Pt_3Sn/SiO_2$ and $PtGe/SiO_2$ show higher activity and benzene selectivity than $Pt/SiO_2$, while other catalysts show lower activity and poor benzene selectivity. The difference is ascribed to the different chemical properties of the second metal as well as geometric factors. Ali *et al.* studied the performance of Pt, Rh, Re, U, PtIr, PtRh, PtRe, and PtU on

$\gamma$-$Al_2O_3$ using a pulsed micro-reactor.[34] For the monometallic catalyst, the activity follows the order of $Pt/Al_2O_3 > Rh/Al_2O_3 > Ir/Al_2O_3 > Re/Al_2O_3 \geq U/Al_2O_3$. For the bimetallic catalyst, the $PtRh/Al_2O_3$ shows the best activity, which is higher than the $Pt/Al_2O_3$. The addition of U in $Pt/Al_2O_3$ leads to a decreased activity, possibly because of the low electronegativity of U than Pt.

In addition to the thermal strategy, the dehydrogenation of cyclohexane using other energy sources, such as renewable solar energy, has been studied. This process can be performed under mild conditions. Recently, Zhang *et al.* synthesized Pt/black $TiO_2$ photocatalysts *via* reduction–oxidation–reconstruction protocol.[37] In this method, $TiO_2$ nanoparticles were first reduced by $NaBH_4$, then subjected to surface oxidation treatment with aqueous $H_2O_2$. Pt was finally introduced *via* a conventional wet impregnation. The catalyst obtained is designated as Pt@BT-O. The 0.2 wt% Pt@BT-O can achieve cyclohexane conversion of 99% under 1 h of visible-light irradiation at 43 °C with a ratio of produced benzene to $H_2$ close to 1 : 3.

**2.1.2 Other transition metal-based catalysts.** Despite the good performance, the very high cost of Pt affects its practical application. Consequently, other transition metal-based catalysts have been explored (Table 3). Pd-Based photocatalyst has become one of the choices. Jeong *et al.* reported UV-assisted dissociation of C–H bonds at low temperatures using the $TiO_2$ surfaces modified by Pd nanoparticles (Pd–$TiO_2$).[38] Photocatalytic dehydrogenation requires low pressure and temperature, making it a promising $H_2$-release process for LHC compared to conventional thermocatalytic strategies. Rodríguez-Ramos *et al.* used Ir supported on carbon and $Al_2O_3$ in cyclohexane dehydrogenation.[39] The morphologies of Ir on these two supports are different. Ir nanoparticles are spheres and rafts in Ir/C and $Ir/Al_2O_3$, respectively. A comparison of $H_2$ and CO chemisorption suggests that more than one hydrogen atom can be adsorbed on the surface of each Ir atom. The support influences the amount of H adsorbed on Ir. Reaction results show that cyclohexane dehydrogenation is not sensitive to the metal dispersion and support type. The Ir catalysts also exhibit good resistance to the thiophene molecule in the feed.

Some non-noble metal catalysts, such as Ni[40] and Zn,[41] also show good catalytic activity. Besides, bimetallic catalysts play an important role in enhancing activity in various reactions compared to monometallic catalysts, including the dehydrogenation of cyclohexane. Improving the performance of non-noble metal-based catalysts has practical significance for promoting the application of catalysts. Liu *et al.* studied the influence of Ni particle size on cyclohexane dehydrogenation using $Ni/SiO_2$/Mo(110) model catalysts.[42] Ni was deposited on the substrate by vapor deposition and the size was controlled by changing the deposition time. The results show that the TOF increases with the decrease of Ni particle size for the particles smaller than 2.5 nm due to the increase portions of low coordinated Ni atoms favoring $H_2$ desorption, while the TOF is not sensitive to the particle size for the particles larger than 2.5 nm. Viveros *et al.* used $Al_2O_3$–$TiO_2$ as support for Ni in this reaction.[43] The effect of $TiO_2$ on the performance of $Ni/Al_2O_3$ is influenced by the $TiO_2$ content, Ni loading, and reduction temperature. At low $TiO_2$ content, the dispersion and intrinsic activity of Ni can be promoted by $TiO_2$. However, at high $TiO_2$ content, the metallic Ni surface is partially covered by reduced $TiO_x$ species due to the strong metal support interaction, resulting in reduced activity. Ichikawa *et al.* used Pt to promote the performance of Ni supported on activated carbon cloth (ACC).[44] The activity was tested using a spray-pulsed mode reactor. The addition of only 0.5 wt% Pt into 20 wt% Ni/ACC increases the hydrogenation production rate by ~1.5 times. The promotion effect of Pt is ascribed to the easy formation and desorption of $H_2$ on the Pt surface and a synergistic effect of Ni–Pt for C–H bond activation. Chen. *et al.* studied the performance of Ni–Cu/$SiO_2$ in cyclohexane dehydrogenation.[45] The catalysts were prepared by the one-step sol–gel method. $Ni/SiO_2$ shows low dehydrogenation selectivity of <50% at 350 °C due to the small Ni particle size, which has high hydrogenolysis activity. The addition of Cu increases the selectivity to benzene, possibly due to the formation of NiCu alloy. The $Ni_{0.85}Cu_{0.15}/SiO_2$ exhibits 94.9% conversion of cyclohexane with selectivity to benzene of 99.5% at 350 °C. SBA-15 was also used as support for Ni–Cu catalyst.[46] The NiCu/SBA-15 with Ni and Cu of 4.9 wt% and 3.5 wt% shows a cyclohexane conversion of 99.4% and benzene selectivity of 98.7% at 350 °C. *In situ* diffuse reflectance infrared Fourier transform spectroscopy (DRIFT) shows that vinyl species are present on the catalyst surface during dehydrogenation. Liu *et al.* studied the performance of $Ni_2P/\gamma$-$Al_2O_3$ in this reaction.[47] The catalyst was prepared by the decomposition of nickel hypophosphite supported on $Al_2O_3$ under $N_2$ atmosphere. The $Ni_2P/\gamma$-$Al_2O_3$ shows higher activity, selectivity, and stability compared to $Ni/Al_2O_3$ and achieves cyclohexane conversion of 80% with benzene selectivity of

Table 3 Other transition metal-based catalysts for cyclohexane dehydrogenation

| Catalyst | Temp. (°C) | Space velocity | Conv. (%) | Sel. (%) | Ref. |
|---|---|---|---|---|---|
| 10 wt% $Ag^{-1}$ wt% Pt/ACC | 300 | | | 100 | 52 |
| Ni–Cu/SBA-15 | 350 | 12 000 mL $g^{-1}$ $h^{-1}$ (GHSV) | 99.4 | 98.7 | 46 |
| $Ni_2P/Al_2O_3$ | 340 | 1 $h^{-1}$ (WHSV) | 80 | 99.9 | 47 |
| $Pd/CeO_2$-HT | 450 | 12 000 mL $g^{-1}$ $h^{-1}$ (GHSV) | 65.3 | 100 | 53 |
| $Ni/Al_2O_3$ | 340 | 1 $h^{-1}$ (WHSV) | 65 | 90 | 47 |
| 1 : 4 Ag-Rh/$Y_2O_3$ | 300 | | 35.8 | | 54 |
| $Co/SiO_2$ | 550 | 2.3 $h^{-1}$ (WHSV) | 9.1 | 74.4 | 48 |
| Ni/20%$CeO_2$–$Al_2O_3$ | 350 | 3 $h^{-1}$ (WHSV) | ~50 | 100 | 55 |
| RANEY®-Ni | 320 | | 72.7 | 100 | 56 |

79.9% at 340 °C. The good performance of $Ni_2P$ is ascribed to the positive charge of Ni which enhances the interaction between reactant and active sites and reduces the adsorption of benzene as well as the ensemble effect of P in $N_2P$ that inhibits the sintering of $Ni_2P$ under reaction conditions. $H_2$ temperature-programmed desorption (TPD) profiles show that the $Ni_2P$ has a stronger $H_2$ spillover effect, which may contribute to the good performance. *In situ* DRIFT shows that the P-covered Ni sites of $Ni_2P(0001)$ should be the active sites.

Sooknoi *et al.* tested $Co/SiO_2$ in cyclohexane dehydrogenation.[48] A series of $Co/SiO_2$ was prepared by electrostatic adsorption of Co salts on $SiO_2$ using $[Co(bipy)_3](NO_3)_2$, $[Co(NH_3)_5Cl]Cl_2$, $[Co(NH_3)_6]Cl_3$, and $[Co(en)_2Cl_2]Cl$. The activity of the catalyst prepared using $[Co(bipy)_3](NO_3)_2$ is the highest among these catalysts, which is ascribed to the highest $Co^{2+}$ content in the catalyst. A comparison of the activity for reduced and unreduced catalysts shows that metallic Co is much less active than the $Co^{2+}$ species. It is proposed that the dehydrogenation on cationic $Co^{2+}$ species has two steps. The first one is the C–H dissociation with the formation of cobalt–alkyl species and Si–OH, followed by β-H elimination of the cobalt–alkyl species. Since the activity of this catalyst under $H_2$ is higher than $N_2$ atmosphere, it is concluded that a cobalt hydride intermediate formed under $H_2$ can facilitate the C–H activation of reactant without the necessity for dissociation of the Co–O bond. Pinard *et al.* used Ga containing MFI zeolite in cyclohexane dehydrogenation.[49] Three catalysts were prepared by direct hydrothermal synthesis, ion exchange, and physical mixture. Ga incorporates into the zeolite framework by direct hydrothermal synthesis while deposits on the outer surface by ion exchange. For the physical mixture, $Ga_2O_3$ and zeolite are physically separated. The Ga species located on the outer surface of zeolite can be reduced and migrate into the zeolite crystal after high-temperature reducing treatment. The dehydrogenation reaction was conducted at 530 °C. Reaction results show that the catalysts prepared by hydrothermal synthesis show higher selectivity to benzene than the other two catalysts due to its weak acid strength. Du *et al.* reported that the C-$Mo_2C$ composite catalyst could catalyze cyclohexane dehydrogenation.[50] Catalysts with different Mo contents were prepared by hydrothermal synthesis followed by carbonized at high temperatures. The catalyst with 25 wt% Mo content shows the best activity with conversion of ~11% and selectivity to benzene of ~100% at 315 °C. Chen *et al.* studied the performance of Cu/SBA-15 in this reaction.[51] A series of Cu/SBA-15 with different Cu loading of 1.9–7.1 wt% was prepared by impregnation. For all the catalysts tested, the selectivity to benzene is 100%. The 3.7 wt% Cu/SBA-15 shows the highest turnover frequency (TOF) of 5578 mol $h^{-1}$ $mol_{Cu}{}^{-1}$ at 350 °C due to the small Cu particle size under reaction conditions. This catalyst also shows good stability with only slight activity loss after 20 h on stream. Although the 1.9 wt% Cu/SBA-15 with lower Cu content should have a smaller Cu particle size at the initial state, the sintering of Cu nanoparticles after reduction makes the TOF of this catalyst lower than the 3.7 wt% Cu/SBA-15.

### 2.2 Toluene/methylcyclohexane

The toluene/methylcyclohexane system is another attractive system of LHC. This system can achieve gravimetric and volumetric hydrogen storage densities of up to 6.1 wt% and 47.1 g $L^{-1}$, respectively.[13] The enthalpy change for this reaction is 205 kJ $mol^{-1}$ as shown in the equation below.[57]

$$C_7H_{14} \rightarrow C_7H_8 + 3H_2 \quad \Delta H^{\theta} = 205 \text{ kJ mol}^{-1}$$

The methylcyclohexane–toluene–hydrogen (MTH) system, first proposed by Taube *et al.*, shows great potential for application.[11] Compared to benzene in the cyclohexane–benzene–hydrogen (CBH) cycle, toluene in the MTH cycle is less toxic, aligning with the current green energy development goals. While the hydrogenation of toluene has already been commercialized, the main challenge lies in resolving the issue of catalytic dehydrogenation.[58] From an energy standpoint, the MCH system can form a relatively closed loop if the heat generated from the hydrogenation reaction is utilized for the dehydrogenation reaction and gasification of reactants.

Catalytic dehydrogenation of MCH is typically carried out using heterogeneous catalysts with metal and acid functionalities. A crucial aspect of developing catalysts for this system is optimizing the metal and acid functions of heterogeneous catalysts to prevent unwanted byproduct generation and enhance toluene formation.[59,60] Dehydrogenation of MCH is an endothermic reaction accompanied by an increase in gas volume, making it more favorable at high temperatures and low pressures. However, most catalysts do not perform well under high-temperature conditions, primarily due to coke formation during dehydrogenation. Coke deposition can significantly reduce catalyst performance and even deactivate it, leading to an increase in byproducts, decreased selectivity, and reduced reactant conversion. Therefore, developing catalysts with good stability, product selectivity, and catalytic activity at relatively low temperatures is of great importance. The dehydrogenation of MCH is recognized as a structure-sensitive reaction, and in this context, the support structure greatly influences catalytic performance. Common supports, such as molecular sieves, metal oxides, composite metal oxides, and activated carbon, are generally suitable for MCH dehydrogenation catalysts. Several representative catalysts for this reaction are listed in Table 4.

For the catalytic dehydrogenation of MCH, similar to cyclohexane, Pt-based catalysts have been widely studied as Pt can effectively activate C–H bonds without splitting C–C bonds.[58] Different supports have been used for Pt-based catalysts in MCH dehydrogenation. Biniwale *et al.* used single metal oxides and perovskites, including $La_2O_3$, $ZrO_2$, $TiO_2$, $CeO_2$, $Fe_2O_3$, $Al_2O_3$, $MnO_2$, $LaNiO_3$, and $La_{0.7}Y_{0.3}NiO_3$ as supports for Pt in MCH dehydrogenation in a spray-pulsed reactor.[61] For the single metal oxide, the $Pt/La_2O_3$ shows the best activity of 21.1 mmol $g_{metal}{}^{-1}$ $min^{-1}$ at 350 °C. The performance can be further improved by using $LaNiO_3$ and $La_{0.7}Y_{0.3}NiO_3$ as supports, achieving hydrogenation formation rate of 30.3 mmol $g_{metal}{}^{-1}$ $min^{-1}$ and 45.3 mmol $g_{metal}{}^{-1}$ $min^{-1}$ at

Table 4 Catalysts for methylcyclohexane dehydrogenation

| Catalyst | Temp. (°C) | Space velocity | Conv. (%) | Sel. (%) | Ref. |
|---|---|---|---|---|---|
| $Mo_{10}$–$SiO_2$ | 400 | 92.4 $h^{-1}$ (WHSV) | | 90 | 78 |
| 8 wt% Ni-2 wt% Cu/ACC | 350 | | 25.78 | | 76 |
| Pt–Sn/$MgAlO_x$ | 300 | 9.2 $h^{-1}$ (WHSV) | 90.5 | ~100 | 69 |
| Ir/USY | 300 | 92.4 $h^{-1}$ (WHSV) | 13.1 | 89 | 65 |
| Pt-B1/$Al_2O_3$-600 | 350 | 23 $h^{-1}$ (WHSV) | 81.5 | >99.9 | 84 |
| Pt/$Al_2O_3$–$TiO_2$ | 400 | 5 $h^{-1}$ (WHSV) | 93 | 99 | 67 |
| Pt–Sn/$Al_2O_3$ | 300 | 600 000 mL $g^{-1}$ $h^{-1}$ (GHSV) | ~23.6 | ~99.99 | 85 |
| $Pt_3(Fe_{0.75}Zn_{0.25})/SiO_2$ | 320 | | 99 | >99.8 | 86 |
| $Ni_{20}AlO_x$ | 450 | 3 $h^{-1}$ (WHSV) | 77.4 | 85.6 | 87 |
| $Ga_{52}Pt/SiO_2$ | 450 | 1730 $h^{-1}$ (GHSV) | 15 | 85 | 19 |
| Pt/GAC-S | 300 | 5 $h^{-1}$ (WHSV) | 63 | | 88 |
| Zn/Ni–$SiO_2$ (Ni : Zn = 80 : 20) | 350 | 18 $h^{-1}$ (WHSV) | ~76 | 97 | 89 |
| Pt/$Y_2O_3$ | 350 | | 98 | ~100 | 62 |
| Pt/activated carbon | 300 | 28 $h^{-1}$ (WHSV) | 42 | >99 | 63 |
| Pt/pyrolytic waste tire char | 300 | 3 $h^{-1}$ (WHSV) | >95 | ~100 | 64 |
| Cu–Pt/S-1 | 350 | 4.6 $h^{-1}$ (WHSV) | 59.35 | 99.94 | 66 |
| Pt/$TiO_2$–$Al_2O_3$ | 400 | 5 $h^{-1}$ (WHSV) | 93.2 | 99.1 | 67 |
| Pt/Ce–Mg–Al–O | 350 | 9 $h^{-1}$ (WHSV) | 98.5 | >99.9 | 70 |

350 °C, respectively. The Pt/$La_{0.7}Y_{0.3}NiO_3$ also shows good selectivity, as no methane can be detected in the product. In a later work, $V_2O_5$ and $Y_2O_3$ were also used as supports for Pt.[62] The Pt/$Y_2O_3$ shows a high hydrogen formation rate of 703 mmol $g_{metal}^{-1}$ $min^{-1}$ at 350 °C, which is stable up to 150 min. The good activity is ascribed to the high dispersion of Pt on $Y_2O_3$ (31.5%) as determined by CO adsorption. Bao *et al.* used activated carbon as support for Pt in MCH dehydrogenation.[63] The surface of activated carbon was modified by oxidation with $HNO_3$ and reduction in $H_2$. Oxygen-containing groups, such as carboxylic acid groups, can be created on the surface of activated carbon during $HNO_3$ oxidation. After $H_2$ reduction, carboxylic acid and anhydride groups are removed while the thermal stable groups, such as lactone, phenol, and carbonyl, are preserved. The two-step modified catalysts show better activity than the unmodified or only oxidized catalysts. The difference in activity is ascribed to the different Pt dispersion caused by different surface groups. Liu *et al.* used pyrolytic waste tire char as support for Pt.[64] The waste tire char was purified in multi-steps before being used as the support. The organic impurities in the waste tire char were extracted by toluene refluxing, while the inorganic metal oxides were removed by $H_2SO_4$ washing. Then the support was activated in steam to create the porous structure. The supported catalysts with Pt loading 0.4–1 wt% show better activity than the catalyst with low Pt content, achieving MCH conversion over 95% with selectivity to toluene of nearly 100%.

Besides Pt, other noble-metal can catalyze MCH dehydrogenation. Vasudevan *et al.* compared the performance of USY-supported Ir, Pt, Pd, and Ni.[65] The activity follows the order of Ir ≫ Pt > Pd > Ni. The good activity of Ir/USY compared to Pt/USY is ascribed to the larger Ir nanoparticles formed due to the moderate interaction between Ir and USY. Larger particles have fewer kink sites which are active for the hydrogenolysis reaction and responsible for reduced selectivity. The deactivation of catalysts due to coke formation is related to the acidity of the catalyst. High total acidity of Pd/USY leads to severe coke formation and deactivation for this catalyst. The activity and selectivity of the noble-metal-based catalysts can be modified by adding promoters. Guo *et al.* improved the performance of Pt/S-1 in MCH dehydrogenation by doping Cu.[66] The catalysts were prepared by adsorption of metal precursors using silicalite-1 as support, followed by calcination. The Cu–Pt/S-1 exhibits better activity, selectivity, and stability than Pt/S-1 and Cu/S-1, showing an average $H_2$ formation rate of 288.9 mmol $g_{metal}^{-1}$ $min^{-1}$ with a MCH conversion of 59.35% at 350 °C. Formation of Pt–Cu alloy increases the dispersion of Cu, facilitates the charge transfer from Pt to Cu, decreases the electron density of Pt, and reduces the over-dehydrogenation and hydrogenolysis activity of the catalyst.

Lin *et al.* used $TiO_2$ to modify $Al_2O_3$ support for Pt/$Al_2O_3$ catalysts.[67] $TiO_2$ was deposited on $Al_2O_3$ by chemical vapor deposition. The Pt/$TiO_2$–$Al_2O_3$ with 11.5 wt% $TiO_2$ shows the best activity with an average MCH conversion of 93.2% and toluene selectivity of 99.1% at 400 °C. The $TiO_2$-coated $Al_2O_3$ combines the advantage of the high specific surface area of $Al_2O_3$ and strong interaction between Pt and $TiO_2$, which results in a good Pt dispersion of 57.5%. The surface density of weak acid sites is reduced by $TiO_2$ modification while the density of strong acid sites increases. At the same time, the electron density and H spillover on Pt are promoted. All these effects contribute to the increase in activity. Sekine *et al.* also studied the promotion effect of $TiO_2$ on Pt/$Al_2O_3$.[68] The repulsion between the π-coordination of toluene and electron-rich Pt on $TiO_2$–$Al_2O_3$ promotes the desorption of toluene and suppresses the further demethylation to benzene and methane or coke formation. Yang *et al.* used Pt–Sn/$MgAlO_x$ in MCH dehydrogenation.[69] The $MgAlO_x$ support was prepared from Mg–Al layered double hydroxides by calcination, and Pt and Sn were introduced into $MgAlO_x$ by impregnation. The activity and stability of Pt/$MgAlO_x$ were improved by the addition of Sn. X-ray photoelectron spectroscopy (XPS) results reveal the existence of electron transfer from Sn to Pt, which may be related to the improved activity by increasing the interaction between electron donor and Pt and thereby enhancing the reactant adsorption and product desorption. The good stability is

ascribed to the absence of acid sites in support, large pore size that reduces the diffusion resistance of the product, and a drain-off effect of Sn in assisting the migration of coke precursors to the support. In a later work, Pt supported on $CeMgAlO_x$ derived from layered double hydroxide precursors was employed in this reaction.[70] The catalysts with different Ce content were prepared by one-step co-precipitation and the introduction of Ce could promote the activity. The catalyst with Ce content of 14% shows the best activity with a hydrogen formation rate of 1358.6 mmol $g_{metal}^{-1}$ $min^{-1}$ due to the smallest Pt particle size of 2.28 nm and the largest specific surface area of 163.1 $m^2$ $g^{-1}$. This catalyst also shows a good stability as no coke formation and deactivation could be observed after 10 h on stream. The performance of Pt-based catalyst can also be improved by Mo, as reported by Boufaden *et al.*[71] Mo was introduced into $SiO_2$ support *via* sol–gel route before the introduction of Pt by impregnation. The catalyst with 8 wt% Mo shows the best activity. At higher Mo content (10.6 wt% and 12.7 wt%), $MoO_x$–Pt core–shell nanoparticles will form with a decline in activity. There is a linear correlation between the activity and the surface $Pt^0/Mo^{4+}$ ratio, indicating that both $MoO_2$ and $Pt^0$ sites participate in the reaction and the catalyst shows a bifunctional character of both metallic and acidic character. Sekine *et al.* reported that Mn could act as a promoter to improve the performance of $Pt/Al_2O_3$.[72,73] The $MnO_x$ selectively covers the unsaturated step facets on Pt which have high activity for demethylation, thus improving the dehydrogenation selectivity. Wasserscheid *et al.* studied the performance of Ga-rich, supported catalytically active liquid metal solution represented by $Ga_{52}Pt/SiO_2$ in MCH dehydrogenation.[19] Pt was dissolved in the Ga matrix, which is supported on $SiO_2$. Due to the low melting temperature of Ga, the alloy presents in the liquid state under reaction conditions and Pt in the atomically dispersed state. This catalyst shows higher activity and better stability than $Pt/SiO_2$ and achieves conversion of 15% with toluene selectivity of 85% at 450 °C. No significant deactivation can be observed for 75 h on stream, possibly due to the atomically dispersed and dynamic state of Pt in the liquid Ga matrix under reaction conditions.

The non-noble metals such as Ni and Mo have also been used in MCH dehydrogenation. Unsupported RANEY®-Ni shows some activity in this reaction.[74] Yolcular *et al.* studied the performance of $Ni/Al_2O_3$ with Ni content between 5–20 wt% in this reaction.[75] MCH conversion increases with the Ni content in the range studied and 20 wt% $Ni/Al_2O_3$ achieves MCH conversion of 92% at 440 °C. Biniwale *et al.* used NiCu supported on activated carbon cloth with different Ni/Cu ratios in this reaction.[76] The catalyst with 8 wt% Ni and 2 wt% Cu shows the best activity with a MCH conversion of 25.78%. The improved dehydrogenation activity and decreased hydrogenolysis activity are ascribed to decreases adsorption strength of hydrocarbon intermediates due to the formation of NiCu alloy. Takanabe *et al.* studied the effect of Zn on $Ni/Al_2O_3$ in MCH dehydrogenation.[77] The Zn in $NiZn/Al_2O_3$ occupies the low coordination corner and edge sites which are active for C–C dissociation and thereby improves the toluene selectivity. The rate of MCH dehydrogenation on $NiZn/Al_2O_3$ shows a ~0.5 order dependence on the $H_2$ partial pressure, indicating that the rate-determining step involves H-derived species. Density functional theory (DFT) calculations suggest that the exothermic toluene dissociative adsorption by losing one H atom from the methyl group occurs on the catalyst surface during MCH dehydrogenation. The adsorption of this species is so strong that the reverse hydrogenation and desorption to form toluene needs to overcome an energy barrier of 1.29 eV and becomes the rate-determining step. Therefore, the rate of dehydrogenation reaction shows a positive order dependence on the $H_2$ partial pressure. Boufaden *et al.* prepared Mo–$SiO_2$ catalysts with different Mo content *via* sol–gel route and tested them in MCH dehydrogenation.[78] $MoO_2$ formed after the reduction is ascribed to be the active phase for dehydrogenation. The catalyst with Mo/Si of 0.1 shows the best activity at 400 °C with toluene selectivity of 90%. Further increase in the Mo content causes the decrease of activity due to the decreased $MoO_2$ dispersion and formation of $MoO_3$. The acidity of the catalysts also increases with the increased Mo content, resulting in coke formation.

It is worth mentioning that in the cycle of the MTH system, in addition to the conventional fixed-bed reactor, some other promising reaction systems have been studied. Takise *et al.* reported low-temperature catalytic dehydrogenation of MCH by applying an electric field in the fixed-bed flow reactor.[57] Typically, 3 wt% $Pt/CeO_2$ catalyst demonstrates the highest MCH conversion under the electric field which exceeds the thermodynamic equilibrium at 150 °C. The enhanced conversion under the electric field is ascribed to the proton hopping on the catalyst and the suppressed reverse hydrogenation reaction in the presence of electric field.

### 2.3 Polycyclic aromatic hydrocarbons

Decalin/naphthalene is one of the widely studied systems with a theoretical hydrogen capacity of 7.3 wt% and dehydrogenation heat of 63.9 kJ per mol $H_2$. Naphthalene exists as a solid at ambient conditions. These factors complicate the implementation of the storage system and hinder practical applications to some extent.[9] Despite these disadvantages, decalin is considered an excellent hydrogen source for fuel cells due to its high energy and power densities, low energy consumption, safety, economy, and ease of operation. Consequently, it holds promise for applications such as hydrogen sources in fuel-cell vehicles.[79] Catalysts based on Pt-group metals exhibit exceptional performance in decalin dehydrogenation, with size-dependent activity. This underscores the importance of controlling Pt particle size and achieving ideal dispersion by adjusting the catalyst support for the dehydrogenation process.[80] Studies have shown that Pt atoms with a low coordination number are more efficient than those with a high coordination number, as they have a lower energy barrier.[81] Nevertheless, the dehydrogenation product of decalin, naphthalene, strongly adsorbs on the Pt surface. A few studies show that the kinetics of decalin dehydrogenation is limited by naphthalene desorption.[79,82] Changing the adsorption behaviour of the reactant is crucial, and adjusting the

electronic structure of Pt by modifying the support is an effective strategy. Commonly used catalyst supports include activated carbon and metal oxides. Activated carbon is particularly attractive due to its low cost and good performance. Sebastián *et al.* reported that 4 wt% Pt/C could effectively catalyze decalin dehydrogenation.[83]

Tuo *et al.* improved the dehydrogenation performance of Pt/CNT by modifying the surface of CNT with nitrogen and oxygen functional groups.[90] Recently, Tuo *et al.* used $MgAl_2O_4$ to modulate the electronic structure of Pt nanoparticles. The prepared catalyst, $Pt/MgAl_2O_4$, exhibited record-high dehydrogenation activity, which is almost as twice as the activity of Pt/CNF[91] (Fig. 2). Some bimetallic catalysts have also been studied as they not only show distinctly different electronic and chemical properties from Pt itself, but also explore ways to reduce catalyst costs. Qi *et al.* designed Pt–Ni bimetallic catalysts supported on active carbon, with the bimetallic catalyst 1Ni–1Pt/C displaying higher dehydrogenation activities than the monometallic catalysts.[92] Apart from Pt-based catalysts, other metal-based catalysts have shown promise for the reaction. Kim *et al.* found that decalin is more easily dehydrogenated on Pt/C, while tetrahydronaphthalene is more easily dehydrogenated on Pd/C.[93] The difference in catalytic activity and selectivity can be attributed to the distinct structural properties and adsorption mode preferences between Pd and Pt catalysts during dehydrogenation. Non-precious metal-based catalysts have also been studied. For example, Al-Muntaser *et al.* reported that a Ni-based catalyst, nickel(II) stearate, reached the maximum decalin conversion rate of 21.95%.[94] It is worth mentioning that some studies have found that the microwave effect appears in the process of tetrahydronaphthalene, but in the dehydrogenation of decalin, microwave heating is of little use to improve the catalytic performance.[95]

Perhydrodibenzyltoluene (H18-DBT) is another promising LOHC with a hydrogen storage content of 6.2 wt%. Mixtures of isometric benzyltoluenes and dibenzyltoluenes are used as heat-transfer oil in industry and produced on a large scale. The dehydrogenation of H18-DBT undergoes different

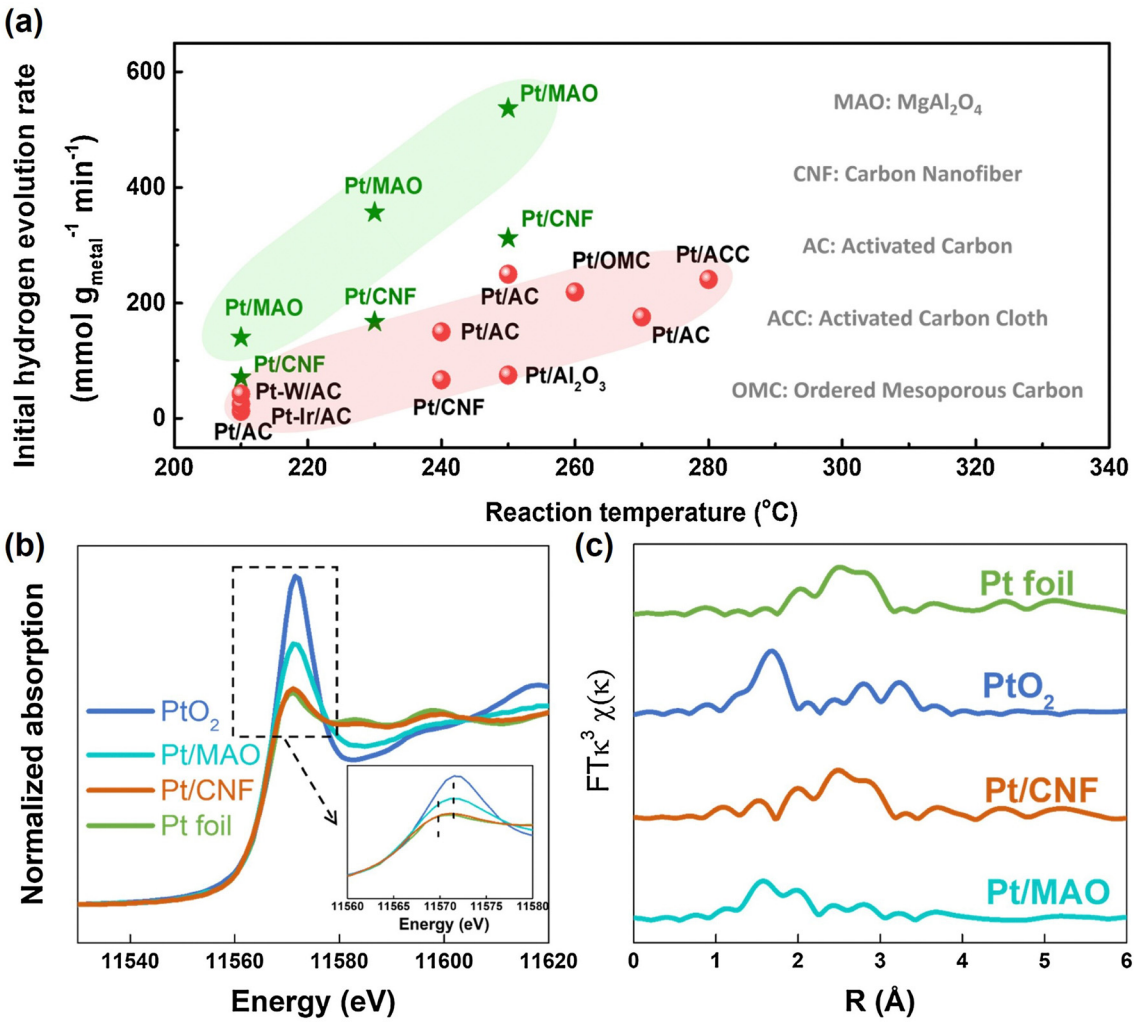


Fig. 2 (a) Comparison of dehydrogenation activity of $Pt/MgAl_2O_4$ and Pt/CNF with other catalysts at different temperatures. (b) Normalized Pt $L_3$-edge XANES spectra and (c) $k^3$-weighted Fourier transform EXAFS spectra ($L_3$-edge) of Pt for Pt foil, $PtO_2$, Pt/CNF, and $Pt/MgAl_2O_4$.[91] Modified with permission from ref. 91. Copyright (2021) Elsevier Inc.

intermediates, including H12-DBT, H6-DBT, to dibenzyltoluene (H0-DBT). This reaction can be catalyzed by Pt and Pd-based catalysts. Wasserscheid *et al.* compared the performance of Pt/C, Pt/$Al_2O_3$, Pt/$SiO_2$, Pd/C, and Pd/$Al_2O_3$ in H18-DBT dehydrogenation.[96] Pt-Based catalysts show higher activity than Pd-based catalysts and Pt/C exhibits the best activity among the catalysts tested, achieving 71% degree of dehydrogenation at 270 °C at catalysts loading of 0.15 mol%. In a later work, The reversible hydrogen storage in a hot pressure swing reactor using H18-DBT and dibenzyltoluene cycle catalyzed by Pt/$Al_2O_3$ was demonstrated by Wasserscheid *et al.*[97] The reactor was operated at 290–310 °C. At this temperature, both hydrogenation and dehydrogenation can take place catalyzed by Pt/$Al_2O_3$. The reaction direction is changed by the hydrogen pressure. Hydrogenation is achieved at high pressures, while dehydrogenation is achieved at low pressures. Between the change of reaction direction, the reactor does not need to be cooled, making this system suitable for the fast start-up. Since the exothermic hydrogenation reaction can operate at a temperature slightly higher than the endothermic dehydrogenation, a heat storage system can be applied to utilize the hydrogenation heat for dehydrogenation. Qi *et al.* studied the influence of surface hydroxyl groups and oxygen vacancies of $Al_2O_3$ on the performance of Pt/$Al_2O_3$.[98] The surface of $Al_2O_3$ was modified by $H_2$ or $O_2$ plasma treatment. Surface treatment by $H_2$ increases the surface oxygen vacancies, while treatment by $O_2$ increases the surface hydroxyl groups.

The catalysts treated by $O_2$ plasma show improved hydrogenation and dehydrogenation activity, selectivity, and long-term performance. The high side reaction activity and poor stability for the catalyst pretreated by $H_2$ plasma are due to the high proportion of low coordinated Pt species. Bessarabov *et al.* reported that the activity and selectivity of Pt/$Al_2O_3$ could be promoted by adding Mg dopants in $Al_2O_3$ support.[99] The addition of Mg decreases the acidic property of the $Al_2O_3$ support, improves the stability of the catalyst, and promotes the desorption of H0-DBT. Kang *et al.* studied the dehydrogenation of H18-DBT on the Pt-based subsurface alloys (Pt/M/Pt(111), where M = Pd, Cu, or Ni) using DFT calculation.[100] The results show that the rate-determined step is the first step of dehydrogenation in the middle ring of H18-DBT for all the surfaces studied. It is proposed that the hydrogen adsorption strength might be a descriptor for the dehydrogenation activity since the d-band centers and reaction energies for the rate-determining step correlate to the hydrogen adsorption energy. The Pt/Pd/Pt(111), tensile-strain-applied Pt/Pd/Pt(111), and tensile-strain-applied Pt/Cu/Pt(111) might be promising catalysts due to the low hydrogen adsorption energy of less than or equal to −0.6 eV.

### 2.4 N-Heterocyclic molecules

The lower endothermicity of heterocyclic organic liquids compounds is conducive to the dehydrogenation process, which means that heterocycles have the potential as hydrogen storage carriers. However, their disproportion, alkyl transfer, degradation by C–N cleavage, and other side reactions affect their application in industry.[101] The introduction of nitrogen atoms into the conjugated structure of aromatic hydrocarbons has been shown to effectively lower the temperature required for dehydrogenation reactions.[16,102–104] Researchers have expanded the LHC system with a variety of N-heterocycles, including carbazole,[105] benzpyrole,[106] pyridine,[107] benzopyridine,[108] and so on, among which the most studied is *N*-ethylcarbazole. Noble metal-based catalysts, such as Pd[109] and Pt,[110] have garnered the most attention for their role in the dehydrogenation of N-heterocycles. To assess the effectiveness of these N-heterocycles within the LHC system, researches rely on various performance indicators, including hydrogen storage capacity, operating conditions, conversions, and turnover frequency (TOF).

**2.4.1 Dodecahydro-*N*-ethylcarbazole (DNEC)/*N*-ethylcarbazole (NEC).** Focusing on N-heterocycles, carbazole and its derivatives have emerged as primary research compounds for LHC systems, particularly NEC. In recent years, the system of DNEC/NEC has drawn considerable interest in LHC studies (Table 5).[111–114] Unlike cyclohexane and MCH, the introduction of N atom efficiently reduces the dehydrogenation temperature, potentially lowering the hydrogen storage cycle temperature to below 200 °C.[115] A single DNEC molecule can generate six hydrogen molecules, offering a high hydrogen storage capacity of up to 5.8 wt%.[116] During the dehydrogenation process, partially hydrogenated intermediates such as tetrahydro-*N*-ethylcarbazole (4H-NEC) and octahydro-*N*-ethylcarbazole (8H-NEC) are produced together with NEC. The fact that all products and reactants remain liquid in this hydrogen storage system offers a significant advantage for application.[117] Like other LHC, transition metals serve as catalysts for DNEC dehydrogenation. By altering the metal species and catalyst support, the selectivity and activity of catalysts can be controlled and adjusted. The most commonly used metals include Pd, Pt, and Ru, among others. Although several studies have compared different noble metals,[117,118] there is no definitive rule determining the best catalyst.

**2.4.2 Catalysts for DNEC dehydrogenation reaction.** Since the first report by Smith *et al.* in 2009,[119] Pd-based catalysts have been the most commonly studied catalysts in DNEC dehydrogenation. To maximize the atomic efficiency of precious metals, it is necessary to improve their dispersion. At present, different synthesis strategies have been employed to drive Pd atoms into highly dispersed state.[120–122] Smith *et al.* studied the structure sensitivity of DNEC dehydrogenation over Pd catalysts in 2011.[123] According to experimental results and DFT calculations, multiple catalytic sites were required and the heat of adsorption depended on the surface structure. In 2017, Yang *et al.* focused on the kinetic study and revealed that there were three stages in the dehydrogenation of DNEC.[124] The rate-limiting step is considered to be the third step, namely 4H-NEC dehydrogenated to NEC. The supports of Pd-based catalysts show significant impacts on the catalytic activity. $SiO_2$[119] and $Al_2O_3$[125] are the most used supports. Mesoporous silica,[113] reduced graphene oxide (rGO),[120] CNT,[121] and other supports have also been applied. Fu *et al.* reported a new strategy of using PdO as the active site and activated carbon as the substrate.[126] PdO/AC showed great performance with a conversion of 100% and yield of 95.8% at 100 °C. Several researches

Table 5 Catalysts for NEC hydrogeneration and DNEC dehydrogenation

| Reaction | Catalyst | Conditions | Time (h) | Conv./yield (%) | Cycles | $H_2$ stored (wt%) | Ref. |
|---|---|---|---|---|---|---|---|
| Hydrogenation | $LaNi_{5.5}$ | 453 K, 7 MPa | 8 | 96.8 | 9 | 5.5 | 145 |
| | $Ni_{70}$/AlSiO | 423 K, 7 MPa | 1.5 | 100 | | ~5.7 | 112 |
| | Pd/$Al_2O_3$-$YH_3$ | 453 K, 10 MPa | 2.0 | 94.8 | 3 | 5.5 | 114 |
| | Co-B/$Al_2O_3$-$YH_{3-x}$ | 453 K, 10 MPa | 2.0 | >94 | 3 | 5.5 | 135 |
| | RuPd/LDH | 393 K, 6 MPa | ~1.3 | 99.3 | 8 | 5.75 | 147 |
| | Ru/$YH_3$ | 363 K, 1 MPa | | 100 | | | 146 |
| Dehydrogenation | $LaNi_{5.5}$ | 473 K, 0.1 MPa | 6 | 91.7 | 9 | 5.5 | 145 |
| | h-BNNS | 393 K | | 74 | | | 111 |
| | Pd/KIT-6 | 453 K, 0.1 MPa | 6.0 | 97.4 | 10 | 5.59 | 113 |
| | Pd/$Al_2O_3$-$YH_3$ | 473 K, 0.1 MPa | 4.0 | 94.8 | 3 | 5.5 | 114 |
| | Pt/$TiO_2$ | 453 K, 0.1 MPa | 7 | 100 | | 5.38 | 117 |
| | Pd/$TiO_2$ | 453 K, 0.1 MPa | 7 | 100 | | 5.25 | 117 |
| | Rh/$TiO_2$ | 453 K, 0.1 MPa | 7 | 100 | | 3.72 | 117 |
| | Au/$TiO_2$ | 453 K, 0.1 MPa | 7 | 75.7 | | 1.59 | 117 |
| | Ru/$TiO_2$ | 453 K, 0.1 MPa | 7 | 14.1 | | 0.42 | 117 |
| | Pd/$Al_2O_3$ | 453 K, 0.1 MPa | 7 | 100 | | 4.64 | 117 |
| | Pd/rGO-EG | 443 K, 0.1 MPa | 12.0 | 100 | 5 | 5.49 | 120 |
| | Co-B/$Al_2O_3$-$YH_{3-x}$ | 473 K, 0.1 MPa | 7.0 | >94 | 3 | 5.5 | 135 |
| | $Pd_3Au_1$/$SiO_2$ | 453 K, 0.1 MPa | 8.0 | 100 | | 5.7 | 148 |
| | $Pd_3Ni_1$/$SiO_2$ | 453 K, 0.1 MPa | 8.0 | 100 | | 5.63 | 105 |
| | $Pd_3Cu_1$/$SiO_2$ | 453 K, 0.1 MPa | 8.0 | 100 | | 5.47 | 105 |
| | Pd/$MgAl_2O_4$ | 453 K, 0.1 MPa | | 98.3 | | | 149 |
| | Pd/$MoO_3$ | 473 K, 0.1 MPa | 1.5 | | | 5.8 | 136 |
| | $Pd_1Co_1$/$Al_2O_3$ | 473 K, 0.1 MPa | 8.0 | 100 | | 5.52 | 150 |

using mesoporous materials in the past years are noteworthy. Bai *et al.* prepared Pd nanocatalysts (Pd/KIT-6) *via* inorganometallic chemical adsorption (ICA) and sonochemical reduction.[113] Typically, the Pd dispersion of Pd/KIT-6 could reach 97% and the dehydrogenation efficiency maintained above 95% after 10 cycles. Bai *et al.* performed attempt with highly dispersed Pd/SBA-15 catalysts *via* glow discharge plasma.[127] After 7 cycles at 180 °C, the dehydrogenation efficiency of Pd/SBA-15 remained above 97%. Furthermore, metal–organic frameworks (MOFs) could also be used as the precursors of Pd catalysts.[128] Recently, Ma *et al.* systematically studied the structure sensitivity of Pd catalysts with different sizes.[129] The results showed that Pd single-atom sites were ineffective for the dehydrogenation reaction. With the help of bulk-sensitive X-ray absorption spectroscopy and single-atom sensitive electron microscopy, the authors confirmed that the fully exposed atomic-layered palladium clusters, with an average Pd–Pd coordination number of ~4.4, performed the best activation of reactants and desorption of products.

Pt catalysts are another kind of catalyst widely used in dehydrogenation reactions, with overall performance close to Pd catalysts. The reaction mechanism of Pt(111) is very similar to Pd(111). From 173 K, DNEC undergoes molecular adsorption at Pt(111) and stepwise dehydrogenation to NEC while heating to 380 K.[130] Meanwhile, C–N bond will be broken above 390 K, ~60 K higher than Pd(111). $Al_2O_3$ is the commonly used support for Pt-based catalysts.[131] Wasserscheid *et al.* first applied egg-shell catalysts in the dehydrogenation of DNEC.[132] An inert non-porous α-alumina core and an active, porous γ-alumina shell of defined thickness were impregnated with Pt by a hybrid sol–gel suspension process. Their results confirm that pore diffusion strongly affects the dehydrogenation reaction in almost all commercial catalysts. Recently, $TiO_2$ has been applied in Pt-based catalysts.[117,133] The catalytic activity of the noble metal catalysts on $TiO_2$ followed the trend of Pt > Pd > Rh > Au > Ru.[117] Jiang *et al.* proved the introduction of the Si–O–Ti species could strengthen the metal-supporting interaction and increase the oxygen vacancy concentration for efficient dedrogenation.[134]

At present, most catalysts used in the dehydrogenation reaction are noble metal-based catalysts. Non-noble metal catalysts have also been explored due to the scarcity of noble metals. Fu *et al.* reported that high crystallinity hexagonal boron nitride nanosheets (h-BNNS) performed high catalytic efficiency in the dehydrogenation of DNEC due to the synergistic effect of the nanoporous structure and highly ordered crystalline pattern.[111] Zheng *et al.* prepared a two-direction catalyst, namely Co-B/$Al_2O_3$-$YH_3$-*x*, for reversible hydrogen storage in NEC/DNEC,[135] which is the first non-noble metal catalyst used for both NEC hydrogenation and DNEC dehydrogenation reaction. Synthesis of bimetallic catalysts is also an important strategy for dehydrogenation catalysts, which usually have catalytic activity for both hydrogenation and dehydrogenation.[114,136,137] You *et al.* investigated the effect of interheteromolecular hyperconjugation on heterogeneous (de)hydrogenation catalyzed by Rh–Pd loaded silicon–aluminium oxide supports (Rh–Pd/SAO).[138] Sun *et al.* synthesized reusable bimetallic Pd–Rh nanoparticle catalysts.[139] The optimized catalyst performs a hydrogen release of 5.48 wt% in 4 h and the maximum hydrogen uptake of 5.43 wt% in 1 h. The good activity is ascribed to the synergistic effect between Pd and Rh nanoclusters.

**2.4.3 Catalysts for NEC hydrogenation reaction.** The most used catalysts for the hydrogenation reaction are Ru-based catalysts.[140–142] The mechanism of hydrogenation was first discussed by Tsang *et al.* in a stepwise manner over metal catalysts.[143] It is concluded that steric constraints make the catalyst inefficient in terms of activity and selectivity. Chen *et al.* reported a Ru single-atoms supported on BEA zeolite

 

catalyst with a hydrogen uptake of 5.69 wt% (Fig. 3).[144] The synergistic effects of Ru single atoms and BEA zeolite (the strong acid sites of zeolites) can lower the activation energy and accelerate the hydrogenation rate. Zheng *et al.* applied rare earth metals in the hydrogenation of NEC.[145] It is reported that the sub-μm $LaNi_{5.5}$ particles can catalyze the reversible hydrogen storage in NEC/DNEC below 473 K, which stem from the change of H concentration in the $LaNi_5$-H solid solution. Notably, the combination of Ru single atoms with $YH_3$ can achieve complete hydrogenation of NEC at 363 K and 1 MPa hydrogen.[146]

**2.4.4 Indole.** Recently, significant attention has been paid to indole and its derivatives, which are low in price and show the potential for application in LHC. Compared with other N-heterocycles, Indole has great application prospects because of the high hydrogen gravimetric capacity (6.4 wt%). There are still lots of problems in the dehydrogenation process. For instance, octahydroindole is susceptible to ring-opening reactions to form other products, which seriously affects the cycling performance and hydrogen production efficiency.[106] The most used catalysts for dehydrogenation include Pt[151] and Pd[152] based catalysts. The dehydrogenation mechanism has not been fully revealed. Ouma *et al.* used *Ab initio* calculations to study the adsorption properties of reactants and products on a Pt(111) surface.[151] The calculated reaction energies explain that the dehydrogenation of octahydroindole to indole will either select a reaction pathway through indoline or not. Papp *et al.* performed a systematic study on indole to reveal the surface chemistry of indole and possibly tweak the deprotonation reaction and temperature.[153] The results indicate that methyl has a strong impact on the stability of reaction intermediates, which can be used to tailor more suitable LHC systems. Besides, with the hydrogen gravimetric density of 5.23 wt%, *N*-ethylindole is also used in the LHC system.[17]

**2.4.5 Other N-heterocycles.** The use of quinoline[108] and pyridine[103] in LHC has also been reported. In 2019, Beller *et al.* applied Ni-based nanocatalysts in reversible hydrogenation and dehydrogenation reactions of quinoline and its homologues.[108] The hydrogen uptake/release properties could be maintained after three consecutive cycles under optimized conditions. Lim *et al.* detailed a large-scale (1000 $m^3$ per h $H_2$) LHC dehydrogenation system and evaluated 2-(*N*-methylbenzyl)pyridine in the process simulation.[154] These results illustrate the promise of N-heterocycles in LHC systems.

## 3. Methanol

The consumption of fossil fuels increases the emission of carbon dioxide ($CO_2$). Carbon capture and utilization (CCU) is an effective way to reduce the excessive $CO_2$ concentration in the atmosphere.[155] Furthermore, the synthesis of methanol from

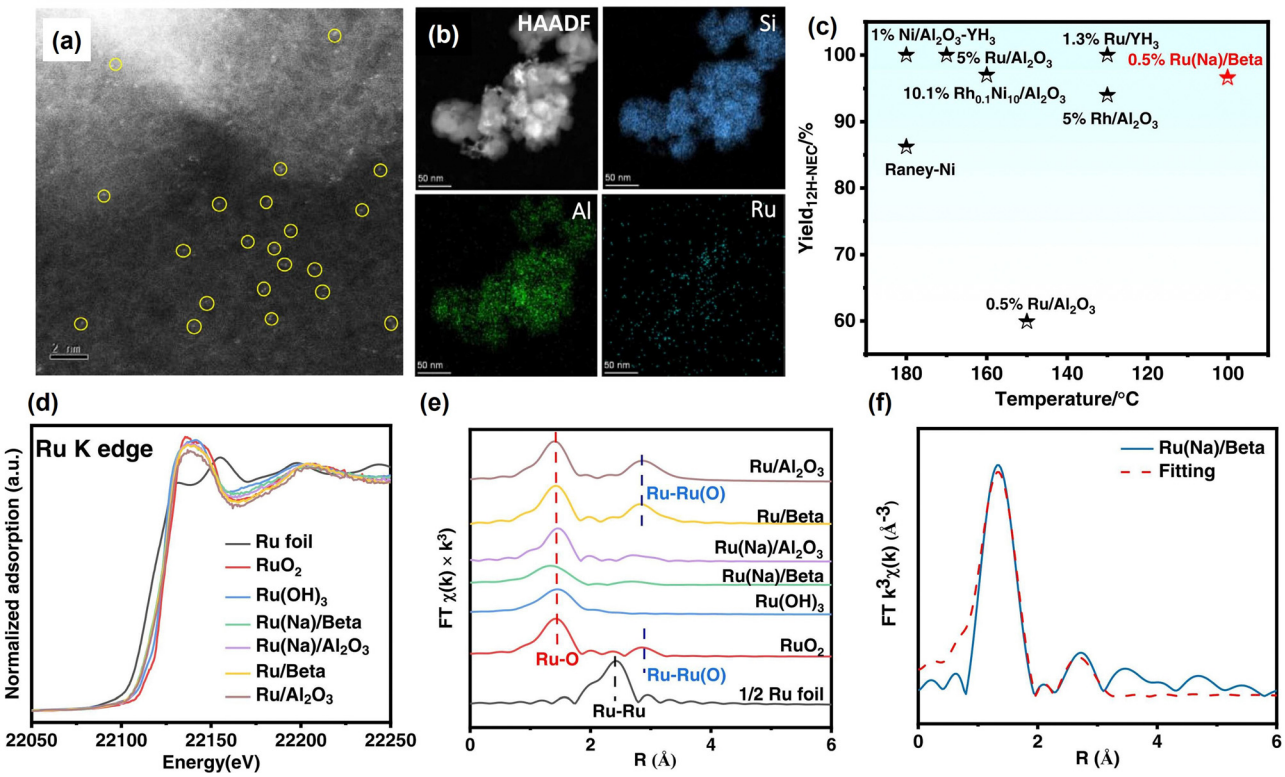


Fig. 3 (a) Aberration-corrected HAADF-STEM image and (b) corresponding element mapping images of Ru(Na)/Beta. (c) Comparison of the performance of different catalysts in the hydrogenation of *N*-ethylcarbazole. (d) Ru K-edge XANES spectra, (e) $k^3$-weighted Fourier transform Ru K-edge EXAFS spectra, and (f) EXAFS fitting curve of Ru(Na)/Beta.[144] Modified with permission from ref. 144. Copyright (2022) Elsevier Inc.

$CO_2$ and hydrogen is a feasible way to reduce the concentration of $CO_2$ in the atmosphere.[156] Methanol has been proposed to replace fossil fuels partially.[157] From another perspective, it is possible to use methanol as LHC. Methanol can store 12.6 wt% $H_2$ in each molecule, which is higher than cyclohexane and other LHC substances. Methanol is a stable liquid substance at room temperature that can be easily transported. Hydrogen can be generated from methanol through steam reforming as shown in the following equation.

$$CH_3OH + H_2O = CO_2 + 3H_2 \quad \Delta H^{\theta}_{289K} = +49.7 \text{ kJ mol}^{-1}$$

MSR reaction is endothermic and heat from an external source is required. On the other hand, due to the absence of C–C bond in methanol molecule, its steam reforming can be achieved at a relatively low temperature (150–350 °C) compared to other alcohols and hydrocarbons. During MSR, the reaction of methanol decomposition and water–gas shift reaction[158] might also occur.

$$CH_3OH = CO_2 + 2H_2 \quad \Delta H^{\theta}_{289K} = +90.7 \text{ kJ mol}^{-1}$$

$$CO + H_2O = CO_2 + H_2 \quad \Delta H^{\theta}_{289K} = +41.2 \text{ kJ mol}^{-1}$$

The main drawback of methanol decomposition is the byproduct of this process, CO, which can poison some catalysts. Therefore, reducing the CO content in the effluent is one of the targets of concern. In recent years, there have been many reports on the dehydrogenation of methanol to hydrogen. However, in many catalytic reactions, less than three molecules of hydrogen can be obtained from a single molecule of methanol. The by-products, $CH_4$ and CO, will reduce the purity of the hydrogen product, which brings additional problems of hydrogen purification.

### 3.1 Heterogeneous catalysis for MSR

Catalysts play a crucial role in methanol steam reforming by increasing the reaction rate. Heterogeneous catalysts, in particular, have garnered attention in this area due to their benefits in large-scale applications, such as good stability, simple separation, and reusability. A wide range of catalysts, including Cu, Pt, Pd, and metal oxide-based catalysts, have been explored for their potential use in MSR (Table 6).

**3.1.1 Cu-Based catalyst.** Cu-Based catalysts are widely used in heterogeneous catalysis, such as water–gas shift reaction and methanol synthesis from carbon monoxide, and also show good activity in methanol steam reforming.[159] Cu is usually employed together with ZnO to construct active catalysts. The synergistic effect between Cu and ZnO has been widely studied in different reactions.[160] $Cu^0$–ZnO contact,[160–162] $Cu^+$ dispersed in ZnO,[163,164] formation of CuZn alloy,[165,166] strained Cu induced by interaction with ZnO,[167] as well as charge transfer between Cu and ZnO[168] are proposed to explain the promotion effect of ZnO. $ZrO_2$ and other supports have also been used to construct active Cu catalysts and show good performance. Different promoters, including metal oxides and metals, have been added into Cu catalysts as structure or electron promoters to improve the performance. Cu has a low Tammann temperature of ~405 °C and sinters easily under high reaction temperatures, leading to the deactivation of catalysts. Coking is another influence that deactivates the catalysts. Cu-Based catalysts are sensitive to sulfur even in a few ppm levels and show pyrophoric behaviour when exposed to air.[169] Overcoming these disadvantages will make Cu catalysts more practical in industry applications. The influence of supports, preparation methods, pretreatment conditions, and introduction of different promoters on the structure and activity of the Cu-based catalysts will be introduced in the following section.

*Cu/ZnO and Cu/$Al_2O_3$ catalysts.* Among copper catalysts, the most-studied catalysts are Cu/ZnO and Cu/$Al_2O_3$ based catalysts. Ressler *et al.* studied the structure change of Cu/ZnO during reduction and MSR using *in situ* X-ray diffraction (XRD) and X-ray absorption spectroscopy (XAS).[167] Reaction results show that catalysts reduced with the mixture of $H_2$ (2.5%) and $H_2O$ (3%) exhibit lower CO selectivity than catalysts reduced by $H_2$ alone (2%) at similar methanol conversion levels. The effect of reduction followed by an oxidation cycle was also studied. The addition of oxygen in the reactant stream transfers the metallic Cu into $Cu^+$ and $Cu^{2+}$ with the loss of catalytic activity. Besides, the methanol conversion and $CO_2$ selectivity increase with repeated oxidation/reduction cycle. *In situ* XRD shows that the lattice parameters of Cu and ZnO increase after the oxidation/reduction cycle, indicating an expansion of the unit cell. XAS shows that the medium-range structure disorder of Cu increases with a reduced Zn concentration in Cu clusters after repeated oxidation and reduction. Zn migrated out of Cu clusters and formed ZnO on the Cu surface with increased interface interaction between Cu and ZnO during this process. The influence of aging during preparation on the structure and activity for the Cu/ZnO catalyst was studied by Ressler *et al.*[170,171] Four Cu/ZnO catalysts with different aging times (0, 15, 30, and 120 min) were investigated. An amorphous precursor was obtained with short (15 min) or without aging, while crystalline hydroxycarbonate was obtained after a long aging time. For the catalysts after calcination, the longer aging time results in a smaller CuO crystallite size and a lower reduction temperature. *In situ* XRD and XAS show that the microstrain in Cu increases with the aging time. The high Cu surface area and increased microstrain both contribute to the high reaction activity for the catalysts with long aging time. Mendes *et al.* studied the influence of surface area and polarity of ZnO on the activity of Cu/ZnO.[172] Different calcination temperatures (300–400 °C) were used to control the ZnO surface area, while the polarity (002) surface ratio was adjusted by using different Zn precursors. A higher calcination temperature results in a lower surface area of ZnO and Cu, thus a decreased activity. Cu species on the polar surface of ZnO can be reduced more easily, as caused by the strong interaction between Cu and polar facets. The results suggest that the $CO_2$ selectivity increase with the polar surface ratio of ZnO, indicating that the Cu–ZnO polar interface is more selective for MSR. Xu *et al.* studied the influence of the activation process on the catalytic

Table 6 Catalysts for methanol steam reforming

| Catalyst | Temp. (°C) | Pressure (MPa) | Space velocity | Methanol conv. (%) | $CO_2$ sel. (%) | CO sel. (%) | Ref. |
|---|---|---|---|---|---|---|---|
| 15 wt% Cu/ZnO | 300 | 0.1 | 1.4 $h^{-1}$ (WHSV) | 82.2 | | ~2 | 172 |
| $Cu/ZnO/Al_2O_3$ | 225 | 0.1 | 6 $h^{-1}$ (WHSV) | 67.0 | | 0.07 | 173 |
| $Cu/ZnO/Al_2O_3$ | 263 | 0.1 | 25 714 $h^{-1}$ (GHSV) | 58 | | 2.5 | 204 |
| 10 wt% Cu/ZnO–Al | 250 | 0.1 | 15.3 $h^{-1}$ (WHSV) | 57 | ~98.7 | | 235 |
| 5% MgO–$Cu/ZnO/Al_2O_3$ | 200 | 0.1 | 3.84 $h^{-1}$ (WHSV) | ~70 | | ~1 | 174 |
| 30% Ni–$Cu/Al_2O_4$ | 300 | 0.1 | 0.9 $h^{-1}$ (WHSV) | 96.89 | | 33.5 | 181 |
| Ru–$Cu/ZnO/Al_2O_3$ | 240 | 0.1 | 4 $h^{-1}$ (WHSV) | 95 | | 1.97 | 175 |
| $CuNiAlO_x$ spinel oxide | 255 | 1 | 1.09 $h^{-1}$ (WHSV) | ~92 | | <0.8 | 180 |
| CuFeMg/$\gamma$-$Al_2O_3$/Al mesh | 250 | 0.1 | 3000 mL $g_{cat}^{-1}$ $h^{-1}$ (GHSV) | 93.5 | | ~4 | 199 |
| $CuTi_{1.9}/\gamma$-$Al_2O_3$/Al mesh | 275 | 0.1 | 4000 mL $g_{cat}^{-1}$ $h^{-1}$ (GHSV) | ~100 | | ~3 | 236 |
| 20 wt% $Cu/ZrO_2$–$Al_2O_3$ | 240 | 0.1 | 3.8 $h^{-1}$ (WHSV) | 95 | | 0.37 | 185 |
| $Cu/ZrO_2$-10 wt% $SiO_2$ | 260 | 0.1 | 5 $h^{-1}$ (WHSV) | 73 | | <0.1 | 186 |
| $Cu/ZnO/ZrO_2$ | 300 | 0.1 | 24.9 $h^{-1}$ (WHSV) | 84 | | 1.6 | 203 |
| $Cu/ZnO/ZrO_2/Al_2O_3$ | 305 | 0.1 | 0.77 $h^{-1}$ (WHSV) | 80 | | 3.6 | 205 |
| $CuO/ZnO/ZrO_2/Al_2O_3$ | 270 | 0.1 | 8.7 $h^{-1}$ (WHSV) | ~80 | | ~0.7 | 237 |
| $CuO/ZnO/CeO_2/ZrO_2/Al_2O_3$ | 270 | 0.1 | 8.7 $h^{-1}$ (WHSV) | 90.5 | | 0.91 | 238 |
| $CuO/ZnO/ZrO_2/Al_2O_3$ | 270 | 0.1 | 8.7 $h^{-1}$ (WHSV) | 92.4 | | 0.97 | 238 |
| 2 wt% $In_2O_3$–$Cu/ZnO/ZrO_2$ | 400 | 0.1 | 29.1 $h^{-1}$ (WHSV) | 79 | | 1.7 | 239 |
| $CuPd/ZrO_2$ | 260 | 0.1 | 1.4 $h^{-1}$ (WHSV) | ~86 | | 5 | 187 |
| $CuZnGaO_x$ | 150 | 0.1 | 0.12 $h^{-1}$ (WHSV) | 36 | | <1 ppm (Conc.) | 189 |
| $Cu/CeO_2$ | 200 | 0.1 | 6.2 $h^{-1}$ (WHSV) | 7.4 | | <0.5 | 240 |
| $Ce_{0.8}Cu_{0.2}O_x$ | 300 | 0.1 | 36 000 mL $g_{cat}^{-1}$ $h^{-1}$ (GHSV) | ~99 | | ~1 | 241 |
| Ce–Cu/KIT-6 | 325 | 0.1 | 2 $h^{-1}$ (WHSV) | 96.8 | | 3.7 | 198 |
| Cu–Ce/SBA-15 | 250 | 0.1 | 6 $h^{-1}$ (WHSV) | ~82 | | ~1.2 | 197 |
| $ZrO_2$–$CeO_2$–Cu/KIT-6 | 300 | 0.1 | 2 $h^{-1}$ (WHSV) | 96 | | 0.7 | 242 |
| Cu-MCM-41 | 300 | 0.1 | 2838 $h^{-1}$ (GHSV) | 69.9 | | 16.4 | 243 |
| 10% $Cu/\gamma$-$Al@ZnAlO_x$ | 300 | 0.1 | 800 $h^{-1}$ (GHSV) | 99.98 | | 0.92 (Conc.) | 176 |
| CeCuZn/CNTs | 300 | 0.1 | 7.5 $h^{-1}$ (WHSV) | 94.2 | | 2.6 | 244 |
| $CuIn/SiO_2$ | 260 | 0.1 | 18 $h^{-1}$ (WHSV) | 71.20 | | 0.08 | 195 |
| CuZn/MCM-41 | 300 | 0.1 | 2.85 $h^{-1}$ (WHSV) | 88 | | <1.8 | 196 |
| $Ru_1/CeO_2$ | 350 | 0.1 | 6 $h^{-1}$ (WHSV) | 25.6 | 97.8 | | 206 |
| $Pt/NiAl_2O_4$ | 210 | 2.9 | 2.94 $h^{-1}$ (WHSV) | >99.9 | 99.72 | | 211 |
| 0.5 wt% Zn–Pt/MoC | 160 | 0.1 | 1.8 $h^{-1}$ (WHSV) | 65.9 | | 0 | 210 |
| Pt–SnO/MIL-101(Cr) | 300 | 0.1 | 1.8 $h^{-1}$ (WHSV) | 92 | | 3.4 | 245 |
| KOH-$Pt/Al_2O_3$ | 230 | 0.5 | 360 $h^{-1}$ (WHSV) | | | <1 | 214 |
| $Pt/In_2O_3/Al_2O_3$ | 350 | 0.1 | 3 $h^{-1}$ (WHSV) | 100 | | 3.2 | 246 |
| $In_2Pt$ | 400 | 0.1 | 7 $h^{-1}$ (WHSV) | | | 0.2 | 247 |
| $Pt/In_2O_3/CeO_2$ | 350 | 0.1 | 3 $h^{-1}$ (WHSV) | ~100 | | <4.5 | 248 |
| $Pt/In_2O_3$ | 300 | 0.1 | 11 $h^{-1}$ (WHSV) | | | 0.6 | 249 |
| $PtNi/CeO_2$ | 400 | 0.1 | 31 $h^{-1}$ (WHSV) | 100 | | ~20 | 207 |
| K-Pt@Silicalite-1 | 400 | 0.1 | 1.0 $h^{-1}$ (WHSV) | 100 | | 1.9 | 212 |
| Pd/ZnO | 250 | 0.1 | 2.03 mL $g_{cat}^{-1}$ $s^{-1}$ (WHSV) | ~67 | | ~15 | 218 |
| 10 wt% Pd/ZnO | 220 | 0.1 | 0.47 $s^{-1}$ (WHSV) | ~58 | | 2 | 216 |
| 15 wt% Pd/ZnO | 250 | 0.1 | 3.4 $h^{-1}$ (WHSV) | ~65 | | 4 | 250 |
| 0.1 wt% $Pd/ZnAl_2O_4$ | 250 | 0.1 | 3.3 $h^{-1}$ (WHSV) | <20 | | 3 | 220 |
| 4 wt% Pd/ZnO (002) | 330 | 0.1 | 30 130 mL $g_{cat}^{-1}$ $h^{-1}$ (GHSV) | 97.3 | | 2.7 | 219 |
| $Fe/Mo_2C$ | 200 | 0.1 | 9000 mL $g_{cat}^{-1}$ $h^{-1}$ (GHSV) | ~8 | | ~4 | 251 |
| $Co/Mo_2C$ | 200 | 0.1 | | ~12 | | ~30 | 251 |
| $Ni/Mo_2C$ | 200 | 0.1 | | ~26 | | ~30 | 251 |
| $Pt/Mo_2C$ | 200 | 0.1 | | 100 | | ~8 | 251 |
| $Cu/Mo_2C$ | 400 | 0.1 | | ~100 | | 8 | 252 |
| 1% $Au/CeO_2$ | 225 | 0.1 | 42 000 $h^{-1}$ (GHSV) | ~50 | | | 253 |
| Au/CuO–$CeO_2$ | 300 | 0.1 | 14.8 $h^{-1}$ (WHSV) | ~79 | | 0.43 | 254 |
| Au–$Cu/CeZrO_x$ | 350 | 0.1 | 21 000 mL $g_{cat}^{-1}$ $h^{-1}$ (GHSV) | 100 | | ~3 | 229 |
| Au/ZnO | ~300 | 0.1 | | 50 | | 20 | 228 |
| $ZnO/ZnZrO_x$ | 380 | 0.1 | 3.3 $h^{-1}$ (WHSV) | 99.7 | | 2.4 | 233 |
| $ZnCeZrO_x$ | 400 | 0.1 | 4.5 $h^{-1}$ (WHSV) | 99.8 | | 6.0 | 234 |
| ZnO | 300 | 0.1 | 0.18 $h^{-1}$ (WHSV) | 3.6 | 99.6 | | 231 |
| ZnO–$Cr_2O_3/CeO_2$–$ZrO_2/Al_2O_3$ | 460 | 0.1 | 22 594 mL $g_{cat}^{-1}$ $h^{-1}$ (GHSV) | ~100 | | ~9 | 232 |
| ZnO–$Al_2O_3$ | 420 | 0.1 | 13 275 mL $g_{cat}^{-1}$ $h^{-1}$ (GHSV) | ~100 | | ~6 | 255 |

activity of commercial $Cu/ZnO/Al_2O_3$ catalyst.[173] The catalyst reduced by $H_2$ first followed by a 10 min reduction under $H_2/H_2O/CH_3OH/N_2$ showed the best activity and stability among various pretreatment conditions. CuO could be reduced to Cu under all activation conditions as confirmed by *in situ* XRD. Moreover, scanning transmission electron microscopy (STEM) results of the catalysts after pretreatment show that activation in $H_2$ only results in discrete ZnO and Cu nanoparticles. In contrast, activation in $H_2/H_2O/CH_3OH/N_2$ mixture induces the formation of thin layers of ZnO covering the Cu nanoparticles due to the strong metal support interaction (Fig. 4). The formation of $ZnO_x$ overlayers outside of the Cu nanoparticle

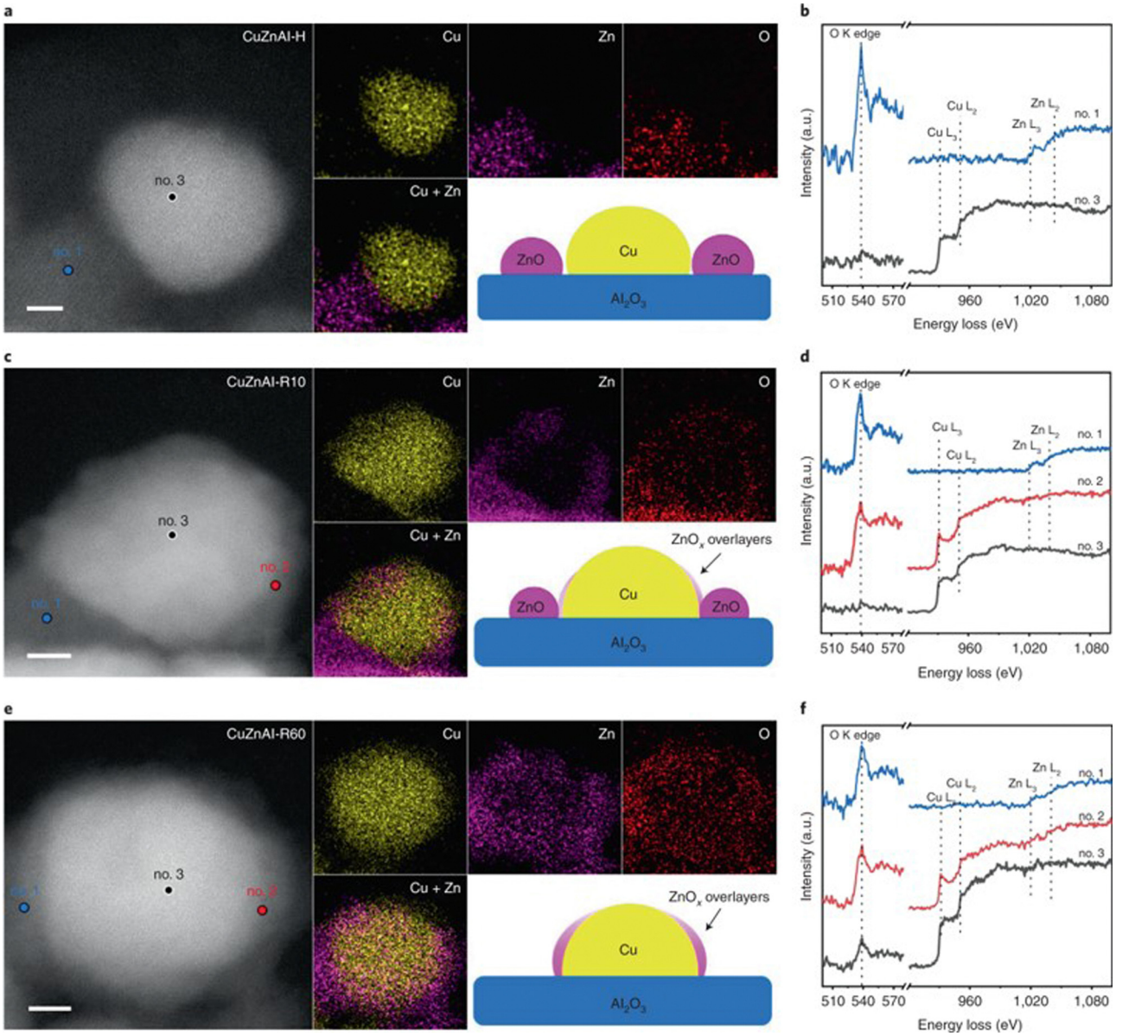


Fig. 4 HAADF-STEM images and corresponding EDS elemental maps of CuZnAl-H (reduced in $H_2/N_2$), (a), CuZnAl-R10 (reduced in $H_2/N_2$) followed by $H_2/H_2O/CH_3OH/N_2$, (c) and CuZnAl-R60 (reduced in $H_2/H_2O/CH_3OH/N_2$), (e). Scale bars, 2 nm. Insets give schematic illustrations of the catalyst structures. EELS spectra of marked regions for CuZnAl-H (b), CuZnAl-R10 (d), and CuZnAl-R60 (f) in (a), (c) and (e), respectively.[173] Reproduced with permission from ref. 173. Copyright (2022) Springer Nature.

after treatment under $H_2/H_2O/CH_3OH/N_2$ was also confirmed by quasi *in situ* XPS and IR spectroscopy using CO as a probe molecule. Therefore, the better catalytic performance is ascribed to the formation of abundant $ZnO_x$–Cu interfacial sites after activation in $H_2/H_2O/CH_3OH/N_2$ mixture for a proper period. DFT calculations of the migration energy of small ZnO clusters over the Cu surface indicate that adsorbed $CH_3OH$ molecules on the ZnO clusters can accelerate the migration of $ZnO_x$ over the Cu nanoparticles, explaining the formation of plenty of Cu–$ZnO_x$ interfacial sites for the catalysts activated under $H_2/H_2O/CH_3OH/N_2$ mixture.

Li *et al.* introduced Mg into $Cu/ZnO/Al_2O_3$ by co-precipitation.[174] The $H_2$ formation rate increases with the increasing Mg content in $Cu/ZnO/Al_2O_3$ up to 5% with the decrease of $CO_2$ selectivity. The highest $H_2$ formation rate was 172 mol $kg_{cat}^{-1}$ $h^{-1}$ at 200 °C. However, a further high Mg content of 7% leads to a slightly low $H_2$ formation rate and high $CO_2$ selectivity. The inverse trend for $H_2$ formation rate and $CO_2$ selectivity can be explained by the increased reverse water–gas shift reaction at high $H_2$ and $CO_2$ concentrations. $Mg^{2+}$ can incorporate into the malachite structure, replace the $Cu^{2+}$ partially and improve the dispersion of Cu and ZnO after calcination. The $Cu^+/Cu^0$ ratio increased with the Mg content up to 5%, indicating that Mg can stabilize the $Cu^+$ and promotes the Cu–ZnO synergy, leading to enhanced performance. Hu *et al.* studied the influence of Pt, Pd, Rh, Au, Ag, Ru,

Ni, and Co on $CuO/ZnO/Al_2O_3$ derived from precursors with hydrotalcite structure in MSR.[175] The catalyst modified with Ru shows the best activity with methanol conversion increase of 20% at 240 °C compared to $CuO/ZnO/Al_2O_3$. At the same time, the introduction of Ru does not have a significant influence on CO selectivity. In contrast, the introduction of Ni and Rh improves the CO formation significantly with a slight drop in methanol conversion. Other metals lead to a decrease in methanol conversion without a significant change in CO selectivity. The promotion effect of Ru is ascribed to the electron interaction between Ru and Cu, as confirmed by XPS. The decrease of activity for other metals is due to the partly destroyed lamellar structure and reduced active surface area after impregnation and calcination.

Zhang *et al.* prepared ZnAl layered double hydroxides (LDHs) on $Al_2O_3$ and used them as support precursors for Cu catalyst.[176] The ZnAl-LDHs were prepared by precipitation of Zn ions in the presence of $Al_2O_3$, and the LDHs were calcinated and transferred into mixed metal oxides before supporting Cu with different loading by impregnation. XRD confirms the formation of the hydrotalcite phase on the support precursor. After calcination, the hydrotalcite phase transfers into metal oxide. The catalyst with 10% Cu loading shows the highest activity with methanol conversion of 99.98% at 300 °C. The high Cu surface area and the easy reduction of Cu due to the interaction with ZnO contributed to the good activity. Gao *et al.* reported that Cu–Al spinel oxide was active in MSR.[177] The Cu–Al spinel catalyst with a high surface area was prepared by the solid-state reaction between $Cu(OH)_2$ and pseudo boehmite. The sintering of Cu during pre-reduction can be avoided by eliminating the pre-reduction step before reaction. During MSR, Cu in the spinel structure was reduced by methanol and released slowly in order to form Cu active sites. The influence of calcination temperature on the activity was systemically studied.[178] The catalyst calcinated at 950 °C shows the best activity, which can be ascribed to the modest release rate of Cu from the spinel structure under reaction conditions and the small copper nanoparticles stabilized by the defective spinel structure. A detailed study of the dynamic change of $CuAl_2O_4$ reveals that the releasing rate of Cu species increases first and then decreases with time on stream, in agreement with the activity at the initial state of reaction.[179] The deactivation after a long time on stream is caused by the coke formation. Even after 300 h on stream, a small amount (5.8%) of Cu species still stays in the spinel lattice. Ni was introduced in the Cu–Al spinel oxide to improve its performance.[180] The catalysts were prepared by the solid phase reaction between $Cu(OH)_2$, nickel acetate, and pseudo-boehmite at 900 °C. $H_2$-TPR profiles indicate that the introduction of Ni slows the reduction behaviour. The catalyst with Ni/Cu of 0.05 exhibits the best activity and good stability. A higher Ni content (Ni/Cu = 0.1 and 0.2) results in an increased CO selectivity, which is related to the formation of metallic Ni from the non-spinel NiO at high Ni loading. However, the $Ni^{2+}$ species in the spinel lattice are stable against reduction under reaction conditions, as proved by the low and stable CO selectivity of the catalyst with low Ni content (Ni/Cu = 0.01 and 0.05). The improvement effect of Ni on Cu–Al spinel oxide catalyst is ascribed to the stabilization effect of Ni containing defective spinel for the small Cu nanoparticles. Hsu *et al.* also studied the performance of $Ni–Cu/Al_2O_4$ in MSR.[181] The catalysts with Cu/Ni ratios of 10 : 1, 5 : 1, 10 : 3 and a fixed Cu/Al ratio of 1 : 10 were prepared by a precipitation–adsorption method.

Characterization results show that the as-synthesis catalysts possess $Ni–Cu/Al_2O_4$ spinel structure. For the catalyst with the highest Ni content, NiCu alloy can also be observed by XRD. The stability test shows only a small amount of coke ($\sim$1.0 wt%) formed on the catalyst after 20 h on stream, which can be removed by calcination in air. However, the selectivity to CO increases after regeneration.

The mechanism of methanol steam reforming on Ni–Cu based catalysts (Ni@Cu(111) and Ni@Cu(110) models) was studied using DFT calculations by Fajín *et al.*[182] The possible reaction routes include methanol decomposition, water–gas shift reaction, direct $CO_2$ production from reforming, and formation of methane. Coke can form from the dissociation of adsorbed species like COH* or from the dehydrogenation of $CH_x^*$ species. According to the results, methanol decomposition followed by the water–gas shift reaction is the main reaction route on the Ni–Cu alloy surface, while $CO_2$ formation from methanol direct reforming is a minor route. The desorption of CO, formation of methane, and coke on the Ni–Cu surface are unfavorable due to the high energy barriers.

*$Cu/ZrO_2$ catalysts.* Penner *et al.* compared the performance of $Cu/ZrO_2$ catalysts prepared with different $ZrO_2$ phases (*m*-$ZrO_2$ and *t*-$ZrO_2$), synthesis methods, and Cu precursors in MSR.[183] Cu/*t*-$ZrO_2$ exhibited a higher activity with higher CO selectivity compared to Cu/*m*-$ZrO_2$. The difference is explained by the more defective and hydroxylated surface of *t*-$ZrO_2$ with plenty of reactive Lewis acidic and Brønsted basic sites. Different binding sites for methanol and water on the surface of *t*-$ZrO_2$ promote the decarbonylation and splitting of C–O bond, leading to the formation of CO and $CH_4$. On Cu/*m*-$ZrO_2$, the CO formation comes from the spillover of formate to the support exclusively, while the Cu–$ZrO_2$ interface sites on Cu/*t*-$ZrO_2$ also contribute to the CO formation. Meanwhile, the Cu precursors used in synthesis show some influence on the activity and product selectivity. The performance of $Cu/ZrO_2$ with different Cu loadings was also studied by Penner *et al.*[184] Cu dispersion decreased from 18% to 0.09% with increasing Cu content from 0.2 wt% to 80 wt%. The Cu morphology was also influenced by the Cu loading, changing from a highly dispersed state at low loading over nanoparticles to bulk Cu grains wetting and covering $ZrO_2$ at 80 wt%, with the change of fraction of exposed $ZrO_2$ simultaneously. It is interesting that the TOF value increases with increasing Cu loading despite the reduced Cu dispersion. Moreover, 80 wt% $Cu/ZrO_2$ showed the highest $H_2$ TOF of $\sim$0.015 $s^{-1}$ at 220 °C. Covering of exposed $ZrO_2$ surface by Cu reduced the exposure of CO generation sites on $ZrO_2$. Mateos-Pedrero *et al.* used $ZrO_2–Al_2O_3$ with different Zr/Al ratios prepared by hydrothermal route as supports for Cu and tested in MSR.[185] The increase of support Zr/Al ratio

up to 1 results in a decrease of CuO crystallite size for the as-prepared catalysts. However, a further increase of Zr/Al ratio higher than 1 leads to an increase in CuO crystallite size as evidenced by XRD. The dispersion of Cu, influenced by the Zr/Al, is revealed by $N_2O$ chemisorption. The catalyst with Zr/Al ratio of 0.4 shows the highest Cu dispersion of 19.7% and the best activity, suggesting the activity is closely related to the dispersion of Cu.

Dal Santo *et al.* investigated the influence of Si on $Cu/ZrO_2$ for MSR.[186] Characterization results show that the introduction of Si results in more amorphous content in the final catalyst and changes the reduction behaviour as well as the final size of Cu species. The $Cu/ZrO_2$–$SiO_2$ with 10 wt% $SiO_2$ content shows the best methanol conversion of 73% and hydrogen productivity of 370 mmol $h^{-1}$ $g_{cat}{}^{-1}$ (with the lowest apparent activation energy of 54.9 kJ $mol^{-1}$), which is higher than $Cu/ZrO_2$ and $Cu/ZrO_2$–$SiO_2$ with other $SiO_2$ contents. The improved activity is ascribed to the Lewis acidity from the electron-deficient small Cu nanoparticles. XPS results clearly demonstrate the introduction of Si results in a lower electron density for Zr and Cu. Mendes *et al.* investigated the influence of the impregnation sequence of Cu and Pd for $CuPd/ZrO_2$ in MSR.[187] The results show that the impregnation sequence has a significant impact on the property and activity of catalysts. Segregated Pd nanoparticles form on the catalyst prepared by impregnating Cu first, while Cu and Pd are well dispersed and homogeneous mixed with the formation of CuPd alloy on the catalyst prepared by adding Pd first. The catalyst with Pd loaded first shows a higher activity, achieving methanol conversion of ~86% with $CO_2$ selectivity of ~95% at 260 °C. Xiao *et al.* used CuZn containing MOFs as precursors for the construction of $CuO/ZnO/CeO_2/ZrO_2$ catalysts for MSR.[188] Typically, Cu/Zn/CuZn-BTC were impregnated with other metal precursors and calcinated in air at 500 °C to form $CuO/ZnO/CeO_2/ZrO_2$ mixed oxides. Then the oxides were mixed with PVA and deposited on the cordierite honeycomb ceramic support to get the final catalyst. The catalyst derived from CuZn-BTC shows better activity than the catalyst derived from Cu-BTC or Zn-BTC. Characterization results show that the addition of $Cu^{2+}$ during the formation of CuZn-BTC MOF introduces lattice distortions and increases the specific surface area. Meanwhile, the ZnO formed during calcination can act as a spacer to prevent the sintering of CuO, resulting in the formation of Cu active sites with fine and uniform dispersion and high activity. The catalyst also shows low CO selectivity, which is related to oxygen vacancies on the $Ce_xZr_{1-x}O_2$.

*Other Cu-based catalysts.* According to thermodynamic calculation, low reaction temperature (100–150 °C) is favorable for MSR while equilibrium shifts to methanol decomposition at high temperature and results in the formation of CO. Therefore, it is important to develop catalysts active at low temperatures. Tsang *et al.* reported that $CuZnGaO_x$ could achieve MSR with a very low CO content (<1 ppm) at 150 °C.[189] The incorporation of $Ga^{3+}$ into Cu/ZnO promotes the reduction of Cu species at lower temperatures, as proved by $H_2$-TPR. Through reduction, small Cu clusters of 0.4–0.8 nm are formed from trapped Cu ions, leading to the high activity at low reaction temperature. Kinetic analysis suggests that the selectivity to CO can be lowered by increasing contact time. Chiu *et al.* studied a series of Cu-containing delafossite materials, including $CuCrO_2$,[190,191] $CuCr_xFe_{1-x}O_2$,[192] $CuFeO_2$–$CeO_2$,[193] and $CuYO_2$[194] in MSR. The promotion effect of $In_2O_3$ on $Cu/SiO_2$ was studied by Santo *et al.*[195] The CO selectivity drops from 0.37% to 0.08% at 260 °C while the $H_2$ formation rate increases from 237 mmol $h^{-1}$ $g_{cat}{}^{-1}$ to 301 mmol $h^{-1}$ $g_{cat}{}^{-1}$ with the addition of 1 wt% In. The stronger reduction peak for Cu–1In/$SiO_2$ than $Cu/SiO_2$ in CO-TPR indicates that In promoted the reduction of Cu. $H_2O$-TPD further reveals that $InO_x$ can promote the activation of water.

Mesoporous silica with ordered structure and carbon nanotubes have also been used for catalysts construction. Jibril *et al.* compared the performance of CuZn/MCM-41 prepared by impregnation and hydrothermal routes.[196] The best activity is achieved by co-impregnation, offering methanol conversion of 88% and CO selectivity of less than 1.8%. Huang *et al.* studied the influence of Ce at Cu/SBA-15 on the catalytic performance.[197] The finely dispersed Ce species show strong interaction with Cu as confirmed by CO-adsorbed FTIR. Reaction results indicate that Cu–Ce/SBA-15 with Ce ion exchange for one time exhibits the best $CO_2$ selectivity and stability. The improved $CO_2$ selectivity is explained by the redox properties of Ce species, which facilitate $H_2O$ activation. Taghizadeh *et al.* studied the performance of Ce–Cu/KIT-6 in MSR.[198] Enhanced activation of water by $CeO_2$ results in methanol conversion of 96.8% and CO selectivity of 3.7% at 325 °C. Zhang *et al.* prepared mesh-type structured $CuFeMg/\gamma\text{-}Al_2O_3$/Al catalysts and used in MSR.[199,200] A commercial Al mesh was used as substrate and $Al_2O_3$ was fabricated by anodic oxidation and calcination. The Cu, Fe, and Mg species were introduced by sequential impregnation. The introduction of Mg decreases the formation of dimethyl ether, while Fe acts as both electronic and structure promoters.[200] The comparison of the two catalysts in the same size range (20–50 mesh) indicates that the commercial granular catalyst shows a better intrinsic activity as its activity at low temperatures is higher. However, when used in the shaped form, the mesh-type catalyst shows better performance than the granular catalyst. This should be ascribed to the better mass transportation for the mesh-type catalyst. Further, the arrangement of mesh-type catalysts in the reactor can influence the activity due to the difference in the effective contact area. The hole-to-edge arrangement can improve the methanol conversion by 14% compared to the hole-to-hole arrangement.

Cu-Based catalysts tend to deactivate due to different reasons such as sintering, change of oxidation states, and coke deposition. The poisons such as sulphur and chloride can also lead to deactivation.[169,201] Valdés-Solís *et al.* concluded that coke formation and sintering lead to the deactivation of $Cu/ZnO/ZrO_2$ and $Cu/MnO_x$.[202] Adding s small amount of oxygen in the feed may be a solution to coke formation and also change the reaction partially to oxidative methanol steam reforming. However, the amount of $H_2$ produced will be reduced. Matsumura *et al.* studied the deactivation of $Cu/ZnO/ZrO_2$ in MSR.[203]

It is found that the growth of Cu nanoparticles is not significant during the reaction. The deactivation is ascribed to the growth of ZnO, which changes the interaction between Cu and ZnO. Hagelin-Weaver *et al.* studied the deactivation of nanoparticle alumina supported Cu/ZnO.[204] XPS shows that the surface Zn/Cu ratio increases after the reaction, indicating that the Cu surface is covered by ZnO due to the migration of ZnO under reaction conditions. It is concluded that the deactivation is related to the reduced Cu surface area due to ZnO cover. No carbon build-up can be observed, indicating that coking is not the deactivation reason for this catalyst. In another work, the deactivation of Cu/ZnO based catalysts is ascribed to the sintering of Cu nanoparticles.[205] Pettersson *et al.* studied the poison effect of sulphur and chlorine on $Cu/ZnO/Al_2O_3$.[169] It is found that sulphur is more detrimental to the catalysts than chlorine. The poison effect of sulphur may be due to the formation of ZnS or $ZnSO_4$ from ZnO and sulphur, while the poison effect of chlorine may occur from the formation of volatile copper chloride compounds. The high reaction temperature is also detrimental due to the sintering. Adding promoters such as $ZrO_2$, $Al_2O_3$, $CeO_2$, and $In_2O_3$ can improve the stability of Cu-based catalysts by modifying the Cu support interaction and inhibiting sintering. Using zeolite may also be a promising method to improve stability by spatial confinement.

**3.1.2 Other transition metal-based catalysts.** Besides Cu catalysts, Ru, Pt, Ni, Au, and Pd based catalysts have also been evaluated in MSR. Different supports such as $Al_2O_3$, $CeO_2$, $Mo_2C$, ZnO, $ZnAl_2O_4$, silicalite-1, and TS-1 are used to construct catalysts. It should be noted that methane forms on some of these catalysts during reaction, which is detrimental to $H_2$ yield and should be inhibited as possible. The preparation methods, promoters, support types, and surface structure of supports show significant impacts on the metal-support interaction and the activity of catalysts, as detailed below.

*Ru, Pt, and Ni based catalysts.* Su *et al.* investigated the MSR on single-site $Me/CeO_2$ catalysts where Me includes Pt, Pd, Rh, and Ru.[206] The catalysts were prepared by an ascorbic acid-assisted reduction method. $Ru_1/CeO_2$ shows the highest methanol conversion and $CO_2$ selectivity compared to other catalysts, which can be explained by the strong adsorption of CO on the $Ru_1/CeO_2$ as confirmed by CO-TPD. It is suggested that MSR is a tandem reaction, consisting of methanol decomposition to CO and the subsequent wafer–gas shift reaction. On the single metal site, the intermediate CO comes from methanol dehydrogenation. CO can either desorb or react with water adsorbed on the neighbouring $Ce^{3+}$ sites to produce $CO_2$. The strong adsorption of CO on Ru site can promote the water–gas shift reaction and the formation of $CO_2$, leading to low CO selectivity. On the $Ru/CeO_2$ surface, the single Ru sites and neighbouring $Ce^{3+}$ sites construct an ensemble reaction pool, catalyzing the methanol decomposition and water–gas shift reaction efficiently (Fig. 5).

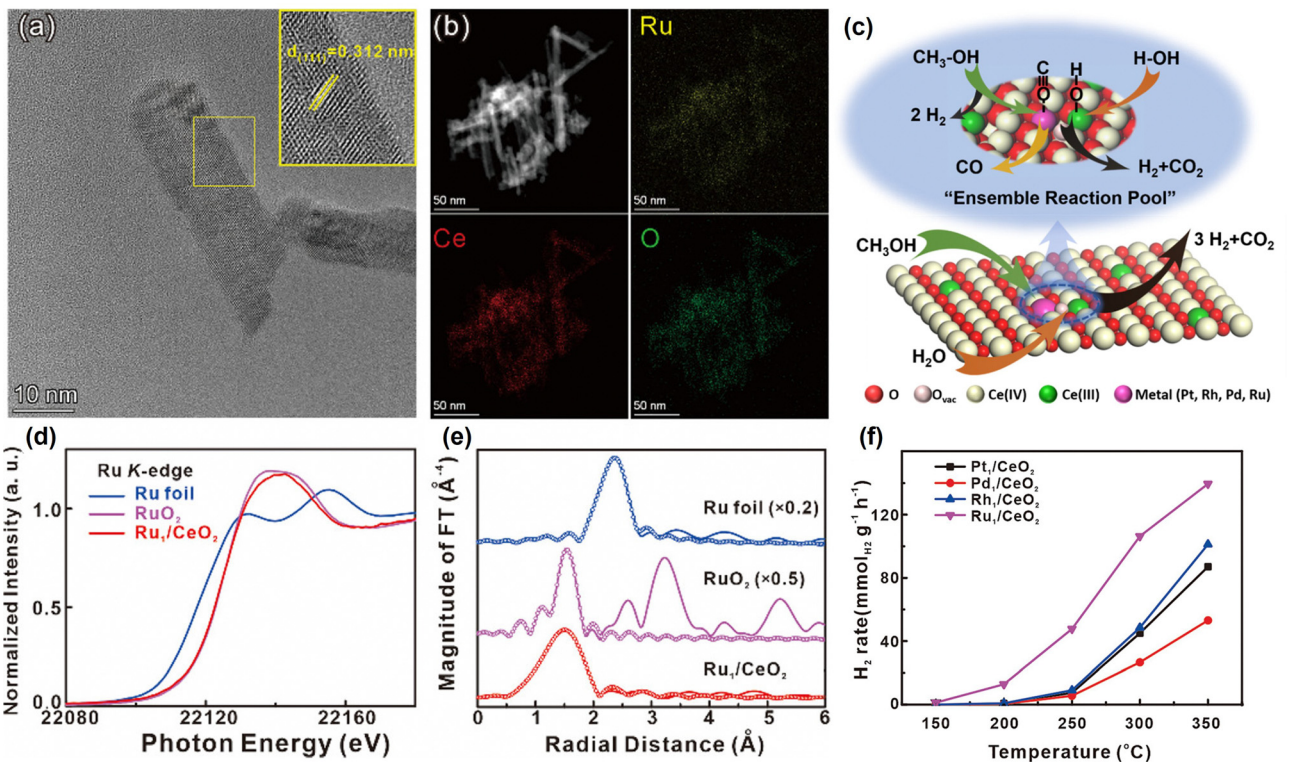


Fig. 5 (a) HRTEM image, (b) HAADF-STEM image, and elemental mapping images of $Ru_1/CeO_2$. (c) Proposed mechanism for methanol steam reforming on $M_1/CeO_2$ single-site catalysts. (d) Normalized Ru K-edge XANES spectra and (e) $k^3$-weighted Fourier transform EXAFS spectra for Ru K-edge of $Ru_1/CeO_2$, $RuO_2$, and Ru foil. (f) $H_2$ formation rate for different catalysts.[206] Modified with permission from ref. 206. Copyright (2021) American Chemical Society.

The performance of $PtNi/CeO_2$ in MSR was studied by Hernández *et al.*[207] $PtNi/CeO_2$ shows higher activity and $H_2$ yield than $Pt/CeO_2$ and $Ni/CeO_2$. Unfortunately, a high methane yield of ~10% and a CO yield of ~10% are achieved with $PtNi/CeO_2$. The CO-adsorbed FTIR indicates that the surface of $PtNi/CeO_2$ is terminated by Pt atoms. Mechanism studies show that methoxy species from methanol adsorption react with the surface oxygen and transform into formate species during the reaction. Ma *et al.* reported that single atom Pt supported on α-MoC enabled MSR at 150–190 °C with a very high average TOF of 18 046 $h^{-1}$ calculated based on Pt.[208] The Pt/α-MoC catalysts were prepared by temperature-programmed carburization of $Pt/MoO_3$ under a flowing mixture of $H_2$ and $CH_4$. The support, α-MoC, shows strong interaction with Pt and facilitates the atomic dispersion of Pt, as proved by STEM and XAS. DFT calculations suggest that Pt/α-MoC provides bifunctional sites for MSR. The electron transfer from Pt to α-MoC makes $Pt_1$ sites electron deficient. Methanol is activated on the Pt site with an energy barrier of 0.67 eV and decomposes to adsorbed CO. Water is adsorbed and activated on α-MoC, forming hydroxy groups, which react with the adsorbed CO to produce $CO_2$ and finish the reforming reaction. The excellent activity is ascribed to the synergy effects between $Pt_1$ sites and α-MoC (Fig. 6).

In a later work, Ma *et al.* reported that atomically dispersed Ni on α-MoC could also catalyze MSR efficiently.[209] A series of Ni catalysts with different Ni loadings were prepared by impregnation under inert gas protection. The best activity is achieved with 2% Ni/α-MoC, which offers an average TOF of 1805 $h^{-1}$ at 240 °C. Although this catalyst shows low CO selectivity of 0.7%, the methane selectivity was very high (~20%). XPS results reveal the charge transfer from Ni to support and the strong electronic interaction between Ni and α-MoC. The local coordination study shows that Ni is anchored on the surface of α-MoC through carbon bridge bonds. The MSR mechanism on this catalyst is studied by DFT calculations and the decomposition of adsorbed methoxy is established as the rate-determining step. The atomically dispersed Ni sites are responsible for the C–H bond activation and CO reforming, while $H_2O$ activation is more easily on the Mo terminated α-MoC site. Therefore, the Ni–C–Mo interfacial sites play an important role in MSR reaction. Sun *et al.* investigated the promotion effect of Zn on the Pt/MoC catalyst.[210] A series of Zn–Pt/MoC with different Zn loadings were prepared by temperature-programmed carburization of mixtures of ammonium molybdate, chloroplatinic acid, and ZnO. Characterization results show that the introduction of a suitable amount of Zn can promote the formation of the $\alpha\text{-}MoC_{1-x}$ phase and improve the dispersion of Pt species through the electronic interaction between Zn and Pt/Mo. The best performance is achieved with Zn–Pt/MoC with Zn content of 0.5%, which shows methanol conversion of 65.9% without the detection of CO at 160 °C. The activity decreases when Zn content is higher than 0.5%, possibly because of the formation of PtZn alloy. The effect of $H_2O/CH_3OH$ ratio on the stability of the catalyst is also studied. High $H_2O/CH_3OH$ ratios will accelerate the deactivation of the catalysts, possibly due to the oxidation of $\alpha\text{-}MoC_x$ by water. Mechanism study suggests that aldehyde is the intermediate for MSR, which can react with adsorbed methoxy species to produce methyl formate and finally decomposes into $CO_2$ and hydrogen through formic acid.

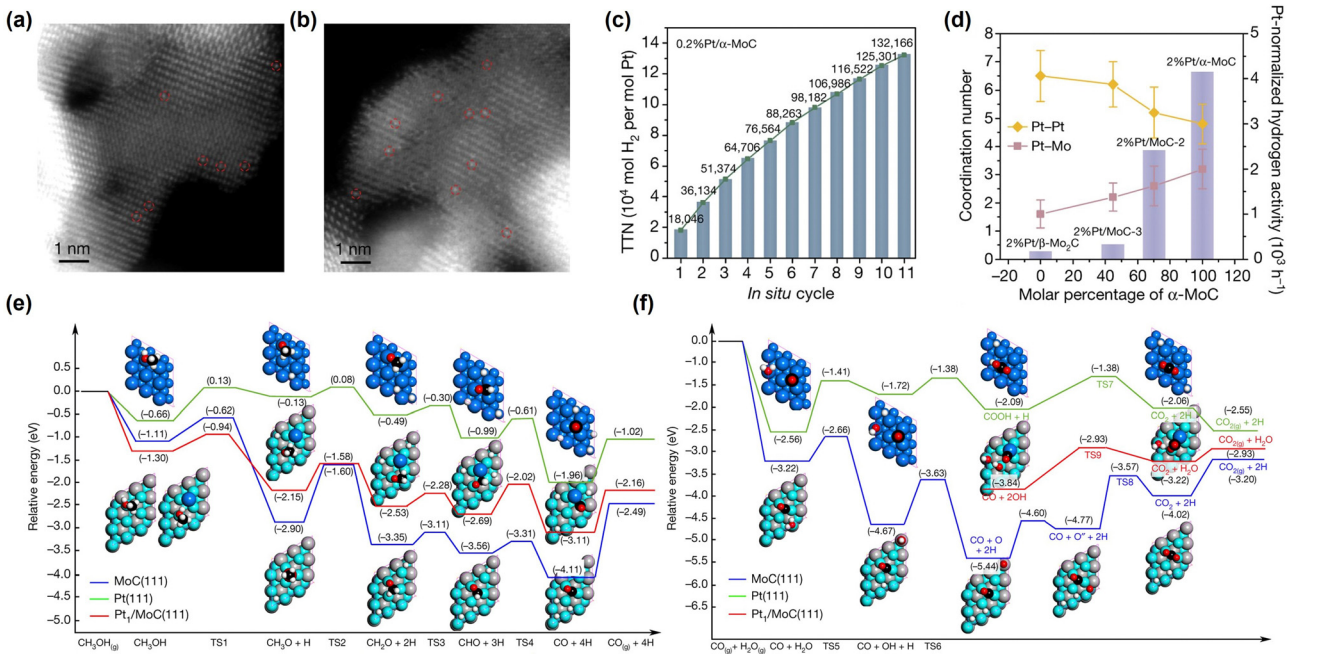


Fig. 6 (a and b) HAADF-STEM images of (a) fresh and (b) used 0.2% Pt/α-MoC. (c) Cycling performance of 0.2% Pt/α-MoC in aqueous-phase methanol reforming. (d) The coordination numbers of Pt–Pt and Pt–Mo shells and the activity change with the change in the molar ratio of α-MoC in Pt/MoC. (e and f) Energy profiles for $CH_3OH$ dissociation and $CO_2$ formation on α-MoC(111), Pt(111), and $Pt_1$/α-MoC(111) surfaces.[208] Modified with permission from ref. 208. Copyright (2017) Springer Nature.

The aldehyde species can also convert into formic acid directly *via* the nucleophilic attack of water (Fig. 7).

Guo *et al.* compared the activity of $Pt/NiAl_2O_4$ and $Pt/\gamma\text{-}Al_2O_3$ for methanol aqueous phase reforming.[211] The $Pt/NiAl_2O_4$ catalyst shows a methanol conversion of 99.9% and a $H_2$ yield of 95.7%, much higher than the $Pt/\gamma\text{-}Al_2O_3$. This catalyst also exhibits good stability with 90% of the original activity being preserved for 600 h on stream. Mechanism study suggests two tandem reactions, namely methanol decomposition and water–gas shift reaction, occur sequentially on the Pt catalyst. For the first reaction, adsorbed methoxy species form and then dehydrogenate to formaldehyde species and finally to absorbed CO step by step. The Pt species on $Pt/NiAl_2O_4$ catalyst under working conditions are closer to the metallic state compared with those on $Pt/\gamma\text{-}Al_2O_3$, thus exhibiting higher activity for methanol decomposition. For the water–gas shift reaction, the IR study suggests that the mechanisms for these two catalysts are different. On $Pt/\gamma\text{-}Al_2O_3$, adsorbed CO converts to $CO_2$ *via* formate intermediate, while a redox pathway happens on $Pt/NiAl_2O_4$. The redox pathway on $Pt/NiAl_2O_4$ is faster than the formate pathway on $Pt/\gamma\text{-}Al_2O_3$, leading to higher water–gas shift activity for the former catalyst. Sun *et al.* investigated the performance of K-promoted Pt/silicalite-1 catalyst in MSR.[212] The Pt species were confined in the silicalite-1 *via* a ligand protection one-pot synthesis route and K was introduced by adding KOH in the synthesis gel. The final Pt content in the catalysts is ~0.3 wt% while the K content varies from 0.1 wt% to 0.8 wt%. The size of Pt nanoparticles is influenced by K loading, possibly due to the Pt–O–$K_x$ interaction. The catalyst with 0.2 wt% K shows the highest Pt dispersion (66.5%) and smallest Pt particle size (1.7 nm), which offers the best activity and lowest CO selectivity. A detailed analysis of the Pt state indicates that $Pt^0$ and $Pt^{\delta+}$ co-exist on the K-modified catalysts. The Pt-0.2 K@S-1 has the highest specific surface area of both $Pt^0$ and $Pt^{\delta+}$, contributing to its high activity. The different roles of $Pt^0$ and $Pt^{\delta+}$ sites are studied by DFT calculations. $Pt^0$ sites are suitable for methanol adsorption and activation, forming HCHO and $HCOOCH_3$. CO is formed more easily on $Pt^0$ sites through the decomposition of HCHO. On the other hand, HCOOH is formed on the $Pt^{\delta+}$ sites from the nucleophilic attack of $HCOOCH_3$ by water, while the decomposition of HCOOH on $Pt^{\delta+}$ sites produces $CO_2$ and $H_2$. The synergy effect between $Pt^0$ and $Pt^{\delta+}$ sites is responsible for the high activity and low CO selectivity. Xiao *et al.* used titanosilicalite-1 supported Pt catalyst in MSR, in comparison with Pt catalysts supported on ZSM-5, $SiO_2$, and $TiO_2$.[213] The Pt nanoparticles on TS-1 show an average diameter of ~2.6 nm, smaller than those on other supports, indicating that TS-1 can stabilize the Pt nanoparticles more efficiently. CO adsorption results show that $Pt^0$ and $Pt^{\delta+}$ coexist on $Pt/SiO_2$ and Pt/ZSM-5 while the major species on Pt/TS-1 and $Pt/TiO_2$ are $Pt^0$, as also confirmed by XPS and XAS, indicating the enhanced electron transferred from Ti containing support to Pt. Reaction results show that the activity of Pt/TS-1 is highest among all these catalysts, offering a $H_2$ formation rate of 6.6 mmol $h^{-1}$ $g_{cat}^{-1}$ at 250 °C. The good activity is ascribed to the small Pt nanoparticle size and the metallic state of Pt. Moreover, this catalyst shows good stability as Pt nanoparticles only sinter slightly to ~2.8 nm after reaction at 300 °C.

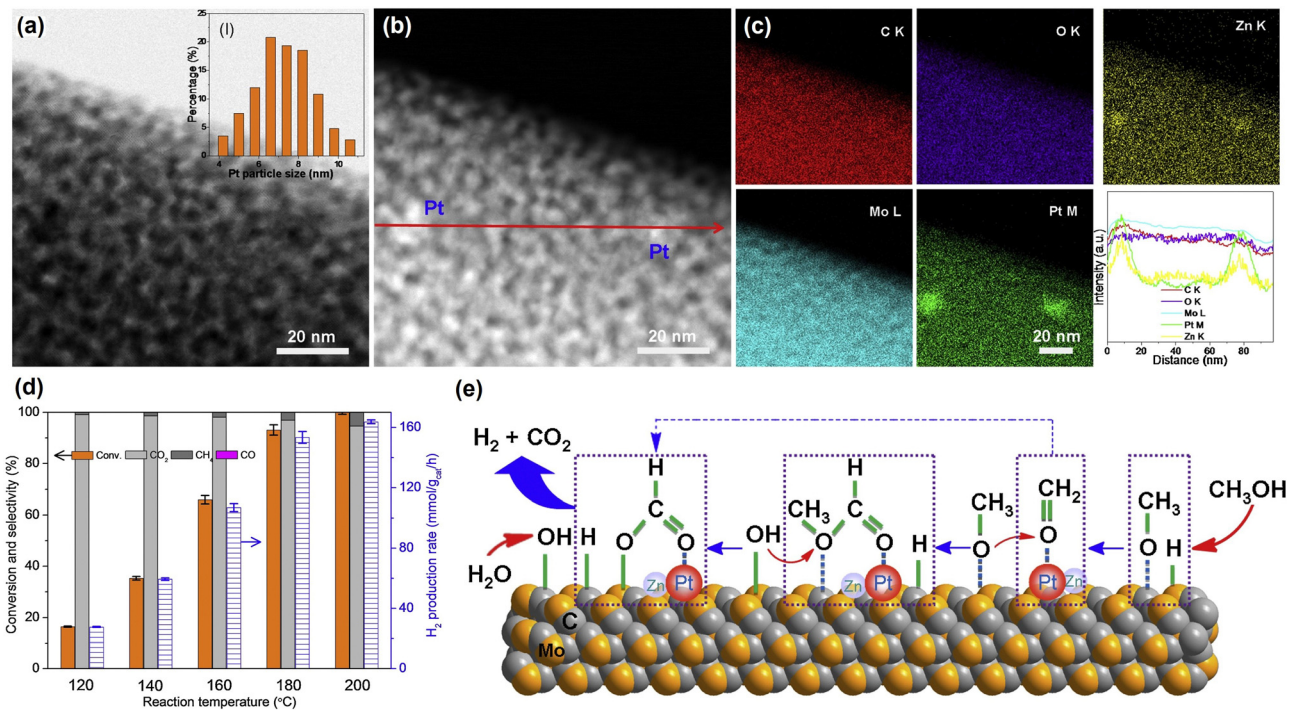


Fig. 7 (a) HRTEM image, (b) HAADF-STEM image, and (c) EDX element mapping and line spectra along the red arrow in (b) of 0.5% Zn–Pt/MoC. (d) Catalytic performance of 0.5% Zn–Pt/MoC for methanol steam reforming at different temperatures. (e) Proposed mechanism for methanol steam reforming on 0.5% Zn–Pt/MoC.[210] Modified with permission from ref. 210. Copyright (2020) Elsevier Inc.

Wasserscheid *et al.* used molten salt to modify the $Pt/Al_2O_3$ catalysts and tested them in MSR.[214,215] Methanol conversion and $CO_2$ selectivity both increase with the addition of promoters. The best loading is determined to be 7.5 wt% and 5.35 wt% for KOH and NaOH, respectively. Phase behaviour study showed that under reaction conditions, a liquid film containing alkali hydroxide/alkali carbonate solution forms on the catalyst surface, which increases the local water concentration and contributes to the improved performance. Besides, the electronic interaction between alkali ions and Pt promotes the intrinsic activity of Pt active sites.

*Pd-Based catalysts.* The most used Pd catalysts are Pd/ZnO. In an early work, Takezawa *et al.* compared the performance of $Pd/SiO_2$, $Pd/ZrO_2$, and Pd/ZnO in MSR.[216] The Pd/ZnO shows higher $CO_2$ selectivity than the other two catalysts. The $CO_2$ selectivity of Pd/ZnO is influenced by the reduction temperature. Characterization results show that PdZn alloy is formed at high reduction temperature and results in the high $CO_2$ selectivity. The morphology of ZnO for Pd/ZnO catalyst has a significant impact on the catalytic activity as reported by Datye *et al.*[217] In a later work, Wang *et al.* studied the effect of ZnO crystallite faceting in detail.[218] The needle-like ZnO predominantly exposed $(10\bar{1}0)$ nonpolar facets were prepared by a PVP-assisted alcohol thermal method and a commercial ZnO prism without preferential exposed facets was used for comparison. Reaction results show that the selectivity to CO decreases with the increase of Pd loading for both supports. This is ascribed to the increased particle size of PdZn at high Pd loadings. Meanwhile, the needle-like ZnO support shows higher CO selectivity compared to ZnO prism, which is explained by the difficulty in the formation of β-PdZn on the nonpolar $(10\bar{1}0)$ surface compared to the (0001) polar facet. On the nonpolar $(10\bar{1}0)$ surface, Pd dominated $Pd_xZn_y$ $(x > y)$ phase and Pd nanoparticles are easily formed and show higher selective to CO. Huang *et al.* also studied the facet effect of ZnO. Typically, Pd nanoparticles with narrow size distribution were deposited on the surface of ZnO with different major exposed facets of (002) or (100).[219] The results demonstrate that the (002) face of ZnO has a stronger interaction with Pd species, which promotes the reduction of Pd species and the formation of PdZn alloy. Thus, the Pd/ZnO (002) catalysts show better MSR activity and $CO_2$ selectivity. The strong interaction also contributes to the stability of formed PdZn alloy against oxidative decomposition under oxidizing atmosphere. Wang *et al.* studied the effect of Pd loading (0.1 to 15 wt%) of $Pd/ZnAl_2O_4$ in MSR.[220] Characterization results show that α-PdZn alloy phase forms on the catalyst with high Pd contents of $\geq$7.5 wt%, while β-PdZn alloy phase forms on the catalysts with low Pd content of $\leq$2.5 wt%. The Pd loading has a significant influence on $CO_2$ selectivity. The catalysts with low Pd loadings show high selectivity to $CO_2$ and the highest $CO_2$ selectivity of 97% is achieved with 0.1 wt% $Pd/ZnAl_2O_4$. When the Pd content increases to 7.5 wt%, the $CO_2$ selectivity drops to $\sim$50.5%. Therefore, the β-PdZn alloy phase is more selective for MSR. It is proposed that the polar face of the $ZnAl_2O_4$ promotes the formation of the β-PdZn alloy at low Pd loadings while the formation of α-PdZn at high Pd loadings is due to the limited Zn atoms on the $ZnAl_2O_4$ surface.

Armbrüster *et al.* prepared $Pd/In_2O_3$ aerogel catalysts by gelation of $InCl_3$ and $PdCl_2$ using propylene oxide in water and ethanol mixture and applied them in MSR.[221] InPd bimetallic nanoparticles are formed after mild reduction at 230 °C, which show a high $H_2$ formation rate of 50 mmol $mmol_{Pd}^{-1}$ $h^{-1}$ and a $CO_2$ selectivity of 99% at 300 °C. The apparent activation energy is 142 kJ $mol^{-1}$ at 225–300 °C and 54 kJ $mol^{-1}$ at 300–400 °C. The high activation energy at low temperatures is similar to the performance of $In_2O_3$ while the low activation energy at high temperatures resembles InPd, indicating the existence of $In_2O_3$ on the catalyst surface at below 300 °C and a dynamic change of surface structure with temperatures. Characterization results show that $In_3Pd_2$ formed from the reduction of $In_2O_3$ and incorporation of In into InPd at temperatures equal to or higher than 300 °C. Isotope-labelling experiments confirm that the reaction involves the Mars–van-Krevelen mechanism, and oxygen atoms in the phase boundary of $In_2O_3$ and PdIn participate in the reaction.

Compared to the Cu-based catalyst, the Pd-based catalysts show better thermal stability. Penner *et al.* studied the thermal stability of PdZn alloy using TEM.[222] PdZn alloy is thermally and structurally stable on reduction between 200 °C and 600 °C from the TEM observation. Iwasa *et al.* compared the stability of Cu/ZnO and $Pd/Zn/CeO_2$ at 350 °C. The $Pd/Zn/CeO_2$ is quite stable and no deactivation was observed for 3 h on stream.[223] In contrast, the Cu/ZnO shows a significant deactivation with activity loss by 20% after 3 h on stream. Datye *et al.* compared the stability of $Pd/ZnO/Al_2O_3$ with commercial $Cu/ZnO/Al_2O_3$.[224] The $Pd/ZnO/Al_2O_3$ is tested at 250 °C, slightly higher than 230 °C for $Cu/ZnO/Al_2O_3$. The Cu-based catalysts show a 40% activity loss after 60 h on stream, while $Pd/ZnO/Al_2O_3$ only shows a 17% loss in activity. The deactivation of Pd-based catalysts is not due to sintering, as the average diameter only increases slightly. A simple oxidation–reduction cycle can regenerate the $Pd/ZnO/Al_2O_3$ and fully recover the activity. Tomishige *et al.* found that zinc carbonate hydroxide forms for the used Pd/ZnO and may be related to the deactiviation.[225] Datye *et al.* proposed that the deactivation of PdZn is caused by coke formation.[226] Pérez-Hernández *et al.* studied the performance of Pd supported on $TiO_2$, $ZrO_2$, and $ZrO_2$–$TiO_2$ mixed oxide and ascribed the deactivation to sintering of active phase and coke deposition.[227]

*Au-Based catalysts.* Wang *et al.* studied the performance of Au/ZnO in methanol steam reforming, decomposition, partial oxidation, and oxidative stream refroming.[228] Au/ZnO with Au content of 4.3 wt% and a mean particle size of $\sim$3.2 nm was prepared by deposition precipitation. The catalytic activity for methanol decomposition and steam reforming is lower than partial oxidation and oxidative steam reforming, as the initiation temperatures are 300 °C, 250 °C, 150 °C, and 150 °C respectively. A comparison with Cu-based catalysts shows that the methanol decomposition and steam reforming activity of Au/ZnO is lower. However, the activity can be greatly enhanced by adding oxygen to the reactant to induce partial oxidation and

oxidative steam reforming. This is ascribed to the good oxygen activation ability of the Au catalyst in the Au-support interface. The oxidative steam reforming shows a good methanol conversion of 95%, high $H_2/CO_2$ yield ratio of 2.4, and low CO selectivity of 1% at 200 °C. Luengnaruemitchai *et al.* tested $Au/Ce_{1-x}Zr_xO_2$ and $Au–Cu/Ce_{1-x}Zr_xO_2$ in MSR.[229] Au and Cu were deposited on the supports by deposition precipitation. The metal loading is influenced by the point of zero charge of the support, which is controlled by the Ce/Zr ratio and preparation method. XRD patterns indicate the formation of AuCu alloy on the $Au–Cu/Ce_{1-x}Zr_xO_2$. The particle size of AuCu alloy is influenced by the deposition pH value. For the $Au/Ce_{1-x}Zr_xO_2$, the catalyst with Ce/Zr of 3 : 1 shows the best activity with methanol conversion of ~95% at 350 °C. For the $Au–Cu/Ce_{0.75}Zr_{0.25}O_2$, the catalyst prepared at pH = 7 exhibits the best performance with 100% methanol conversion at 350 °C.

**3.1.3 Metal oxide based catalysts.** Besides metal-based catalysts, metal oxide catalysts such as ZnO, $In_2O_3$, and $ZnZrO_x$ can catalyze MSR. The thermal stability of metal oxide catalysts is generally good compared to metal-based catalysts while their activity is relatively low. Higher temperatures are necessary to achieve reasonable methanol conversions, which is favourable for CO formation from the thermodynamic point of view.

Penner *et al.* explored the potential of $In_2O_3$ catalysts in MSR.[230] $In_2O_3$ thin films deposited on NaCl(001) surfaces by thermal evaporation and commercial $In_2O_3$ powders were investigated. Pretreatment in $H_2$ or $O_2$ at 400 °C or 450 °C does not show significant impacts on the bulk structure of $In_2O_3$. Temperature-programmed reaction results show that MSR starts at 177 °C and 277 °C on $In_2O_3$ film and powders, respectively. The highest CO selectivity is less than 5% in the temperature range studied (<400 °C), indicating that $In_2O_3$ is very selective for MSR. Later, the performance of ZnO in MSR was studied.[231] Commercial ZnO with a specific surface area of 14 $m^2\ g^{-1}$ was employed. In the batch reactor, ZnO shows activity starting from 267 °C and increases strongly above 327 °C. In the flow reactor, ZnO achieves methanol conversion of 3.6% with high $CO_2$ selectivity of 99.6% at 300 °C. Chen *et al.* applied $ZnO–Cr_2O_3/CeO_2–ZrO_2/Al_2O_3$ prepared by impregnation in MSR.[232] The optimized catalyst achieves methanol conversion of 100% and CO selectivity of ~8% at 460 °C. Reaction results of methanol steam reforming, water–gas shift, and reverse water–gas shift reaction reveal that water–gas shift and reverse water–gas shift reaction can be neglected during MSR on this catalyst. The by-product CO mainly comes from methanol decomposition. The catalyst shows good stability during MSR without significant deactivation for 6 h on stream at 440 °C. However, the activity declines significantly when subjected to methanol decomposition reaction. $H_2$ and CO do not show significant impacts on MSR, but $H_2$ inhibits methanol decomposition. $CO_2$ suppresses MSR, and $H_2O$ suppresses both methanol steam reforming and decomposition. Li *et al.* studied the performance of $ZnO/ZnZrO_x$ in MSR reaction.[233] Reaction results at 400 °C show that methanol conversion increases with Zn content and reaches the maximum of 99% at Zn content of 9–13%. The good performance of catalysts with 9–13% Zn content is ascribed to the synergy effect between small ZnO clusters and $ZnZrO_x$ solid solution support. Moreover, $ZnO/ZnZrO_x$-9% shows good stability during 230 h on stream with a slight decrease of methanol conversion from 90.4% to 80.7% and an almost unchanged CO selectivity of *ca.* 2%. The mechanism of MSR on $ZnO/ZnZrO_x$-9% was studied by temperature-programmed DRIFTS and TPSR. From the FTIR study, methoxy species are observed at 100 °C and transferred to formate species at 300–400 °C. The surface OH species participate in the reaction as the negative bands corresponding to OH species appear at high temperatures. HCHO is detected by TPSR ahead of HCOOH, which comes from methanol dehydrogenation. HCOOH is produced from the reaction of HCHO with OH species and decomposes into $CO_2$ and $H_2$ subsequently. In the later work, the promotion effect of Ce on $ZnZrO_x$ was studied by Li *et al.*[234] Characterization results from XRD and Raman show that Zn and Ce incorporate in the lattice of *t*-$ZrO_2$, forming ternary solid solutions in the composition range studied. $Zn_1Ce_{0.5}Zr_9O_x$ appears to be more active than the $Zn_1Zr_{10}O_x$ and $Zn_1Ce_{10}O_x$, achieving methanol conversion of 99.8% at 400 °C. The CO selectivity of $Zn_1Ce_{0.5}Zr_9O_x$ (6.0%) is lower than $Zn_1Ce_{10}O_x$ (11.6%) but higher than $Zn_1Zr_{10}O_x$ (2.2%). The participation of oxygen vacancy in MSR is confirmed by *in situ* Raman. TPSR profiles indicate that the reaction follows the formate pathway on $Zn_1Ce_{0.5}Zr_9O_x$, similar to that on unmodified $ZnZrO_x$. The enhanced activity is due to the improved $H_2O$ activation ability on oxygen vacancy sites stabilized by $Ce^{3+}$. Ce doping can also stabilize the phase structure of $ZnCeZrO_x$ during the reaction and inhibit carbon deposition, leading to the improved stability.

### 3.2 Homogeneous catalysis for MSR

Homogeneous catalysis refers to a homogeneous phase in which the catalytic reaction system is indistinguishable from the reaction medium and other components. Compared with heterogeneous catalysts, homogeneous catalysts show the characteristics of high activity, high selectivity, and catalyze specific reactions quickly with definite mechanisms. The most used homogeneous catalysts in dehydrogenation reactions are organometallic complexes, such as Ru-based catalysts.[256] Some representative results are summarised in Table 7.

From the perspective of reducing energy consumption and side reactions, lowering the reaction temperature is a key objective for MSR. In 1987, Cole-Hamilton *et al.* reported that MSR could be catalyzed by $[Rh(bipy)_2]Cl$ (bipy = 2,2′-bipyridyl).[257] This catalyst achieved a TOF of 7 $h^{-1}$ at 120 °C in the presence of NaOH. Beller *et al.* reported a process facilitated by Ru pincer complexes $[RuHCl(CO)(HN(C_2H_4PiPr_2)_2)]$, offering a TOF of 4700 $h^{-1}$ and a turnover number (TON) of 35 000 at reaction temperature of 93 °C.[258] The reaction mechanism was studied in the later work, as shown in Fig. 8. Ru–Amido complex is sorted and considered as the key reaction intermediate. This intermediate is highly reactive with methanol, formic acid, and water, providing mono and dihydride Ru complexes, which can be deprotonated at the nitrogen atom of the pincer ligand in the presence of base. The deprotonated dihydride complex releases hydrogen and formaldehyde during

Table 7 Homogeneous catalysts for methanol dehydrogenation

| Catalyst | Temp. (°C) | Yield (%) | TON | Ref. |
|---|---|---|---|---|
| 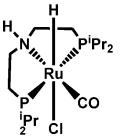 | 93 | 59 | 350 000 | 258 |
| 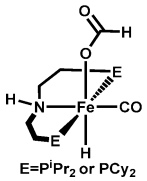 | ~80 | 50 | 51 000 | 267 |
| 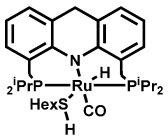 | 150 | 96 | >130 000 | 269 |
| 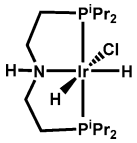 | 94 | | 1400 | 270 |
| 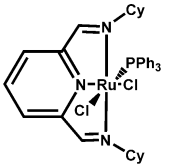 | 100 | 90 | | 271 |
| 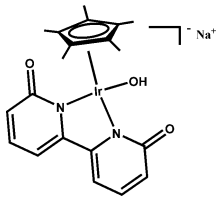 | ~90 | 64 | 10 510 | 263 |
| 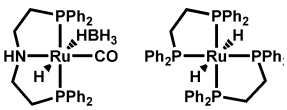 | 94 | 26 | >4200 | 259 |
| 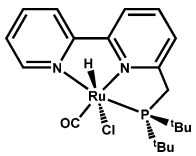 | ~100 | 82 | 29 000 | 261 |
| 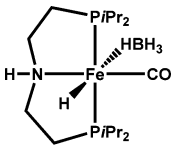 | 91 | | 9834 | 265 |
| 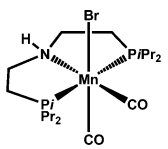 | 92 | | >20 000 | 266 |

the protonation to generate monohydride complex. Beller *et al.* also reported a bi-catalytic system for methanol steam reforming in the absence of base.[259] This system contains Ru-MACHO-BH and $Ru(H)_2(dppe)_2$ that work synergistically. A TON of higher than 4200 was achieved at ~94 °C and only a trace amount of CO (<8 ppm) was detected in the products. Grützmacher *et al.* developed a Ru-bases complex with a chelating bis(olefin) diazadiene ligand.[260] The complex, $[K(dme)_2][Ru(H)(trop_2dad)]$, can intramolecularly store up two equivalents of hydrogen reversibly. This catalyst can achieve 80% conversion after 10 h at the temperature of 90 °C, producing $CO_2/H_2$ from methanol aqueous solution under neutral conditions. Milstein *et al.* reported a Ru-PNN pincer complex in this reaction.[261] This catalyst achieves a $H_2$ yield of up to 82% in 9 days at ~100 °C and is very stable. No deactivation can be observed after ~1 month, achieving a TON of ~29 000. Reek *et al.* reported a ruthenium complex Ru(salbinapht)(CO)(Pi-$Pr_3$) could also catalyze this reaction.[262] A TOF of 55 $h^{-1}$ is achieved at 82 °C.

Yamaguchi *et al.* reported that an anionic Ir complex with a functional bipyridonate ligand was active for MSR.[263] A continuous $H_2$ production is achieved for 150 h by adding methanol, water, and NaOH continuously at refluxing conditions, achieving a TON of 10 510 with a $H_2$ yield of 64%. Beller *et al.* reported a Ir-PNP pincer complex in this reaction.[264] A TOF of 326 is achieved at 70 °C. During the reaction, the formation of an iridium dihydride carbonyl complex results in the deactivation of this catalyst in low basic media. Using strongly basic conditions can inhibit the deactivation.

It is worth noting that non-noble metal-based complex catalysts for MSR have been explored in recent years. Beller *et al.* reposted an iron pincer complex with a TON close to 10 000 obtained with a TOF of 644 $h^{-1}$ at 91 °C.[265] Deactivation is observed for this catalyst and adding additional ligands in the reaction mixture can improve the lifetime as the decomposition of the catalyst is hindered. Later, a Mn pincer catalyst was reported for this reaction.[266] This catalyst shows good stability and a TON of more than 20 000 is reached. However, the PNPiPr ligand is sensitive to light and the experiments need to be carried out under the exclusion of light. Holthausen *et al.* applied a pincer-supported Fe compound in the methanol dehydrogenation reaction with TON up to 51 000.[267] A co-catalytic amount of a Lewis acid, $LiBF_4$, plays an important role in facilitating the decarboxylation of the Fe formate species.

### 3.3 Heterogeneous catalysis for methanol synthesis from $CO_2$ hydrogenation

Methanol can be produced from CO hydrogenation and $CO_2$ hydrogenation. Methanol synthesis from syngas in the presence of a small amount of $CO_2$ is a well-established industry process while direct $CO_2$ hydrogenation has been a hot research topic in recent years. A brief introduction of heterogeneous catalysts for $CO_2$ hydrogenation to methanol will be given below.

Cu/ZnO based catalysts show good performance in both methanol synthesis from CO and $CO_2$.[272,273] Urakawa *et al.* studied the performance of $Cu/ZnO/Al_2O_3$ in $CO_2$ hydrogenation under very high pressure.[274] The one-pass $CO_2$ conversion can achieve 95% with a methanol selectivity of 98% at 36 MPa and 260 °C. Other Cu-based catalysts such as $Cu/ZrO_2$ and $Cu/CeO_2$ also show good performance for $CO_2$ hydrogenation to

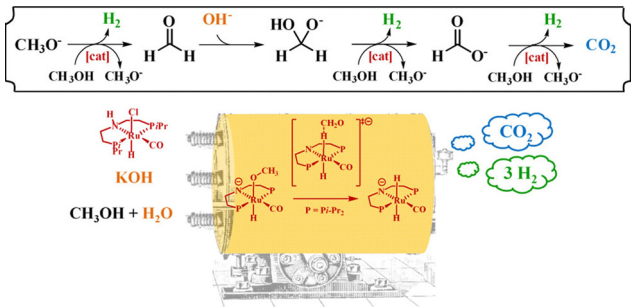


Fig. 8 The mechanism of RuHCl(CO)(HN($C_2H_4PiPr_2$)$_2$) catalyzed methanol dehydrogenation.[268] Reproduced with permission from ref. 268. Copyright (2016) American Chemical Society.

methanol. Rodriguez *et al.* compared the performance of $CeO_x$/Cu(111) and Cu(111) using model catalysts.[275] The TOF of $CeO_x$/Cu(111) is 1.3 $s^{-1}$ at 302 °C, much higher than Cu(111) ($6.3 \times 10^{-3}$ $s^{-1}$). The activation energy of $CeO_x$/Cu(111) (12 kcal $mol^{-1}$) is also lower than Cu(111) (25 kcal $mol^{-1}$). Satokawa *et al.* compared the performance of Cu supported on $ZrO_2$ with different crystal structures, including amorphous $ZrO_2$ (a-$ZrO_2$), monoclinic $ZrO_2$ (*m*-$ZrO_2$), and amorphous/tetragonal $ZrO_2$ supported on KIT-6 (a-$ZrO_2$/KIT-6 and *t*-$ZrO_2$/KIT-6).[276] Reaction results show that the catalysts using supports including amorphous $ZrO_2$ show higher methanol selectivity and formation rate. The difference is related to the different existence states of Cu species on the as-prepared catalysts. XRD and XAS show that CuO exists on the Cu/*m*-$ZrO_2$ and Cu/*t*-$ZrO_2$/KIT-6 while $Cu_xZr_yO_z$ exists on the a-$ZrO_2$ containing catalyst. After reduction, the Cu size of a-$ZrO_2$ containing catalyst is smaller, leading to the higher activity. At the same time, methanol vapor adsorption indicates that the adsorption of methanol on a-$ZrO_2$ is weaker. The weak adsorption of methanol can inhibit the decomposition of methanol into CO and improve the methanol selectivity. Recently, Li *et al.* reported a faujasite-encaged mononuclear Cu catalyst (Cu@FAU) that showed good performance in $CO_2$ hydrogenation to methanol.[277] A methanol formation rate of 12.8 mmol $g_{cat}^{-1}$ $h^{-1}$ and methanol selectivity of 89.5% can be achieved at 240 °C. No deactivation is observed over 200 h on stream, showing that this catalyst is very stable under reaction conditions and may be a promising catalyst for large-scale industry applications. $H_2$–$D_2$ exchange experiment results show that the activation of $H_2$ on this catalyst is assisted by $CO_2$. Surface species study and DFT calculations prove that $CO_2$ hydrogenation to methanol follows the formate pathway. The mononuclear Cu and neighbouring O sites act as classical Lewis pairs and activates the $H_2$ with the assistance from adsorbed $CO_2$ species.

Pd-Based catalyst is another kind of catalyst used for $CO_2$ hydrogenation to methanol. Different supports, such as ZnO, $Ga_2O_3$, and CNTs, have been used. For Pd/ZnO, the PdZn alloy formed after reduction is ascribed to the active sites.[278] Mu *et al.* studied the influence of Al doping in ZnO support for Pd/ZnO on this reaction.[279] The activity increases with Al doping up to 3.93 wt%. Al doping in ZnO can facilitate the adsorption and activation of $CO_2$, leading to the improved performance. However, Al content greater than 3.93 wt% leads to a decrease in activity. This is caused by the formation of $ZnAl_2O_4$ spinel and amorphous $Al_2O_3$ on the ZnO surface. Tsang *et al.* studied the influence of the exposed surface of $Ga_2O_3$ for Pd/$Ga_2O_3$.[280,281] β-$Ga_2O_3$ with plate and rod morphologies are used as supports. The plate type Pd/β-$Ga_2O_3$ shows better performance than the rod type catalyst. XRD and TEM show that the major exposed facets are different for rod and plate β-$Ga_2O_3$. The majority surface of rod $Ga_2O_3$ is terminated with (111) and (110) faces while it is (002) for plate $Ga_2O_3$. The (002) surface of $Ga_2O_3$ has polarity due to the unbalanced arrangement of cation and anion and a stronger interaction with Pd, which improve the metal dispersion and lead to the formation of $PdGa_x$, resulting in a better activity. Li *et al.* investigated the position effect of Pd on CNTs.[282] Pd nanoparticles with high selectivity located inside or outside CNTs were prepared and tested in $CO_2$ hydrogenation to methanol. The TOF of Pd inside of CNTs is 0.33 $h^{-1}$, much higher than the Pd outside of CNTs (0.09 $h^{-1}$). The activation energy of Pd inside of CNTs is also lower. The difference is caused by the different ratios of $Pd^{\delta+}$ species. The deviation from the plane structure of CNTs causes the hybridization of the p orbital of C to become intermediate between $sp^2$ and $sp^3$. Therefore, the π-electron density is shifted from the concave inner surface to the convex outer surface of CNTs. The inner surface thus becomes electron deficient and helps to stabilize the $Pd^{\delta+}$ species, forming more $Pd^0$–$Pd^{\delta+}$ structures. During $CO_2$ hydrogenation, $H_2$ is activated on $Pd^0$ sites while $CO_2$ is activated on $Pd^{\delta}$+. More $Pd^0$–$Pd^{\delta+}$ structures lead to the higher activity.

Besides metal-based catalysts, metal oxides and metal sulfides catalysts have also been used in $CO_2$ hydrogenation, such as $In_2O_3$, $In_2O_3$/$ZrO_2$, ZnO–$ZrO_2$, $GaZrO_x$, $CdZrO_x$, and $MoS_2$. Metal oxide-based catalysts show high methanol selectivity than Cu-based catalysts. However, the activity at low temperatures is unsatisfactory and should be improved. Using DFT calculations, Liu *et al.* predicted that $In_2O_3$ could catalyze $CO_2$ hydrogenation to methanol.[283,284] Later, the activity of commercial $In_2O_3$ is confirmed by experiments.[285] Pérez-Ramírez *et al.* reported a very high selectivity to methanol catalyzed by $In_2O_3$ prepared from the decomposition of $In(OH)_3$.[286] The oxygen vacancies on the surface of $In_2O_3$ are crucial in this reaction. The easy reduction of $In_2O_3$ under reducing atmosphere at high temperature limit its practical application. The activity of $In_2O_3$ can be improved by supporting on monoclinic $ZrO_2$.[287] The lattice mismatch between $ZrO_2$ and $In_2O_3$ causes pronounced tensile forces and more oxygen vacancies for $In_2O_3$. $ZrO_2$ also contributes to $CO_2$ activation. Both these factors contribute to the improved In-based specific activity. Metals, including Pd,[288] Pt,[289] Ni,[290] Rh,[291] Re,[292] and Au,[293] have been used as promoters for $In_2O_3$, mainly to improve the hydrogen activation ability of the catalyst at low reaction temperatures. Li *et al.* studied the performance of ZnO–$ZrO_2$ solid solution catalyst in $CO_2$ hydrogenation to methanol.[294] This catalyst shows a high methanol selectivity of 86–91% with $CO_2$ conversion higher than 10% at 320–315 °C. The resistance of ZnO–$ZrO_2$ to $SO_2$ and $H_2S$ is good. No deactivation is observed in the presence of 50 ppm $SO_2$ or $H_2S$, making this

catalyst suitable for industrial application. DFT calculations show that the synergetic effect between Zn and Zr sites leads to the good performance. Later, the solid solution catalyst system is extended to $GaZrO_x$ and $CdZrO_x$.[295] Wang *et al.* reported that $MoS_2$ nanosheet could catalyze $CO_2$ hydrogenation to methanol at low temperatures.[296] A methanol selectivity of 94.3% with a $CO_2$ conversion of 12.5% is achieved at 180 °C. Theoretical study shows that the in-plane S vacancies of $MoS_2$ are the active sites for methanol formation.

It should be noted that this part is only a brief introduction for $CO_2$ hydrogenation to methanol. A comprehensive summary on this topic can be found in some nice review articles.[297,298]

# 4. Ammonia and related chemicals

Ammonia and its derivatives, including ammonia borane and hydrazine hydrate, also deserve attention as carbon-free energy carriers.[299] Ammonia, a well-established industrial product, is produced and transported globally at a scale of approximately 150 million tons per year *via* trains, pipelines, and other means.[300] In contrast to carbon-containing carriers, ammonia does not emit CO or $CO_2$, and ammonia is not a greenhouse gas. In 1982, Green first proposed the use of ammonia as an energy carrier, suggesting that it could be an economically viable energy vector.[301] Other ammonia-based compounds like ammonia borane and hydrazine are also carbon-free. Ammonia is a particularly versatile energy carrier because the hydrogen generated from ammonia can be utilized in hydrogen fuel cells, and meanwhile, ammonia itself and related compounds can be directly employed as fuels.[302]

## 4.1 Ammonia

Ammonia ($NH_3$) offers great potential as a liquid-phase hydrogen storage and transport medium due to its ability to be stored in liquid form under relatively mild conditions. Notably, its mass hydrogen density surpasses that of liquid $H_2$, and $NH_3$ is much easier to liquefy than $H_2$, given its higher temperature ($\sim$25 °C) and lower pressure ($\sim$3 bar) requirements. $NH_3$ has several advantages as a hydrogen source, as summarized below.

High hydrogen capacity: with a hydrogen storage capacity of up to 17.7 wt% (108 g $L^{-1}$) and an energy density of 3000 W h $kg^{-1}$, $NH_3$ outperforms other LHCs such as methanol in terms of capacity and density.[302]

Environment-friendly: $NH_3$ decomposition results in the production of $H_2$ and stoichiometric $N_2$ without generating harmful CO or greenhouse gas $CO_2$,[303] thereby benefiting both the environment and the purity of $H_2$ produced.[302]

Since the synthesis of $NH_3$ from $N_2$ and $H_2$ ($H_2$ storage process) is very mature in industry, using $NH_3$ as LHC is mainly decided by $H_2$ release process. There are two key challenges of $NH_3$ decomposition and $H_2$ separation, which will be discussed in the following sections.

**4.1.1 Ammonia decomposition.** Metal catalysts have played critical roles in $NH_3$ decomposition reactions since Green's first report in 1982.[301] At high temperatures, $NH_3$ adsorbs onto active catalytic sites and undergoes N–H bond cleavage. The pathway for $NH_3$ decomposition has been proposed as follows, where * represents the active site for $NH_3$ decomposition.[304]

$$NH_3(g) + * \rightarrow NH_3^*$$

$$NH_3^* + * \rightarrow NH_2^* + H^*$$

$$NH_2^* + * \rightarrow NH^* + H^*$$

$$NH^* + * \rightarrow N^* + H^*$$

$$2N^* \rightarrow N_2(g)$$

$$2H^* \rightarrow H_2(g)$$

The binding strength of the metal site to N is the most dominant factor throughout the reaction. A strong M–H bond favours N–H bond scission but goes against N* desorption, while a weak M–H bond is not sufficient to cause N and H separation. Thus, a suitable strength of M–H bond is crucial for enhancing catalytic activity for $NH_3$ decomposition.[305] Among all single metal catalysts, Ru exhibits the highest catalytic activity due to their appropriate Ru–N binding energy.[306] Currently, catalysts for $NH_3$ decomposition can be divided into two categories, namely Ru-based catalysts and Ru-free catalysts (Table 8).

In recent years, significant advancements have been made in the synthesis and mechanism of ruthenium-based catalysts, aiming to achieve higher activity at lower temperatures.[305,307] Yamazaki *et al.* prepared $Ru/CeO_2$–$PrO_x$ *via* a coprecipitation route for on-site $NH_3$-decomposition $H_2$ fuelling station in 2022, which showed the highest level of decomposition activity among all catalysts ever reported.[308] Typically, the optimized catalyst Ru/CP33 shows $NH_3$ conversion of >99.5% at 500 °C within 1800 h on stream. The benefits of $H_2$ production from $NH_3$ decomposition exceed the actual cost, which lays a solid foundation for its commercialization. Zhong *et al.* prepared a series of alkali metal silicates $A_2SiO_3$ (A = Li, Na, and K) supported Ru nanoparticles for $NH_3$ decomposition, and the optimized catalyst exhibited the highest conversion of 60.5% with a TOF value of 2.03 $s^{-1}$.[309] The improved catalytic performance is ascribed to strong electronic metal support interaction (SMSI) between Ru particles and oxygen vacancies. Yun *et al.* confirmed that modulating the SMSI could efficiently enhance the catalytic properties of Ru/BCY-*x* catalysts, which provided an efficient way for catalyst modification.[310] Chae *et al.* prepared a series of Ru doped $La_xCe_{1-x}O_y$ composites for $NH_3$ catalytic decomposition and confirmed that $N_2$ desorption was the rate-determining step in the reaction[311] To reduce costs, non-noble metal-based catalysts for $NH_3$ decomposition have been explored. Various strategies have been employed to improve the catalytic activity, such as designing spatially confined metal nitrides, using one-pot cation–anion double hydrolysis synthesis route, and employing a sol–gel method with a

second support material. Jia *et al.* designed spatially confined metal nitrides in order to weaken the associative desorption of adsorbed N effectively.[312] The synthesized $Mo_2N$/SBA-15/rGO exhibits the highest $NH_3$ decomposition rate of 30.58 mmol $g^{-1}$ $min^{-1}$ among all Mo-based catalysts ever reported. Chae *et al.* prepared a series of $Ni/Al_1Ce_aO_x$ composites with higher Ni dispersion and surface area *via* one-pot cation–anion double hydrolysis synthesis.[313] The introduction of Ce can modulate the synergy of oxygen vacancies, NiO reducibility, Ni-support interaction, and basicity. Jiang *et al.* developed a $CeO_2$ and BN hybrid-supported Ni catalyst by a sol–gel method, which showed high activity with $H_2$ yield of approximately 516 mmol $g_{Ni}^{-1}$ $min^{-1}$ at 600 °C.[314] The result demonstrates a simple but effective strategy of adding a second support material to improve catalytic activity for $NH_3$ decomposition. Besides, Bertola *et al.* performed kinetic assessment of $NH_3$ decomposition reaction based on experiments and computational fluid dynamics modeling.[315] A flat-plate microreactor operating under kinetic-control conditions with negligible mass transfer resistance is designed, which facilitates the assemblage and disassemblage of components.

**4.1.2 Gases separation.** Effective $H_2$ separation is another critical challenge in the gas-phase decomposition of $NH_3$. Generally, the reaction mixture includes products $N_2$, $H_2$, and undecomposed $NH_3$. Small concentrations of $NH_3$ gas can be captured by passing through liquids or solid-packed beds.[300,323] Pressure swing adsorption (PSA) is one of the most well-developed strategies for commercial $NH_3/N_2/H_2$ separation.[300] PSA, first reported in 1959 by Charles W. Skarstrom,[324] is a process where the feed gases are passed through a selectively absorbent material bed at high pressure,[325,326] and the system pressure is reversed to backflush the unwanted compounds. At present, PSA has been able to apply in industrial production on a large scale and has achieved a great economic effect. Alternatively, $H_2$ permeable membranes have been recently applied in the separation of $NH_3/N_2/H_2$. There are three types of $H_2$ permeable membranes: porous ceramic, polymeric, and metal (porous and solid).[327] This method is characterized by a low energy consumption rate, long-term durability, and good quality control and has been used in industry.

Table 8 Catalysts for $NH_3$ decomposition

| Catalyst | Temp. (°C) | GHSV (mL $g_{cat}^{-1}$ $h^{-1}$) | Conv. (%) | $H_2$ production (mmol $g^{-1}$ $min^{-1}$) | Ref. |
|---|---|---|---|---|---|
| Ru/CP33 | 500 | 30 000 | 99.5 | 33.3 | 308 |
| $Ru/K_2SiO_3$ | 450 | 30 000 | 60.5 | 20.3 | 309 |
| Ru/CNTs | 550 | 30 000 | 100 | 33.5 | 316 |
| $Ru/Cr_2O_3$ | 600 | 30 000 | 100 | 30.7 | 317 |
| Ru-K/CaO | 400 | 9000 | 53.7 | 5.4 | 318 |
| $Ru/CaAlO_x$ | 500 | 6000 | 98.2 | 6.6 | 319 |
| $Mo_2N$/SBA-15/rGO | 600 | 60 000 | 68.5 | 184.6 | 312 |
| 20Ni/$Al_1Ce_{0.05}O_x$ | 600 | 54 000 | 81.8 | 49.3 | 313 |
| $Ni_{7.5}Co_{2.5}/CeO_2$ | 650 | 30 000 | 96.96 | 32.5 | 320 |
| $20Co\text{-}10Ni/Y_2O_3$ | 550 | 9000 | 85.02 | 8.5 | 321 |
| $Ni_{10}Ce_5O_x/Al_2O_3$ | 525 | 30 000 | 75 | 25.1 | 322 |

### 4.2 Ammonia borane

Ammonia borane (AB), a solid at room temperature, has emerged as one of the most promising materials for chemical hydrogen storage since its first synthesis in 1955 by Shore and Parry.[328] Due to its high hydrogen content of 19.6 wt%, non-toxic nature, and sustainable stability under ambient conditions, AB has garnered significant interest as a potential hydrogen carrier. The structure and properties of AB can be found in a recent review paper by Demirci.[329] AB dissolves well in water and methanol, allowing it to decompose and release $H_2$ in the presence of catalysts in the liquid system. The chemical equations for AB hydrolysis and methanolysis are as follows.

$$\text{Hydrolysis: } NH_3BH_3 + 2H_2O \rightarrow NH_4BO_2 + 3H_2$$

$$\text{Methanolysis: } NH_3BH_3 + 4CH_3OH \rightarrow NH_4B(OCH_3)_4 + 3H_2$$

However, at high temperatures, AB decomposes to produce $H_2$ and volatile toxic substances such as $NH_3$ and diborane.[330,331]

**4.2.1 Hydrolysis of ammonia borane.** In contrast to energy-intensive and environmentally harmful pyrolysis, AB hydrolysis does not release gaseous by-products, making it safer and more suitable for applications in the automotive industry and other fields. In 2005, Xu *et al.* reported the first hydrolysis reaction of AB using Pt, Rh, and Pd nanoparticles as catalysts, which opened the prelude of AB hydrolysis.[332] During hydrolysis, H connected to B in AB combines with H in the $H_2O$ molecule to release $H_2$ in the presence of catalysts. The mechanism of AB hydrolysis is in the process of continuous development. Zhou *et al.* applied isotopic experiments to determine the order of B–H, B–N, and O–H bond cleavages, confirming that $NH_3BH_2^* + H_2O^* \rightarrow NH_3BH_2(OH)^* + H^*$ is the rate-determining step.[333] The results suggest that the key to hydrolysis catalysis lies in O–H breaking in $H_2O$. Some of the representative catalysts for AB hydrolysis are listed in Table 9.

Similar to the dehydrogenation reaction of toluene and NEC, noble metal catalysts used in the hydrolysis of AB have better performance than non-noble metal catalysts. In 2022, Liu *et al.* immobilized Ru nanoparticles on natural chitosan polymers, achieving a TOF value of 331.8 $min^{-1}$ and an $E_a$ value of 41.3 kJ $mol^{-1}$.[334] Xu *et al.* first applied metal–organic frameworks in hydrolysis with the help of Pt nanoparticles in MIL-101's nanopores, which showed an activation energy of

Table 9 Representative catalysts for ammonia borane hydrolysis

| Catalyst | Temp. (°C) | TOF ($min^{-1}$) | $E_a$ (kJ $mol^{-1}$) | Ref. |
|---|---|---|---|---|
| Ru/CS | 30 | 331.8 | 41.3 | 334 |
| N-hcp-Ni/C | 25 | 17.2 | 35.3 | 337 |
| PVP stabilized Co | 40 | 14 | 46 | 336 |
| Co/CTF | 25 | 42.3 | 42.7 | 338 |
| Fe–Ni–$Ni_3B$ | 30 | ~293 | 39.95 | 339 |
| P2-Cu–$Co_3O_4$@CNF | 30 | 35.6 | 29.86 | 340 |
| hcp-CuNi/C | 25 | 22.64 | 29.92 | 351 |
| Co–P | 25 | 23.5 | 38.7 | 352 |
| Cu@$Ni_6$-MOF | 25 | 69.1 | 31.6 | 341 |
| PdCo@NCHP | 30 | 881.91 | 36.9 | 353 |
| Pt/$MoO_{3-x}$-500 | 25 | 331.4 | 13.97 | 354 |

40.7 kJ $mol^{-1}$.[335] The present results bring light to new opportunities in the superiority of porous materials in hydrolysis.

Despite their superior performance, the high cost of noble metal catalysts has driven researchers to explore more affordable non-noble metal catalysts, such as Ni and Co catalysts. Özkar *et al.* prepared polymer-stabilized cobalt(0) nanoclusters from the reduction of cobalt(II) chloride, which was found to be active in the hydrolysis reaction of AB.[336] Li *et al.* presented for the first time that N-hcp-Ni/C could perform admirable catalytic properties for AB dehydrogenation.[337] N-hcp-Ni/C delivered good catalytic activity with a TOF value of 15.2 $min^{-1}$, owing to the unusual hcp engineering phase of Ni with N doping. In 2016, Chen *et al.* synthesized Co/CTF and Ni/CTF through an impregnation method with a total turnover frequency of 42.3 $min^{-1}$ at room temperature.[338] The covalent triazine framework (CTF) was rich in N, which gave it an electron-donating effect to increase the electron density of the Co and Ni. Besides, the KIE measurements showed that the breaking of an O–H bond in $H_2O$ was the rate-determining step for AB hydrolysis.

Recently, bimetallic catalysts have gained attention for their potential synergistic effects in the hydrolysis of AB. Vernekar *et al.* reported that the addition of Fe in the Ni–$Ni_3B$ produced strongly positive cooperativity, similar to nature-designed hydrogenase metalloenzymes.[339] The catalyst can effectively reduce the reaction activation energy and maintain a catalytic conversion rate of 100% in several catalytic cycles with a TOF of ~293 $min^{-1}$. Yu *et al.* prepared a ZIF-67 derived $Co_3O_4$ nanoparticles in a carbon-based nano framework with P and Cu co-doping strategy which exhibited an astonishing nearly 51-fold improvement.[340] According to the experimental results and DFT calculations, the strong electronic coupling between Co cation and P anions brought electronic structure regulation and a downshift of d-band, similar to the Cu doping effect. This structural shift produced the apparent activation energy with 29.86 kJ $mol^{-1}$ and a TOF of 35.6 $min^{-1}$. Li *et al.* designed an out-of-plane CoRu nanoalloy axially coupling $Co_sNC$ with superior intrinsic activity and cycle stability at room temperature.[341] The result presented that the electron-enrichment-boosting effect could effectively reduce the reaction energy barrier according to DFT calculations.

Increasing studies have been focused on light-assisted photocatalytic AB hydrolysis to $H_2$. With the help of visible light, dehydrogenation can proceed quickly without heat from external systems. Furthermore, the photocatalytic system is more environmentally friendly and promotes carbon neutrality. The photocatalysts are based on the semiconductor materials such as titanium oxide[342] and carbon nitride.[343] In 2022, Astruc and coworkers prepared AuNi@ZIF-8 alloys under visible-light illumination.[344] The researchers designed a new strategy involving plasmon-induced visible light and maximum synergy among the nanocomponents to boost AB dehydrogenation performances. Filiz *et al.* reported a series of Co doped n-type semiconductors and presented that Co@$TiO_2$–$WO_3$ heterojunction structure had the best performance.[345]

**4.2.2 Methanolysis of ammonia borane.** In recent years, a series of catalysts have been developed for the efficient methanolysis of AB, which provides a new way for the industrial application of chemical energy storage. AB methanolysis has a wider application temperature range than AB hydrolysis due to its low freezing point temperature of −114 °C. The mechanism and the technical means to improve $H_2$ production efficiency are still under study. Yao *et al.* confirmed the cleavage of O–H bond in methanol was involved in the rate-determining step by isotope experiments.[346] Recently, Li *et al.* prepared a series of $Cu_xNi_{1-x}WO_4$ through hydrothermal synthesis as cheap catalysts for AB methanolysis.[347] Among them, $Cu_{0.8}Ni_{0.2}WO_4$ exhibits the highest TOF of 59.0 $mol_{H_2}$ $mol_{cat}^{-1}$ $min^{-1}$ and the catalytic activity can be well maintained after eight cycles. Furthermore, the scission of O–H bond is identified as the rate-determining step. Similarly, heterostructured $Cu_3Mo_2O_9$/$NiMoO_4$ hollow spheres comprised of nanoplatelets were prepared for the reaction, and the optimized catalyst exhibited a TOF of 62.1 $mol_{H_2}$ $mol_{cat}^{-1}$ $min^{-1}$.[348] The upshift of *d* band center of the catalyst provides better chemisorption ability of Ni and Cu sites, favourable for the adsorption and activation of $CH_3OH$ and AB.

### 4.3 Hydrous hydrazine

Hydrous hydrazine ($N_2H_4{\cdot}H_2O$) is considered to be used in the liquid chemical hydrogen storage system, and $N_2$ is the only complete decomposition by-product. Hydrazine hydrate has the advantage of liquid phase at room temperature, high hydrogen content (8.0 wt%), and satisfactory stability.[349,350] It is worth noting that pure hydrazine is prone to explode after contact with metal and hydrous hydrazine does not have this safety hazard. The decomposition of hydrazine includes complete decomposition and incomplete decomposition. The complete decomposition is the ideal reaction, while the incomplete decomposition will produce toxic $NH_3$ and possibly poison catalysts.

$$N_2H_4 \rightarrow N_2 + 2H_2$$

$$3N_2H_4 \rightarrow N_2 + 4NH_3$$

To achieve hydrazine complete decomposition, reducing the energy barrier of N–H cleavage is crucial for the reaction, while N–N bond is easier to be broken than N–H bond.[355] Thus, the metal catalysts are necessary for the reaction due to the stronger M–H bonds than M–N bond.[356] In recent years, some progress has been made in the nanocatalysts for hydrazine dehydrogenation (Table 10). In an early study, Xu *et al.* applied Rh, Co, Ru, Ir, Cu, Ni, Fe, Pt, and Pd nanoparticles (NPs) in hydrazine decomposition.[357] Among them, Rh NPs are confirmed to be the most active catalyst under aqueous conditions,

Table 10 Representative catalysts for hydrazine decomposition

| Catalyst | Temp. (°C) | $H_2$ sel. (%) | TOF ($h^{-1}$) | Ref. |
|---|---|---|---|---|
| Rh NPs | 25 | 43.8 | | 357 |
| Ni/Fe/Pd NPs | 40 | 100 | 25.3 | 358 |
| $Rh_{0.5}(MoO_x)_{0.5}$ NPs | 50 | 100 | 750 | 359 |
| $Ni_{0.69}Pt_{0.31}$ | r.t. | 100 | 7.9 | 360 |
| $Ni_{85}Ir_{15}$@MIL-101 | 25 | 100 | 24 | 361 |

while Fe, Ni, Cu, Pt, and Pd NPs exhibit lower activity. Khan *et al.* prepared tri-metallic nanocatalysts for hydrazine decomposition in a basic solution at low temperatures.[358] Compared to the mono-metallic and bi-metallic catalysts, the tri-metallic catalysts perform good durability and 100% hydrogen selectivity. Lu *et al.* reported a series of Rh-$MoO_x$ NPs prepared *via* a one-step chemical reduction approach without any surfactant/support at room temperature.[359] Typically, $Rh_{0.5}(MoO_x)_{0.5}$ NPs exhibit good catalytic activity with a TOF of 750 $h^{-1}$ and 100% $H_2$ selectivity at 50 °C.

## 5. Concluding remarks

In this article, an overview of major existing LHC systems is provided and some relevant catalytic studies are involved. Currently, LHC technology is at a crucial stage, transitioning from laboratory settings to industrial applications, where it can address the challenges in $H_2$ storage and transportation. As LHC technology advances toward commercialization, it has the potential to transform the energy landscape and create a more open market through the development of diverse hydrogen sources. However, LHC systems still face several key issues that need to be addressed. Hydrocarbons, although economically viable, may not be the optimal choice due to dehydrogenation challenges. Methanol can effectively utilize $CO_2$ as the synthesis raw material; however, CO produced during dehydrogenation can lead to catalyst deactivation. Although ammonia decomposition has achieved profitability in gas station applications, its overall economic viability for large-scale commercialization is still uncertain. Moreover, the low-cost, large-scale production of $NH_3$ remains a challenge. *N*-ethyl carbazole and ammonia borane have attracted considerable attention in recent years, but their costs remain high. Importantly, there is a pressing need to develop catalysts with good activity, selectivity, and stability, either by modifying existing catalysts or employing novel preparation methods like atomic layer deposition.

For LOHC, methanol appears to be the optimized choice due to the high $H_2$ mass and volumetric density as well as the low dehydrogenation enthalpy (Table 1). That is, methanol is the intrinsic better LOHC in comparison with other candidates. In practice, both the synthesis of methanol from $CO_2$–$H_2$ and the $H_2$ release from methanol steam reforming can take place at relatively low temperatures of $<250$ °C in the presence of non-noble metal catalysts such as Cu-based catalysts. Overall, methanol shows unparalleled advantages as LOHC and is ready for industrial applications. Furthermore, using methanol as LOHC can be combined with the management and utilization of $CO_2$ for local carbon neutrality. Ammonia and its derivatives are rising candidates as hydrogen carriers with very high $H_2$ mass and volumetric density. However, many key issues should be addressed before their practical applications. Keep in mind ammonia synthesis from $N_2$ and $H_2$ remains one of the most energy-extensive processes in the chemical industry.

Last but not least, improvements beyond the materials themselves (LHC and catalysts) should be made, focusing on the development of more efficient and cost-effective systems for hydrogen storage and release. By integrating advanced control systems, heat management, and energy recovery strategies, the overall performance of these systems can be significantly enhanced, making them more practical for large-scale implementation.

## Conflicts of interest

There are no conflicts to declare.

## Acknowledgements

This work is supported by the National Key R&D Program of China (2021YFA1501202), National Natural Science Foundation of China (22025203), and the Fundamental Research Funds for the Central Universities (Nankai University).

## References

1 H. J. Schellnhuber, S. Rahmstorf and R. Winkelmann, *Nat. Clim. Change*, 2016, **6**, 649–653.
2 C. F. Shih, T. Zhang, J. Li and C. Bai, *Joule*, 2018, **2**, 1925–1949.
3 P. Preuster, C. Papp and P. Wasserscheid, *Acc. Chem. Res.*, 2017, **50**, 74–85.
4 M. Niermann, S. Drünert, M. Kaltschmitt and K. Bonhoff, *Energy Environ. Sci.*, 2019, **12**, 290–307.
5 A. Züttel, *Mater. Today*, 2003, **6**, 24–33.
6 F. Marques, M. Balcerzak, F. Winkelmann, G. Zepon and M. Felderhoff, *Energy Environ. Sci.*, 2021, **14**, 5191–5227.
7 M. D. Allendorf, Z. Hulvey, T. Gennett, A. Ahmed, T. Autrey, J. Camp, E. Seon Cho, H. Furukawa, M. Haranczyk, M. Head-Gordon, S. Jeong, A. Karkamkar, D.-J. Liu, J. R. Long, K. R. Meihaus, I. H. Nayyar, R. Nazarov, D. J. Siegel, V. Stavila, J. J. Urban, S. P. Veccham and B. C. Wood, *Energy Environ. Sci.*, 2018, **11**, 2784–2812.
8 N. Rao, A. K. Lele and A. W. Patwardhan, *Int. J. Hydrogen Energy*, 2022, **47**, 28530–28547.
9 E. Gianotti, M. Taillades-Jacquin, J. Rozière and D. J. Jones, *ACS Catal.*, 2018, **8**, 4660–4680.
10 G. Sievi, D. Geburtig, T. Skeledzic, A. Bösmann, P. Preuster, O. Brummel, F. Waidhas, M. A. Montero, P. Khanipour, I. Katsounaros, J. Libuda, K. J. J. Mayrhofer and P. Wasserscheid, *Energy Environ. Sci.*, 2019, **12**, 2305–2314.
11 M. Taube, D. W. T. Rippin, D. L. Cresswell and W. Knecht, *Int. J. Hydrogen Energy*, 1983, **8**, 213–225.
12 F. Valentini, A. Marrocchi and L. Vaccaro, *Adv. Energy Mater.*, 2022, **12**, 2103362.
13 A. Bourane, M. Elanany, T. V. Pham and S. P. Katikaneni, *Int. J. Hydrogen Energy*, 2016, **41**, 23075–23091.
14 S. P. Verevkin, V. N. Emel'yanenko, A. Heintz, K. Stark and W. Arlt, *Ind. Eng. Chem. Res.*, 2012, **51**, 12150–12153.
15 Y. Dong, M. Yang, T. Zhu, X. Chen, G. Cheng, H. Ke and H. Cheng, *ACS Appl. Energy Mater.*, 2018, **1**, 4285–4292.

16 L. Li, M. Yang, Y. Dong, P. Mei and H. Cheng, *Int. J. Hydrogen Energy*, 2016, **41**, 16129–16134.
17 Y. Dong, M. Yang, Z. Yang, H. Ke and H. Cheng, *Int. J. Hydrogen Energy*, 2015, **40**, 10918–10922.
18 K. He, F. Tan, C. Zhou, G. Zhou, X. Yang and Y. Li, *Angew. Chem., Int. Ed.*, 2017, **56**, 3080–3084.
19 O. Sebastian, S. Nair, N. Taccardi, M. Wolf, A. Søgaard, M. Haumann and P. Wasserscheid, *ChemCatChem*, 2020, **12**, 4533–4537.
20 D. Balcells, E. Clot and O. Eisenstein, *Chem. Rev.*, 2010, **110**, 749–823.
21 X. Lin, W. Wu and Y. Mo, *Coord. Chem. Rev.*, 2020, **419**, 213401.
22 M. Boudart, in *Adv. Catal.*, ed. D. D. Eley, H. Pines and P. B. Weisz, Academic Press, 1969, vol. 20, pp. 153–166.
23 J. A. C. Rodriguez and C. T. Campbel, *J. Phys. Chem.*, 1989, **93**, 826–835.
24 L. Chen, P. Verma, K. Hou, Z. Qi, S. Zhang, Y.-S. Liu, J. Guo, V. Stavila, M. D. Allendorf, L. Zheng, M. Salmeron, D. Prendergast, G. A. Somorjai and J. Su, *Nat. Commun.*, 2022, **13**, 1092.
25 M. Peng, C. Dong, R. Gao, D. Xiao, H. Liu and D. Ma, *ACS Cent. Sci.*, 2021, **7**, 262–273.
26 Y. Deng, Y. Guo, Z. Jia, J. Liu, J. Guo, X. Cai, C. Dong, M. Wang, C. Li, J. Diao, Z. Jiang, J. Xie, N. Wang, H. Xiao, B. Xu, H. Zhang, H. Liu, J. Li and D. Ma, *J. Am. Chem. Soc.*, 2022, **144**, 3535–3542.
27 B. Wang, G. Froment and D. Goodman, *J. Catal.*, 2008, **253**, 239–243.
28 J. Du, C. Song, J. Song, J. Zhao and Z. Zhu, *J. Fuel Chem. Technol.*, 2009, **37**, 468–472.
29 N. Wang, J. Qiu, J. Wu, X. Yuan, K. You and H. Luo, *Appl. Catal., A*, 2016, **516**, 9–16.
30 B.-H. Jeong, K.-I. Sotowa and K. Kusakabe, *J. Membr. Sci.*, 2003, **224**, 151–158.
31 J. Yu, Q. Ge, W. Fang and H. Xu, *Int. J. Hydrogen Energy*, 2011, **36**, 11536–11544.
32 J. Yu, R. Wang, S. Ren, X. Sun, C. Chen, Q. Ge, W. Fang, J. Zhang, H. Xu and D. S. Su, *ChemCatChem*, 2012, **4**, 1376–1381.
33 S. Furukawa, A. Tamura, K. Ozawa and T. Komatsu, *Appl. Catal., A*, 2014, **469**, 300–305.
34 L. I. Ali, A.-G. A. Ali, S. M. Aboul-Fotouh and A. K. Aboul-Gheit, *Appl. Catal., A*, 1999, **177**, 99–110.
35 A. N. Kalenchuk, V. I. Bogdan, S. F. Dunaev and L. M. Kustov, *Fuel Process. Technol.*, 2018, **169**, 94–100.
36 J. Wang, H. Liu, S. Fan, W. Li, Z. Li, H. Yun, X. Xu, A. Guo and Z. Wang, *Energy Fuels*, 2020, **34**, 16542–16551.
37 L. Zhang, L. Liu, Z. Pan, R. Zhang, Z. Gao, G. Wang, K. Huang, X. Mu, F. Bai, Y. Wang, W. Zhang, Z. Cui and L. Li, *Nat. Energy*, 2022, **7**, 1042–1051.
38 J. S. Kang, J. Y. Baek, H. Hwang, H. S. Shin, C. W. Yoon and H.-J. Shin, *J. Mater. Chem. A*, 2022, **10**, 22701–22706.
39 I. Rodríguez-Ramos and A. Guerrero-Ruiz, *J. Catal.*, 1992, **135**, 458–466.
40 A. H. Al-ShaikhAli, A. Jedidi, L. Cavallo and K. Takanabe, *Chem. Commun.*, 2015, **51**, 12931–12934.
41 D. Gao, Y. Zhi, L. Cao, L. Zhao, J. Gao, C. Xu, M. Ma and P. Hao, *Chin. J. Chem. Eng.*, 2022, **43**, 124–134.
42 Y. Yao, Z. Yan, L. Chen, Z. Zhou, L. Liu and D. W. Goodman, *Catal. Lett.*, 2012, **142**, 1437–1444.
43 J. Escobar, J. A. De Los Reyes, T. Viveros and M. C. Barrera, *Ind. Eng. Chem. Res.*, 2006, **45**, 5693–5700.
44 R. B. Biniwale, N. Kariya and M. Ichikawa, *Catal. Lett.*, 2005, **105**, 83–87.
45 Z. Xia, H. Lu, H. Liu, Z. Zhang and Y. Chen, *Catal. Commun.*, 2017, **90**, 39–42.
46 Z. Xia, H. Liu, H. Lu, Z. Zhang and Y. Chen, *Appl. Surf. Sci.*, 2017, **422**, 905–912.
47 J. Li, Y. Chai, B. Liu, Y. Wu, X. Li, Z. Tang, Y. Liu and C. Liu, *Appl. Catal., A*, 2014, **469**, 434–441.
48 K. Choojun, A. Worathanaseth, S. Kuhatasanadeekul, T. Kurato, S. Ketaniruj, P. Phichitsurathaworn, P. Promchana, K. Prakobtham, N. Numwong, Y. Poo-arporn and T. Sooknoi, *Catal. Commun.*, 2019, **125**, 108–113.
49 M. Raad, A. Astafan, S. Hamieh, J. Toufaily, T. Hamieh, J. D. Comparot, C. Canaff, T. J. Daou, J. Patarin and L. Pinard, *J. Catal.*, 2018, **365**, 376–390.
50 H. Wang, N. Zhang, R. Liu, R. Zhao, T. Guo, J. Li, T. Asefa and J. Du, *ACS Omega*, 2018, **3**, 10773–10780.
51 Z. Xia, H. Liu, H. Lu, Z. Zhang and Y. Chen, *Catal. Lett.*, 2017, **147**, 1295–1302.
52 J. V. Pande, A. Shukla and R. B. Biniwale, *Int. J. Hydrogen Energy*, 2012, **37**, 6756–6763.
53 G. Zhou, T. Li, J. Chen, L. Deng and H. Xie, *Int. J. Hydrogen Energy*, 2021, **46**, 14540–14555.
54 J. V. Pande, A. B. Bindwal, Y. B. Pakade and R. B. Biniwale, *Int. J. Hydrogen Energy*, 2018, **43**, 7411–7423.
55 H. M. Gobara, R. S. Mohamed and W. A. Aboutaleb, *Microporous Mesoporous Mater.*, 2021, **323**, 111151.
56 Z. Kou, S. Shen, K. Liu, G. Xu, Y. An and C. He, *Int. J. Hydrogen Energy*, 2013, **38**, 11930–11936.
57 K. Takise, A. Sato, K. Murakami, S. Ogo, J. G. Seo, K.-I. Imagawa, S. Kado and Y. Sekine, *RSC Adv.*, 2019, **9**, 5918–5924.
58 J. Meng, F. Zhou, H. Ma, X. Yuan, Y. Wang and J. Zhang, *Top. Catal.*, 2021, **64**, 509–520.
59 Q. Zhu and Q. Xu, *Energy Environ. Sci.*, 2015, **8**, 478–512.
60 F. Alhumaidan, D. Tsakiris, D. Cresswell and A. Garforth, *Int. J. Hydrogen Energy*, 2013, **38**, 14010–14026.
61 A. A. Shukla, P. V. Gosavi, J. V. Pande, V. P. Kumar, K. V. R. Chary and R. B. Biniwale, *Int. J. Hydrogen Energy*, 2010, **35**, 4020–4026.
62 A. Shukla, J. V. Pande and R. B. Biniwale, *Int. J. Hydrogen Energy*, 2012, **37**, 3350–3357.
63 X. Li, D. Ma and B. Xinhe, *Chin. J. Catal.*, 2008, **29**, 259–263.
64 C. Zhang, X. Liang and S. Liu, *Int. J. Hydrogen Energy*, 2011, **36**, 8902–8907.
65 D. K. Cromwell, P. T. Vasudevan, B. Pawelec and J. L. G. Fierro, *Catal. Today*, 2016, **259**, 119–129.
66 X. Zhang, N. He, L. Lin, Q. Zhu, G. Wang and H. Guo, *Catal. Sci. Technol.*, 2020, **10**, 1171–1181.
67 X. Yang, Y. Song, T. Cao, L. Wang, H. Song and W. Lin, *Mol. Catal.*, 2020, **492**, 110971.

68 Y. Sugiura, T. Nagatsuka, K. Kubo, Y. Hirano, A. Nakamura, K. Miyazawa, Y. Iizuka, S. Furuta, H. Iki, T. Higo and Y. Sekine, *Chem. Lett.*, 2017, **46**, 1601–1604.
69 J. Yan, W. Wang, L. Miao, K. Wu, G. Chen, Y. Huang and Y. Yang, *Int. J. Hydrogen Energy*, 2018, **43**, 9343–9352.
70 W. Wang, L. Miao, K. Wu, G. Chen, Y. Huang and Y. Yang, *Int. J. Hydrogen Energy*, 2019, **44**, 2918–2925.
71 N. Boufaden, R. Akkari, B. Pawelec, J. L. G. Fierro, M. S. Zina and A. Ghorbel, *J. Mol. Catal. A: Chem.*, 2016, **420**, 96–106.
72 S. Manabe, T. Yabe, A. Nakano, S. Nagatake, T. Higo, S. Ogo, H. Nakai and Y. Sekine, *Chem. Phys. Lett.*, 2018, **711**, 73–76.
73 A. Nakano, S. Manabe, T. Higo, H. Seki, S. Nagatake, T. Yabe, S. Ogo, T. Nagatsuka, Y. Sugiura, H. Iki and Y. Sekine, *Appl. Catal., A*, 2017, **543**, 75–81.
74 L. Zhang, G. Xu, Y. An, C. Chen and Q. Wang, *Int. J. Hydrogen Energy*, 2006, **31**, 2250–2255.
75 S. Yolcular and Ö. Olgun, *Catal. Today*, 2008, **138**, 198–202.
76 S. P. Patil, J. V. Pande and R. B. Biniwale, *Int. J. Hydrogen Energy*, 2013, **38**, 15233–15241.
77 A. H. Al-ShaikhAli, A. Jedidi, D. H. Anjum, L. Cavallo and K. Takanabe, *ACS Catal.*, 2017, **7**, 1592–1600.
78 N. Boufaden, R. Akkari, B. Pawelec, J. L. G. Fierro, M. Said Zina and A. Ghorbel, *Appl. Catal., A*, 2015, **502**, 329–339.
79 S. Hodoshima, *Int. J. Hydrogen Energy*, 2003, **28**, 1255–1262.
80 J. J. H. B. Sattler, J. Ruiz-Martinez, E. Santillan-Jimenez and B. M. Weckhuysen, *Chem. Rev.*, 2014, **114**, 10613–10653.
81 Y. Tuo, L. Yang, H. Cheng, M. Yang, Y. Zhu and P. Li, *Int. J. Hydrogen Energy*, 2018, **43**, 19575–19588.
82 S. Hodoshima, S. Takaiwa, A. Shono, K. Satoh and Y. Saito, *Appl. Catal., A*, 2005, **283**, 235–242.
83 D. Sebastián, E. G. Bordejé, L. Calvillo, M. J. Lázaro and R. Moliner, *Int. J. Hydrogen Energy*, 2008, **33**, 1329–1334.
84 X. Wu, H. Lu, Y. Xiao, H. Guo, L. Jia and D. Li, *Int. J. Hydrogen Energy*, 2022, **47**, 34955–34962.
85 K. Murata, N. Kurimoto, Y. Yamamoto, A. Oda, J. Ohyama and A. Satsuma, *ACS Appl. Nano Mater.*, 2021, **4**, 4532–4541.
86 Y. Nakaya, M. Miyazaki, S. Yamazoe, K.-I. Shimizu and S. Furukawa, *ACS Catal.*, 2020, **10**, 5163–5172.
87 D. Wang, Q. Lei, H. Li, G. Li and Y. Zhao, *Catalysts*, 2022, **12**, 958.
88 H. Ye, S. Liu, C. Zhang, Y. Cai and Y. Shi, *RSC Adv.*, 2021, **11**, 29287–29297.
89 M. V. Alekseeva, Y. K. Gulyaeva, O. A. Bulavchenko, A. A. Saraev, A. M. Kremneva, S. A. Stepanenko, A. P. Koskin, V. V. Kaichev and V. A. Yakovlev, *Dalton Trans.*, 2022, **51**, 6068–6085.
90 Y. Tuo, L. Yang, X. Ma, Z. Ma, S. Gong and P. Li, *Int. J. Hydrogen Energy*, 2021, **46**, 930–942.
91 Y. Tuo, Y. Meng, C. Chen, D. Lin, X. Feng, Y. Pan, P. Li, D. Chen, Z. Liu, Y. Zhou and J. Zhang, *Appl. Catal., B*, 2021, **288**, 119996.
92 S. Qi, Y. Li, J. Yue, H. Chen, C. Yi and B. Yang, *Chin. J. Catal.*, 2014, **35**, 1833–1839.
93 K. Kim, J. Oh, T. W. Kim, J. H. Park, J. W. Han and Y.-W. Suh, *Catal. Sci. Technol.*, 2017, **7**, 3728–3735.
94 A. A. Al-Muntaser, M. A. Varfolomeev, M. A. Suwaid, M. M. Saleh, R. Djimasbe, C. Yuan, R. R. Zairov and J. Ancheyta, *Fuel*, 2022, **313**, 122652.
95 Y. Suttisawat, H. Sakai, M. Abe, P. Rangsunvigit and S. Horikoshi, *Int. J. Hydrogen Energy*, 2012, **37**, 3242–3250.
96 N. Brückner, K. Obesser, A. Bösmann, D. Teichmann, W. Arlt, J. Dungs and P. Wasserscheid, *ChemSusChem*, 2014, **7**, 229–235.
97 H. Jorschick, P. Preuster, S. Dürr, A. Seidel, K. Müller, A. Bösmann and P. Wasserscheid, *Energy Environ. Sci.*, 2017, **10**, 1652–1659.
98 L. Shi, Y. Zhou, S. Qi, K. J. Smith, X. Tan, J. Yan and C. Yi, *ACS Catal.*, 2020, **10**, 10661–10671.
99 R. Garidzirai, P. Modisha, I. Shuro, J. Visagie, P. van Helden and D. Bessarabov, *Catalysts*, 2021, **11**, 490.
100 J. Zhou, J. S. Chung and S. G. Kang, *Appl. Surf. Sci.*, 2022, **579**, 152142.
101 M. Niermann, S. Timmerberg, S. Drünert and M. Kaltschmitt, *Renewable Sustainable Energy Rev.*, 2021, **135**, 110171.
102 Z. Chen, M. Yang, T. Zhu, Z. Zhang, X. Chen, Z. Liu, Y. Dong, G. Cheng and H. Cheng, *Int. J. Hydrogen Energy*, 2018, **43**, 12688–12696.
103 S. Lim, Y. Song, K. Jeong, J. H. Park and K. Na, *ACS Sustainable Chem. Eng.*, 2022, **10**, 3584–3594.
104 A. Søgaard, M. Scheuermeyer, A. Bösmann, P. Wasserscheid and A. Riisager, *Chem. Commun.*, 2019, **55**, 2046–2049.
105 Z. Jiang, X. Gong, S. Guo, Y. Bai and T. Fang, *Int. J. Hydrogen Energy*, 2021, **46**, 2376–2389.
106 J. Steinhauer, P. Bachmann, E. M. Freiberger, U. Bauer, H. P. Steinrück and C. Papp, *J. Phys. Chem. C*, 2020, **124**, 22559–22567.
107 Y. Cui, S. Kwok, A. Bucholtz, B. Davis, R. A. Whitney and P. G. Jessop, *New J. Chem.*, 2008, **32**, 1027.
108 P. Ryabchuk, A. Agapova, C. Kreyenschulte, H. Lund, H. Junge, K. Junge and M. Beller, *Chem. Commun.*, 2019, **55**, 4969–4972.
109 Y. Dong, H. Zhao, Y. Zhao, M. Yang, H. Zhang and H. Cheng, *RSC Adv.*, 2021, **11**, 15729–15737.
110 M. Schwarz, P. Bachmann, T. N. Silva, S. Mohr, M. Scheuermeyer, F. Späth, U. Bauer, F. Düll, J. Steinhauer, C. Hohner, T. Döpper, H. Noei, A. Stierle, C. Papp, H. P. Steinrück, P. Wasserscheid, A. Görling and J. Libuda, *Chem. – Eur. J.*, 2017, **23**, 14806–14818.
111 H. Chen, Z. Yang, Z. Zhang, Z. Chen, M. Chi, S. Wang, J. Fu and S. Dai, *Angew. Chem., Int. Ed.*, 2019, **58**, 10626–10630.
112 Y. Ding, Y. Dong, H. Zhang, Y. Zhao, M. Yang and H. Cheng, *Int. J. Hydrogen Energy*, 2021, **46**, 27026–27036.
113 Z. Feng and X. Bai, *Microporous Mesoporous Mater.*, 2022, **335**, 111789.
114 X. Yang, Y. Wu, H. Yu, M. Sun, J. Zheng, X. Li, W. Lin and Y. Wu, *Int. J. Hydrogen Energy*, 2020, **45**, 33657–33662.
115 F. Sotoodeh, B. J. M. Huber and K. J. Smith, *Appl. Catal., A*, 2012, **419–420**, 67–72.
116 Y.-Q. Zou, N. von Wolff, A. Anaby, Y. Xie and D. Milstein, *Nat. Catal.*, 2019, **2**, 415–422.
117 Z. Jiang, X. Gong, B. Wang, Z. Wu and T. Fang, *Int. J. Hydrogen Energy*, 2019, **44**, 2951–2959.

118 M. Yang, Y. Dong, S. Fei, H. Ke and H. Cheng, *Int. J. Hydrogen Energy*, 2014, **39**, 18976–18983.
119 F. Sotoodeh, L. Zhao and K. J. Smith, *Appl. Catal., A*, 2009, **362**, 155–162.
120 B. Wang, T. Yan, T. Chang, J. Wei, Q. Zhou, S. Yang and T. Fang, *Carbon*, 2017, **122**, 9–18.
121 M. Zhu, L. Xu, L. Du, Y. An and C. Wan, *Catalysts*, 2018, **8**, 638.
122 B. Wang, Y. Chen, T. Chang, Z. Jiang, Z. Huang, S. Wang, C. Chang, Y. Chen, J. Wei, S. Yang and T. Fang, *Appl. Catal., B*, 2020, **266**, 118658.
123 F. Sotoodeh and K. J. Smith, *J. Catal.*, 2011, **279**, 36–47.
124 Y. Dong, M. Yang, P. Mei, C. Li and L. Li, *Int. J. Hydrogen Energy*, 2016, **41**, 8498–8505.
125 M. Sobota, I. Nikiforidis, M. Amende, B. S. Zanón, T. Staudt, O. Höfert, Y. Lykhach, C. Papp, W. Hieringer, M. Laurin, D. Assenbaum, P. Wasserscheid, H.-P. Steinrück, A. Görling and J. Libuda, *Chem. – Eur. J.*, 2011, **17**, 11542–11552.
126 H. Shuang, H. Chen, F. Wu, J. Li, C. Cheng, H. Li and J. Fu, *Fuel*, 2020, **275**, 117896.
127 Z. Feng, Y. Wang and X. Bai, *Environ. Sci. Pollut. Res.*, 2022, **29**, 39266–39280.
128 C. Tang, Z. Feng and X. Bai, *Fuel*, 2021, **302**, 121186.
129 C. Dong, Z. Gao, Y. Li, M. Peng, M. Wang, Y. Xu, C. Li, M. Xu, Y. Deng, X. Qin, F. Huang, X. Wei, Y. Wang, H. Liu, W. Zhou and D. Ma, *Nat. Catal.*, 2022, **5**, 485–493.
130 M. Amende, C. Gleichweit, K. Werner, S. Schernich, W. Zhao, M. P. A. Lorenz, O. Höfert, C. Papp, M. Koch, P. Wasserscheid, M. Laurin, H.-P. Steinrück and J. Libuda, *ACS Catal.*, 2014, **4**, 657–665.
131 M. Amende, C. Gleichweit, S. Schernich, O. Höfert, M. P. A. Lorenz, W. Zhao, M. Koch, K. Obesser, C. Papp, P. Wasserscheid, H.-P. Steinrück and J. Libuda, *J. Phys. Chem. Lett.*, 2014, **5**, 1498–1504.
132 W. Peters, A. Seidel, S. Herzog, A. Bösmann, W. Schwieger and P. Wasserscheid, *Energy Environ. Sci.*, 2015, **8**, 3013–3021.
133 X. Gong, Z. Jiang and T. Fang, *Int. J. Hydrogen Energy*, 2020, **45**, 6838–6847.
134 Z. Yang, X. Gong, L. Li, Z. Jiang, R. Zhang and T. Fang, *Fuel*, 2023, **334**, 126733.
135 Y. Wu, Y. Guo, H. Yu, X. Jiang, Y. Zhang, Y. Qi, K. Fu, L. Xie, G. Li, J. Zheng and X. Li, *CCS Chem.*, 2021, **3**, 974–984.
136 S. Fei, Y. Wang, H. Wu, N. Zheng, X. Fang and D. Liu, *ACS Appl. Energy Mater.*, 2022, **5**, 10562–10571.
137 B. Wang, T. Chang, X. Gong, Z. Jiang, S. Yang, Y. Chen and T. Fang, *ACS Sustainable Chem. Eng.*, 2018, **7**, 1760–1768.
138 W. Xue, H. Liu, B. Zhao, C. Tang, B. Y. Xia and B. You, *ChemSusChem*, 2023, **16**, e202201512.
139 W. Xue, H. Liu, B. Mao, H. Liu, M. Qiu, C. Yang, X. Chen and Y. Sun, *Chem. Eng. J.*, 2021, **421**, 127781.
140 A. Ali, U. Kumar G and H. J. Lee, *J. Mech. Sci. Technol.*, 2019, **33**, 5561–5569.
141 K. M. Eblagon, K. Tam and S. C. E. Tsang, *Energy Environ. Sci.*, 2012, **5**, 8621.
142 M. Yang, C. Han, G. Ni, J. Wu and H. Cheng, *Int. J. Hydrogen Energy*, 2012, **37**, 12839–12845.
143 K. Morawa Eblagon, K. Tam, K. M. K. Yu, S.-L. Zhao, X.-Q. Gong, H. He, L. Ye, L.-C. Wang, A. J. Ramirez-Cuesta and S. C. Tsang, *J. Phys. Chem. C*, 2010, **114**, 9720–9730.
144 L. Ge, M. Qiu, Y. Zhu, S. Yang, W. Li, W. Li, Z. Jiang and X. Chen, *Appl. Catal., B*, 2022, **319**, 121958.
145 H. Yu, X. Yang, X. Jiang, Y. Wu, S. Chen, W. Lin, Y. Wu, L. Xie, X. Li and J. Zheng, *Nano Energy*, 2021, **80**, 105476.
146 Y. Wu, H. Yu, Y. Guo, X. Jiang, Y. Qi, B. Sun, H. Li, J. Zheng and X. Li, *Chem. Sci.*, 2019, **10**, 10459–10465.
147 X. Liu, J. Shi, X. Bai and W. Wu, *Environ. Sci. Pollut. Res.*, 2022, **29**, 48558–48572.
148 Z. Jiang, S. Guo and T. Fang, *ACS Appl. Energy Mater.*, 2019, **2**, 7233–7243.
149 J. Li, F. Tong, Y. Li, X. Liu, Y. Guo and Y. Wang, *Fuel*, 2022, **321**, 124034.
150 X. Gong, S. Guo, Z. Jiang, B. Yang and T. Fang, *Int. J. Hydrogen Energy*, 2021, **46**, 33835–33848.
151 C. N. M. Ouma, P. M. Modisha and D. Bessarabov, *Appl. Surf. Sci.*, 2019, **471**, 1034–1040.
152 S. A. Stepanenko, D. M. Shivtsov, A. P. Koskin, I. P. Koskin, R. G. Kukushkin, P. M. Yeletsky and V. A. Yakovlev, *Catalysts*, 2022, **12**, 1260.
153 P. Bachmann, J. Steinhauer, F. Späth, F. Düll, U. Bauer, R. Eschenbacher, F. Hemauer, M. Scheuermeyer, A. Bösmann, M. Büttner, C. Neiß, A. Görling, P. Wasserscheid, H.-P. Steinrück and C. Papp, *J. Chem. Phys.*, 2019, **151**, 144711.
154 B. Brigljević, M. Byun and H. Lim, *Appl. Energy*, 2020, **274**, 115314.
155 R. M. Cuéllar-Franca and A. Azapagic, *J. CO2 Util.*, 2015, **9**, 82–102.
156 F. Sha, Z. Han, S. Tang, J. Wang and C. Li, *ChemSusChem*, 2020, **13**, 6160–6181.
157 G. A. Olah, *Angew. Chem., Int. Ed.*, 2005, **44**, 2636–2639.
158 A. Iulianelli, P. Ribeirinha, A. Mendes and A. Basile, *Renewable Sustainable Energy Rev.*, 2014, **29**, 355–368.
159 S. T. Yong, C. W. Ooi, S. P. Chai and X. S. Wu, *Int. J. Hydrogen Energy*, 2013, **38**, 9541–9552.
160 C. Rameshan, W. Stadlmayr, S. Penner, H. Lorenz, N. Memmel, M. Hävecker, R. Blume, D. Teschner, T. Rocha, D. Zemlyanov, A. Knop-Gericke, R. Schlögl and B. Klötzer, *Angew. Chem., Int. Ed.*, 2012, **51**, 3002–3006.
161 I. Kasatkin, P. Kurr, B. Kniep, A. Trunschke and R. Schlögl, *Angew. Chem., Int. Ed.*, 2007, **46**, 7324–7327.
162 K. C. Waugh, *Catal. Today*, 1992, **15**, 51–75.
163 K. Klier, in *Adv. Catal.*, ed. D. D. Eley, H. Pines and P. B. Weisz, Academic Press, 1982, vol. 31, pp. 243–313.
164 V. Ponec, *Surf. Sci.*, 1992, **272**, 111–117.
165 N. Y. Topsøe and H. Topsøe, *Top. Catal.*, 1999, **8**, 267–270.
166 Y. Choi, K. Futagami, T. Fujitani and J. Nakamura, *Appl. Catal., A*, 2001, **208**, 163–167.
167 M. M. Günter, T. Ressler, R. E. Jentoft and B. Bems, *J. Catal.*, 2001, **203**, 133–149.
168 J. C. Frost, *Nature*, 1988, **334**, 577–580.
169 B. Lindström and L. J. Pettersson, *Catal. Lett.*, 2001, **74**, 27–30.
170 B. Kniep, F. Girgsdies and T. Ressler, *J. Catal.*, 2005, **236**, 34–44.

171 B. L. Kniep, T. Ressler, A. Rabis, F. Girgsdies, M. Baenitz, F. Steglich and R. Schlögl, *Angew. Chem., Int. Ed.*, 2004, **43**, 112–115.
172 C. Mateos-Pedrero, H. Silva, D. A. Pacheco Tanaka, S. Liguori, A. Iulianelli, A. Basile and A. Mendes, *Appl. Catal., B*, 2015, **174–175**, 67–76.
173 D. Li, F. Xu, X. Tang, S. Dai, T. Pu, X. Liu, P. Tian, F. Xuan, Z. Xu, I. E. Wachs and M. Zhu, *Nat. Catal.*, 2022, **5**, 99–108.
174 Z. Cheng, W. Zhou, G. Lan, X. Sun, X. Wang, C. Jiang and Y. Li, *J. Energy Chem.*, 2021, **63**, 550–557.
175 J. Lin, C. Hu, X. Xu, M. Shao, Y. Hu and C. Ma, *Chem. Eng. Technol.*, 2021, **44**, 1121–1130.
176 J. He, Z. Yang, L. Zhang, Y. Li and L. Pan, *Int. J. Hydrogen Energy*, 2017, **42**, 9930–9937.
177 H. Xi, X. Hou, Y. Liu, S. Qing and Z. Gao, *Angew. Chem., Int. Ed.*, 2014, **53**, 11886–11889.
178 Y. Liu, S. Qing, X. Hou, F. Qin, X. Wang, Z. Gao and H. Xiang, *Catal. Sci. Technol.*, 2017, **7**, 5069–5078.
179 Y. Liu, H. Kang, X. Hou, S. Qing, L. Zhang, Z. Gao and H. Xiang, *Appl. Catal., B*, 2023, **323**, 122043.
180 Y. Liu, S. Qing, X. Hou, F. Qin, X. Wang, Z. Gao and H. Xiang, *ChemCatChem*, 2018, **10**, 5698–5706.
181 H.-K. Huang, Y.-K. Chih, W.-H. Chen, C.-Y. Hsu, K.-J. Lin, H.-P. Lin and C.-H. Hsu, *Int. J. Hydrogen Energy*, 2022, **47**, 37542–37551.
182 J. L. C. Fajín and M. N. D. S. Cordeiro, *ACS Catal.*, 2021, **12**, 512–526.
183 K. Ploner, M. Watschinger, P. D. Kheyrollahi Nezhad, T. Götsch, L. Schlicker, E.-M. Köck, A. Gurlo, A. Gili, A. Doran, L. Zhang, N. Köwitsch, M. Armbrüster, S. Vanicek, W. Wallisch, C. Thurner, B. Klötzer and S. Penner, *J. Catal.*, 2020, **391**, 497–512.
184 K. Ploner, P. Delir Kheyrollahi Nezhad, M. Watschinger, L. Schlicker, M. F. Bekheet, A. Gurlo, A. Gili, A. Doran, S. Schwarz, M. Stöger-Pollach, J. Bernardi, M. Armbrüster, B. Klötzer and S. Penner, *Appl. Catal., A*, 2021, **623**, 118279.
185 C. Mateos-Pedrero, C. Azenha, D. A. Pacheco Tanaka, J. M. Sousa and A. Mendes, *Appl. Catal., B*, 2020, **277**, 119243.
186 F. Bossola, N. Scotti, F. Somodi, M. Coduri, C. Evangelisti and V. Dal Santo, *Appl. Catal., B*, 2019, **258**, 118016.
187 C. Azenha, T. Lagarteira, C. Mateos-Pedrero and A. Mendes, *Int. J. Hydrogen Energy*, 2021, **46**, 17490–17499.
188 M. Liao, H. Qin, W. Guo, P. Gao, J. Liu and H. Xiao, *Int. J. Hydrogen Energy*, 2022, **47**, 35136–35148.
189 K. M. K. Yu, W. Tong, A. West, K. Cheung, T. Li, G. Smith, Y. Guo and S. C. E. Tsang, *Nat. Commun.*, 2012, **3**, 1230.
190 T.-W. Chiu, R.-T. Hong, B.-S. Yu, Y.-H. Huang, S. Kameoka and A.-P. Tsai, *Int. J. Hydrogen Energy*, 2014, **39**, 14222–14226.
191 R.-J. Huang, S. Sakthinathan, T.-W. Chiu and C. Dong, *RSC Adv.*, 2021, **11**, 12607–12613.
192 B.-Y. Hwang, S. Sakthinathan and T.-W. Chiu, *Int. J. Hydrogen Energy*, 2019, **44**, 2848–2856.
193 C.-L. Yu, S. Sakthinathan, B.-Y. Hwang, S.-Y. Lin, T.-W. Chiu, B.-S. Yu, Y.-J. Fan and C. Chuang, *Int. J. Hydrogen Energy*, 2020, **45**, 15752–15762.
194 C.-L. Yu, S. Sakthinathan, S.-Y. Chen, B.-S. Yu, T.-W. Chiu and C. Dong, *Microporous Mesoporous Mater.*, 2021, **324**, 111305.
195 F. Bossola, T. Roongcharoen, M. Coduri, C. Evangelisti, F. Somodi, L. Sementa, A. Fortunelli and V. Dal Santo, *Appl. Catal., B*, 2021, **297**, 120398.
196 O. O. Fasanya, A. Y. Atta, M. T. Z. Myint, J. Dutta and B. Y. Jibril, *Int. J. Hydrogen Energy*, 2021, **46**, 3539–3553.
197 Y. Chen and Y. Huang, *Int. J. Hydrogen Energy*, 2023, **48**, 1323–1336.
198 M. Taghizadeh, H. Akhoundzadeh, A. Rezayan and M. Sadeghian, *Int. J. Hydrogen Energy*, 2018, **43**, 10926–10937.
199 Q. Wang, G. Zhang, J. Zhao, L. Zhang and Q. Zhang, *Int. J. Hydrogen Energy*, 2022, **47**, 25256–25265.
200 G. Zhang, J. Zhao, Q. Wang, T. Yang, Q. Zhang and L. Zhang, *Chem. Eng. J.*, 2021, **426**, 130644.
201 S. Sá, H. Silva, L. Brandão, J. M. Sousa and A. Mendes, *Appl. Catal., B*, 2010, **99**, 43–57.
202 T. Valdés-Solís, G. Marbán and A. B. Fuertes, *Catal. Today*, 2006, **116**, 354–360.
203 Y. Matsumura and H. Ishibe, *Appl. Catal., B*, 2009, **91**, 524–532.
204 S. D. Jones, L. M. Neal and H. E. Hagelin-Weaver, *Appl. Catal., B*, 2008, **84**, 631–642.
205 S. D. Jones and H. E. Hagelin-Weaver, *Appl. Catal., B*, 2009, **90**, 195–204.
206 L. Chen, Z. Qi, X. Peng, J.-L. Chen, C.-W. Pao, X. Zhang, C. Dun, M. Young, D. Prendergast, J. J. Urban, J. Guo, G. A. Somorjai and J. Su, *J. Am. Chem. Soc.*, 2021, **143**, 12074–12081.
207 R. Pérez-Hernández, *Int. J. Hydrogen Energy*, 2021, **46**, 25954–25964.
208 L. Lin, W. Zhou, R. Gao, S. Yao, X. Zhang, W. Xu, S. Zheng, Z. Jiang, Q. Yu, Y. Li, C. Shi, X. Wen and D. Ma, *Nature*, 2017, **544**, 80–83.
209 L. Lin, Q. Yu, M. Peng, A. Li, S. Yao, S. Tian, X. Liu, A. Li, Z. Jiang, R. Gao, X. Han, Y. Li, X. Wen, W. Zhou and D. Ma, *J. Am. Chem. Soc.*, 2021, **143**, 309–317.
210 F. Cai, J. J. Ibrahim, Y. Fu, W. Kong, J. Zhang and Y. Sun, *Appl. Catal., B*, 2020, **264**, 118500.
211 D. Li, Y. Li, X. Liu, Y. Guo, C.-W. Pao, J.-L. Chen, Y. Hu and Y. Wang, *ACS Catal.*, 2019, **9**, 9671–9682.
212 Z. Shao, S. Zhang, X. Liu, H. Luo, C. Huang, H. Zhou, Z. Wu, J. Li, H. Wang and Y. Sun, *Appl. Catal., B*, 2022, **316**, 121669.
213 H. Wang, L. Wang, D. Lin, X. Feng, X. Chu, L. Li and F.-S. Xiao, *Catal. Today*, 2021, **382**, 42–47.
214 M. Kusche, F. Agel, N. Ní Bhriain, A. Kaftan, M. Laurin, J. Libuda and P. Wasserscheid, *ChemSusChem*, 2014, **7**, 2516–2526.
215 M. Kusche, F. Enzenberger, S. Bajus, H. Niedermeyer, A. Bösmann, A. Kaftan, M. Laurin, J. Libuda and P. Wasserscheid, *Angew. Chem., Int. Ed.*, 2013, **52**, 5028–5032.
216 N. Iwasa, S. Masuda, N. Ogawa and N. Takezawa, *Appl. Catal., A*, 1995, **125**, 145–157.
217 A. M. Karim, T. Conant and A. K. Datye, *Phys. Chem. Chem. Phys.*, 2008, **10**, 5584–5590.

218 H. Zhang, J. Sun, V. L. Dagle, B. Halevi, A. K. Datye and Y. Wang, *ACS Catal.*, 2014, **4**, 2379–2386.
219 Y. Chen, Q. Dai, Q. Zhang and Y. Huang, *Int. J. Hydrogen Energy*, 2022, **47**, 14869–14883.
220 L. Liu, Y. Lin, Y. Hu, Z. Lin, S. Lin, M. Du, L. Zhang, X. Zhang, J. Lin, Z. Zhang, H. Xiong, S. Wang, B. Ge, S. Wan and Y. Wang, *ACS Catal.*, 2022, **12**, 2714–2721.
221 N. Köwitsch, L. Thoni, B. Klemmed, A. Benad, P. Paciok, M. Heggen, I. Köwitsch, M. Mehring, A. Eychmüller and M. Armbrüster, *ACS Catal.*, 2021, **11**, 304–312.
222 S. Penner, B. Jenewein, H. Gabasch, B. Klötzer, D. Wang, A. Knop-Gericke, R. Schlögl and K. Hayek, *J. Catal.*, 2006, **241**, 14–19.
223 N. Iwasa, T. Mayanagi, W. Nomura, M. Arai and N. Takezawa, *Appl. Catal., A*, 2003, **248**, 153–160.
224 T. Conant, A. M. Karim, V. Lebarbier, Y. Wang, F. Girgsdies, R. Schlögl and A. Datye, *J. Catal.*, 2008, **257**, 64–70.
225 Y. Suwa, S.-i Ito, S. Kameoka, K. Tomishige and K. Kunimori, *Appl. Catal., A*, 2004, **267**, 9–16.
226 B. Halevi, E. J. Peterson, A. Roy, A. DeLariva, E. Jeroro, F. Gao, Y. Wang, J. M. Vohs, B. Kiefer, E. Kunkes, M. Hävecker, M. Behrens, R. Schlögl and A. K. Datye, *J. Catal.*, 2012, **291**, 44–54.
227 R. Pérez-Hernández, A. D. Avendaño, E. Rubio and V. Rodríguez-Lugo, *Top. Catal.*, 2011, **54**, 572–578.
228 C.-W. Tang, Y.-J. Chen, C.-T. Yeh, R.-C. Wu, C.-C. Wang and C.-B. Wang, *Int. J. Hydrogen Energy*, 2021, **46**, 80–88.
229 C. Pojanavaraphan, A. Luengnaruemitchai and E. Gulari, *Int. J. Hydrogen Energy*, 2013, **38**, 1348–1362.
230 H. Lorenz, W. Jochum, B. Klötzer, M. Stöger-Pollach, S. Schwarz, K. Pfaller and S. Penner, *Appl. Catal., A*, 2008, **347**, 34–42.
231 H. Lorenz, M. Friedrich, M. Armbrüster, B. Klötzer and S. Penner, *J. Catal.*, 2013, **297**, 151–154.
232 W. Cao, G. Chen, S. Li and Q. Yuan, *Chem. Eng. J.*, 2006, **119**, 93–98.
233 X. Chen, J. Wang, Z. Han, C. Li, C. Tang, D. Zhao, Q. Yang and C. Li, *ChemCatChem*, 2021, **14**, e202101232.
234 X. Chen, Z. Feng, D. Zhao, Q. Yang and C. Li, *Catal. Sci. Technol.*, 2022, **12**, 7048–7056.
235 Z. Cheng, C. Jiang, X. Sun, G. Lan, X. Wang, L. He, Y. Li, H. Tang and Y. Li, *Ind. Eng. Chem. Res.*, 2022, **61**, 11699–11707.
236 J. Zhao, G. Zhang, H. Liu, Q. Shu and Q. Zhang, *Int. J. Hydrogen Energy*, 2022, **47**, 18294–18304.
237 C.-C. Chang, J.-W. Wang, C.-T. Chang, B.-J. Liaw and Y.-Z. Chen, *Chem. Eng. J.*, 2012, **192**, 350–356.
238 G. Huang, B.-J. Liaw, C.-J. Jhang and Y.-Z. Chen, *Appl. Catal., A*, 2009, **358**, 7–12.
239 Y. Matsumura and H. Ishibe, *J. Power Sources*, 2012, **209**, 72–80.
240 S. Jin, D. Li, Z. Wang, Y. Wang, L. Sun and M. Zhu, *Catal. Sci. Technol.*, 2022, **12**, 7003–7009.
241 X. Liu, J. Xu, S. Li, Z. Chen, X. Xu, X. Fang and X. Wang, *Catal. Today*, 2022, **402**, 228–240.
242 M. Taghizadeh and M. H. Abbandanak, *Int. J. Hydrogen Energy*, 2022, **47**, 16362–16374.
243 R. Y. Abrokwah, V. G. Deshmane and D. Kuila, *J. Mol. Catal. A: Chem.*, 2016, **425**, 10–20.
244 H. Shahsavar, M. Taghizadeh and A. D. Kiadehi, *Int. J. Hydrogen Energy*, 2021, **46**, 8906–8921.
245 N. Kamyar, Y. Khani, M. M. Amini, F. Bahadoran and N. Safari, *ChemistrySelect*, 2019, **4**, 6113–6122.
246 D. Liu, Y. Men, J. Wang, G. Kolb, X. Liu, Y. Wang and Q. Sun, *Int. J. Hydrogen Energy*, 2016, **41**, 21990–21999.
247 N. Köwitsch, S. Barth, K. Ploner, R. Blume, D. Teschner, S. Penner and M. Armbrüster, *ChemPhysChem*, 2022, **23**, e202200074.
248 X. Liu, Y. Men, J. Wang, R. He and Y. Wang, *J. Power Sources*, 2017, **364**, 341–350.
249 N. Köwitsch, L. Thoni, B. Klemmed, A. Benad, P. Paciok, M. Heggen, A. Eychmüller and M. Armbrüster, *J. Phys. Chem. C*, 2021, **125**, 9809–9817.
250 A. Karim, T. Conant and A. Datye, *J. Catal.*, 2006, **243**, 420–427.
251 Y. Ma, G. Guan, C. Shi, A. Zhu, X. Hao, Z. Wang, K. Kusakabe and A. Abudula, *Int. J. Hydrogen Energy*, 2014, **39**, 258–266.
252 Y. Ma, G. Guan, X. Hao, Z. Zuo, W. Huang, P. Phanthong, K. Kusakabe and A. Abudula, *RSC Adv.*, 2014, **4**, 44175–44184.
253 N. Yi, R. Si, H. Saltsburg and M. Flytzani-Stephanopoulos, *Energy Environ. Sci.*, 2010, **3**, 831–837.
254 S. Pongstabodee, S. Monyanon and A. Luengnaruemitchai, *J. Ind. Eng. Chem.*, 2012, **18**, 1272–1279.
255 M. Yang, S. Li and G. Chen, *Appl. Catal., B*, 2011, **101**, 409–416.
256 N. Onishi and Y. Himeda, *Coord. Chem. Rev.*, 2022, **472**, 214767.
257 D. Morton and D. J. Cole-Hamilton, *J. Chem. Soc., Chem. Commun.*, 1987, 248–249, DOI: **10.1039/C39870000248**.
258 M. Nielsen, E. Alberico, W. Baumann, H.-J. Drexler, H. Junge, S. Gladiali and M. Beller, *Nature*, 2013, **495**, 85–89.
259 A. Monney, E. Barsch, P. Sponholz, H. Junge, R. Ludwig and M. Beller, *Chem. Commun.*, 2014, **50**, 707–709.
260 R. E. Rodríguez-Lugo, M. Trincado, M. Vogt, F. Tewes, G. Santiso-Quinones and H. Grützmacher, *Nat. Chem.*, 2013, **5**, 342–347.
261 P. Hu, Y. Diskin-Posner, Y. Ben-David and D. Milstein, *ACS Catal.*, 2014, **4**, 2649–2652.
262 F. F. van de Watering, M. Lutz, W. I. Dzik, B. de Bruin and J. N. H. Reek, *ChemCatChem*, 2016, **8**, 2752–2756.
263 K.-I. Fujita, R. Kawahara, T. Aikawa and R. Yamaguchi, *Angew. Chem., Int. Ed.*, 2015, **54**, 9057–9060.
264 C. Prichatz, E. Alberico, W. Baumann, H. Junge and M. Beller, *ChemCatChem*, 2017, **9**, 1891–1896.
265 E. Alberico, P. Sponholz, C. Cordes, M. Nielsen, H.-J. Drexler, W. Baumann, H. Junge and M. Beller, *Angew. Chem., Int. Ed.*, 2013, **52**, 14162–14166.
266 M. Andérez-Fernández, L. K. Vogt, S. Fischer, W. Zhou, H. Jiao, M. Garbe, S. Elangovan, K. Junge, H. Junge,

R. Ludwig and M. Beller, *Angew. Chem., Int. Ed.*, 2017, **56**, 559–562.
267 E. A. Bielinski, M. Förster, Y. Zhang, W. H. Bernskoetter, N. Hazari and M. C. Holthausen, *ACS Catal.*, 2015, **5**, 2404–2415.
268 E. Alberico, A. J. J. Lennox, L. K. Vogt, H. Jiao, W. Baumann, H.-J. Drexler, M. Nielsen, A. Spannenberg, M. P. Checinski, H. Junge and M. Beller, *J. Am. Chem. Soc.*, 2016, **138**, 14890–14904.
269 J. Luo, S. Kar, M. Rauch, M. Montag, Y. Ben-David and D. Milstein, *J. Am. Chem. Soc.*, 2021, **143**, 17284–17291.
270 C. Prichatz, E. Alberico, W. Baumann, H. Junge and M. Beller, *ChemCatChem*, 2017, **9**, 1891–1896.
271 V. Arora, E. Yasmin, N. Tanwar, V. R. Hathwar, T. Wagh, S. Dhole and A. Kumar, *ACS Catal.*, 2023, **13**, 3605–3617.
272 S. Kuld, M. Thorhauge, H. Falsig, C. F. Elkjær, S. Helveg, I. Chorkendorff and J. Sehested, *Science*, 2016, **352**, 969–974.
273 F. Studt, M. Behrens, E. L. Kunkes, N. Thomas, S. Zander, A. Tarasov, J. Schumann, E. Frei, J. B. Varley, F. Abild-Pedersen, J. K. Nørskov and R. Schlögl, *ChemCatChem*, 2015, **7**, 1105–1111.
274 A. Bansode and A. Urakawa, *J. Catal.*, 2014, **309**, 66–70.
275 J. Graciani, K. Mudiyanselage, F. Xu, A. E. Baber, J. Evans, S. D. Senanayake, D. J. Stacchiola, P. Liu, J. Hrbek, J. F. Sanz and J. A. Rodriguez, *Science*, 2014, **345**, 546–550.
276 S. Tada, A. Katagiri, K. Kiyota, T. Honma, H. Kamei, A. Nariyuki, S. Uchida and S. Satokawa, *J. Phys. Chem. C*, 2018, **122**, 5430–5442.
277 Y. Chai, B. Qin, B. Li, W. Dai, G. Wu, N. Guan and L. Li, *Natl. Sci. Rev.*, 2023, nwad043, DOI: **10.1093/nsr/nwad043**.
278 N. Iwasa, H. Suzuki, M. Terashita, M. Arai and N. Takezawa, *Catal. Lett.*, 2004, **96**, 75–78.
279 J. Song, S. Liu, C. Yang, G. Wang, H. Tian, Z.-J. Zhao, R. Mu and J. Gong, *Appl. Catal., B*, 2020, **263**, 118367.
280 X. Zhou, J. Qu, F. Xu, J. Hu, J. S. Foord, Z. Zeng, X. Hong and S. C. Edman Tsang, *Chem. Commun.*, 2013, **49**, 1747–1749.
281 J. Qu, X. Zhou, F. Xu, X.-Q. Gong and S. C. E. Tsang, *J. Phys. Chem. C*, 2014, **118**, 24452–24466.
282 J. Wang, S.-m Lu, J. Li and C. Li, *Chem. Commun.*, 2015, **51**, 17615–17618.
283 J. Ye, C. Liu and Q. Ge, *J. Phys. Chem. C*, 2012, **116**, 7817–7825.
284 J. Ye, C. Liu, D. Mei and Q. Ge, *ACS Catal.*, 2013, **3**, 1296–1306.
285 K. Sun, Z. Fan, J. Ye, J. Yan, Q. Ge, Y. Li, W. He, W. Yang and C.-J. Liu, *J. $CO_2$* Util., 2015, **12**, 1–6.
286 O. Martin, A. J. Martín, C. Mondelli, S. Mitchell, T. F. Segawa, R. Hauert, C. Drouilly, D. Curulla-Ferré and J. Pérez-Ramírez, *Angew. Chem., Int. Ed.*, 2016, **55**, 6261–6265.
287 M. S. Frei, C. Mondelli, A. Cesarini, F. Krumeich, R. Hauert, J. A. Stewart, D. Curulla Ferré and J. Pérez-Ramírez, *ACS Catal.*, 2020, **10**, 1133–1145.
288 N. Rui, Z. Wang, K. Sun, J. Ye, Q. Ge and C.-J. Liu, *Appl. Catal., B*, 2017, **218**, 488–497.
289 Z. Han, C. Tang, J. Wang, L. Li and C. Li, *J. Catal.*, 2021, **394**, 236–244.
290 X. Jia, K. Sun, J. Wang, C. Shen and C.-J. Liu, *J. Energy Chem.*, 2020, **50**, 409–415.
291 J. Wang, K. Sun, X. Jia and C.-J. Liu, *Catal. Today*, 2021, **365**, 341–347.
292 S. Tang, Z. Feng, Z. Han, F. Sha, C. Tang, Y. Zhang, J. Wang and C. Li, *J. Catal.*, 2023, **417**, 462–472.
293 N. Rui, F. Zhang, K. Sun, Z. Liu, W. Xu, E. Stavitski, S. D. Senanayake, J. A. Rodriguez and C.-J. Liu, *ACS Catal.*, 2020, **10**, 11307–11317.
294 J. Wang, G. Li, Z. Li, C. Tang, Z. Feng, H. An, H. Liu, T. Liu and C. Li, *Sci. Adv.*, 2017, **3**, e1701290.
295 J. Wang, C. Tang, G. Li, Z. Han, Z. Li, H. Liu, F. Cheng and C. Li, *ACS Catal.*, 2019, **9**, 10253–10259.
296 J. Hu, L. Yu, J. Deng, Y. Wang, K. Cheng, C. Ma, Q. Zhang, W. Wen, S. Yu, Y. Pan, J. Yang, H. Ma, F. Qi, Y. Wang, Y. Zheng, M. Chen, R. Huang, S. Zhang, Z. Zhao, J. Mao, X. Meng, Q. Ji, G. Hou, X. Han, X. Bao, Y. Wang and D. Deng, *Nat. Catal.*, 2021, **4**, 242–250.
297 X. Jiang, X. Nie, X. Guo, C. Song and J. G. Chen, *Chem. Rev.*, 2020, **120**, 7984–8034.
298 S.-T. Bai, G. De Smet, Y. Liao, R. Sun, C. Zhou, M. Beller, B. U. W. Maes and B. F. Sels, *Chem. Soc. Rev.*, 2021, **50**, 4259–4298.
299 A. Klerke, C. H. Christensen, J. K. Nørskov and T. Vegge, *J. Mater. Chem.*, 2008, **18**, 2304.
300 K. E. Lamb, M. D. Dolan and D. F. Kennedy, *Int. J. Hydrogen Energy*, 2019, **44**, 3580–3593.
301 L. Green, *Int. J. Hydrogen Energy*, 1982, **7**, 355–359.
302 R. Lan, J. T. S. Irvine and S. Tao, *Int. J. Hydrogen Energy*, 2012, **37**, 1482–1494.
303 S. Lee, T. Kim, G. Han, S. Kang, Y.-S. Yoo, S.-Y. Jeon and J. Bae, *Renewable Sustainable Energy Rev.*, 2021, **150**, 111447.
304 X. Duan, J. Ji, G. Qian, C. Fan, Y. Zhu, X. Zhou, D. Chen and W. Yuan, *J. Mol. Catal. A: Chem.*, 2012, **357**, 81–86.
305 C. Chen, K. Wu, H. Ren, C. Zhou, Y. Luo, L. Lin, C. Au and L. Jiang, *Energy Fuels*, 2021, **35**, 11693–11706.
306 A. Boretti and S. Castelletto, *ACS Energy Lett.*, 2022, **7**, 2557–2564.
307 S. F. Yin, B. Q. Xu, X. P. Zhou and C. T. Au, *Appl. Catal., A*, 2004, **277**, 1–9.
308 K. Yamazaki, M. Matsumoto, M. Ishikawa and A. Sato, *Appl. Catal., B*, 2023, **325**, 122352.
309 F. Zhiqiang, W. Ziqing, L. Dexing, L. Jianxin, Y. Lingzhi, W. Qin and W. Zhong, *Fuel*, 2022, **326**, 125094.
310 N. Jeon, S. Kim, A. Tayal, J. Oh, W. Yoon, W. B. Kim and Y. Yun, *ACS Sustainable Chem. Eng.*, 2022, **10**, 15564–15573.
311 T. A. Le, Y. Kim, H. W. Kim, S.-U. Lee, J.-R. Kim, T.-W. Kim, Y.-J. Lee and H.-J. Chae, *Appl. Catal., B*, 2021, **285**, 119831.
312 L. Huo, X. Han, L. Zhang, B. Liu, R. Gao, B. Cao, W. Wang, C. Jia, K. Liu, J. Liu and J. Zhang, *Appl. Catal., B*, 2021, **294**, 120254.
313 Q. C. Do, Y. Kim, T. A. Le, G. J. Kim, J.-R. Kim, T.-W. Kim, Y.-J. Lee and H.-J. Chae, *Appl. Catal., B*, 2022, **307**, 121167.

314 C. Zhou, K. Wu, H. Huang, C. Cao, Y. Luo, C. Chen, L. Lin, C. Au and L. Jiang, *ACS Catal.*, 2021, **11**, 10345–10350.
315 H. Maleki, M. Fulton and V. Bertola, *Chem. Eng. J.*, 2021, **411**, 128595.
316 S.-F. Yin, B.-Q. Xu, C.-F. Ng and C.-T. Au, *Appl. Catal., B*, 2004, **48**, 237–241.
317 L. Li, Y. Wang, Z. P. Xu and Z. Zhu, *Appl. Catal., A*, 2013, **467**, 246–252.
318 S. Sayas, N. Morlanés, S. P. Katikaneni, A. Harale, B. Solami and J. Gascon, *Catal. Sci. Technol.*, 2020, **10**, 5027–5035.
319 J. Zhao, S. Xu, H. Wu, Z. You, L. Deng and X. Qiu, *Chem. Commun.*, 2019, **55**, 14410–14413.
320 H. He, H. Jiang, F. Yang, J. Liu, W. Zhang, M. Jin and Z. Li, *Int. J. Hydrogen Energy*, 2023, **48**, 5030–5041.
321 H. Li, L. Guo, J. Qu, X. Fang, Y. Fu, J. Duan, W. Wang and C. Li, *Int. J. Hydrogen Energy*, 2023, **48**, 8985–8996.
322 L. Zhou, X. Fu, Y. Xu, W. Wang and C. Jia, *ACS Appl. Nano Mater.*, 2023, **6**, 2952–2962.
323 S.-J. Park and B.-J. Kim, *J. Colloid Interface Sci.*, 2005, **291**, 597–599.
324 C. W. Skarstrom, *Ann. N. Y. Acad. Sci.*, 1959, **72**, 751–763.
325 K. P. Kostroski and P. C. Wankat, *Ind. Eng. Chem. Res.*, 2006, **45**, 8117–8133.
326 T. Inui, Y. Okugawa and M. Yasuda, *Ind. Eng. Chem. Res.*, 1988, **27**, 1103–1109.
327 G. Q. Lu, J. C. Diniz da Costa, M. Duke, S. Giessler, R. Socolow, R. H. Williams and T. Kreutz, *J. Colloid Interface Sci.*, 2007, **314**, 589–603.
328 S. G. Shore and R. W. Parry, *J. Am. Chem. Soc.*, 1955, **77**, 6084–6085.
329 U. B. Demirci, *Int. J. Hydrogen Energy*, 2017, **42**, 9978–10013.
330 B. L. Conley, D. Guess and T. J. Williams, *J. Am. Chem. Soc.*, 2011, **133**, 14212–14215.
331 J. M. B. Richard, J. Keaton and R. Tom Baker, *J. Am. Chem. Soc.*, 2007, **129**, 1844–1845.
332 M. Chandra and Q. Xu, *J. Power Sources*, 2006, **156**, 190–194.
333 W. Chen, D. Li, Z. Wang, G. Qian, Z. Sui, X. Duan, X. Zhou, I. Yeboah and D. Chen, *AlChE J.*, 2017, **63**, 60–65.
334 J. Liu, P. Li, R. Jiang, X. Zheng and P. Liu, *ChemCatChem*, 2021, **13**, 4142–4150.
335 A. Aijaz, A. Karkamkar, Y. J. Choi, N. Tsumori, E. Rönnebro, T. Autrey, H. Shioyama and Q. Xu, *J. Am. Chem. Soc.*, 2012, **134**, 13926–13929.
336 S. Ö. Önder Metin, *Energy Fuels*, 2009, **23**, 3517–3526.
337 P. Li, Y. Huang, Q. Huang, R. Chen, J. Li and S. Tian, *J. Energy Chem.*, 2023, **79**, 72–82.
338 Z. Li, T. He, L. Liu, W. Chen, M. Zhang, G. Wu and P. Chen, *Chem. Sci.*, 2017, **8**, 781–788.
339 R. K. Borah, A. P. Fatrekar, P. Bakre, S. G. Tilve and A. A. Vernekar, *J. Mater. Chem. A*, 2022, **10**, 25490–25499.
340 C. Yuan, T. Xu, M. Guo, T. Zhang and X. Yu, *Appl. Catal., B*, 2023, **321**, 122044.
341 W. Xu, M. Liu, S. Wang, Z. Peng, R. Shen and B. Li, *Int. J. Hydrogen Energy*, 2022, **47**, 23213–23220.
342 B. Pant, H. R. Pant, M. Park, Y. Liu, J.-W. Choi, N. A. M. Barakat and H.-Y. Kim, *Catal. Commun.*, 2014, **50**, 63–68.
343 S. Hu, X. Qu, J. Bai, P. Li, Q. Li, F. Wang and L. Song, *ACS Sustainable Chem. Eng.*, 2017, **5**, 6863–6872.
344 N. Kang, X. Wei, R. Shen, B. Li, E. G. Cal, S. Moya, L. Salmon, C. Wang, E. Coy, M. Berlande, J.-L. Pozzo and D. Astruc, *Appl. Catal., B*, 2023, **320**, 121957.
345 B. Coşkuner Filiz and A. Kantürk Figen, *Int. J. Hydrogen Energy*, 2023, DOI: **10.1016/j.ijhydene.2022.12.176**.
346 X. Li, Q. Yao, Z. Li, H. Li, Q. Zhu and Z. Lu, *J. Mater. Chem. A*, 2022, **10**, 326–336.
347 J. Liao, Y. Shao, Y. Feng, J. Zhang, C. Song, W. Zeng, J. Tang, H. Dong, Q. Liu and H. Li, *Appl. Catal., B*, 2023, **320**, 121973.
348 J. Liao, Y. Wu, Y. Shao, Y. Feng, X. Zhang, W. Zhang, J. Li, M. Wu, H. Dong, Q. Liu and H. Li, *Chem. Eng. J.*, 2022, **449**, 137755.
349 Y. Cheng, X. Wu and H. Xu, *Sustainable Energy Fuels*, 2019, **3**, 343–365.
350 X. Yang, D. A. Bulushev, J. Yang and Q. Zhang, *Energies*, 2022, **15**, 6360.
351 P. Li, R. Chen, Y. Huang, W. Li, S. Zhao and S. Tian, *Appl. Catal., B*, 2022, **300**, 120725.
352 P. Li, Y. Huang, Q. Huang, R. Chen, J. Li and S. Tian, *Appl. Catal., B*, 2022, **313**, 121444.
353 J. Deng, X. Zhou, J. Zou, Y. Qin and P. Wang, *ACS Appl. Energy Mater.*, 2022, **5**, 7408–7419.
354 S. Zhou, Y. Yang, P. Yin, Z. Ren, L. Wang and M. Wei, *ACS Appl. Mater. Interfaces*, 2022, **14**, 5275–5286.
355 J. Prasad and J. L. Gland, *Langmuir*, 1991, **7**, 722–726.
356 D. J. Alberas, J. Kiss, Z. M. Liu and J. M. White, *Surf. Sci.*, 1992, **278**, 51–61.
357 S. K. Singh, X.-B. Zhang and Q. Xu, *J. Am. Chem. Soc.*, 2009, **131**, 9894–9895.
358 K. S. Al-Thubaiti and Z. Khan, *Int. J. Hydrogen Energy*, 2020, **45**, 13960–13974.
359 Q. Yao, M. He, X. Hong, X. Chen, G. Feng and Z. Lu, *Int. J. Hydrogen Energy*, 2019, **44**, 28430–28440.
360 S. K. Singh and Q. Xu, *Inorg. Chem.*, 2010, **49**, 6148–6152.
361 P. Zhao, N. Cao, J. Su, W. Luo and G. Cheng, *ACS Sustainable Chem. Eng.*, 2015, **3**, 1086–1093.